December 2017

Design and Modeling of Fiber Optical Current Sensor Based on Magnetostriction

Suha Mubarak Lasassmeh
University of Wisconsin-Milwaukee

DESIGN AND MODELING OF FIBER OPTICAL CURRENT SENSOR BASED ON MAGNETOSTRICTION

by

Suha Lasassmeh

A Dissertation Submitted in

Partial Fulfillment of the

Requirements for the Degree of

Doctor of Philosophy

in Engineering

at

The University of Wisconsin-Milwaukee

December 2017

ABSTRACT
DESIGN AND MODELING OF FIBER OPTICAL CURRENT SENSOR BASED ON MAGNETOSTRICTION

by

Suha Lasassmeh

The University of Wisconsin-Milwaukee, 2017
Under the Supervision of Professor Chiu-Tai Law

A novel fiber optical current sensor (FOCS) which is based on a giant magnetostrictive material, Terfenol-D (T-D) is modeled and prototyped. Several experiments have been conducted to validate the expected results. Magnetostriction is defined as the change in dimensions of a material under the influence of an external magnetic field. The cause of the change in length is due to the rotation and re-orientation of the small magnetic domains in the magnetostrictive material. The magnetostriction of Terfenol-D is modeled and investigated using several software packages. Here, a magnetostriction-based FOCS using a Terfenol-D/epoxy composite is investigated. Particularly, the FOCS is based on applying magnetostrictive composite material to transform an external magnetic field into a corresponding mechanical strain caused by the magnetostriction of the composite. The composite is incorporated in the FOCS for increased durability, flexibility in shape, extended frequency response, and tensile strength compared to monolithic materials. Coupling Terfenol-D with a fiber Bragg grating (FBG) is an excellent method of magnetic field sensing. It consists of an FBG embedded in the composite that converts magnetostrictive strain into frequency chirp of the optical signal in proportion to a magnetic field. This will form a sensor that is compact, lightweight, and immune from electromagnetic interference. For electromagnetic interference mitigation and optimal signal condition, an FBG, which can be easily integrated with an optical fiber network and reflect a narrow band of

wavelengths based on grating periods, is used to encode strain information onto an optical signal. This FOCS has potential in detecting power systems faults due to its advantages over the conventional current transformers.

Experiments have been performed to investigate the effect of direct current (DC) and alternate current (AC) on the response of the FOCS. Consistent results that indicate its reliability have been obtained. The experiment results matched the predicted response. The effect of the temperature on the response of the FOCS also has been investigated. Finally, future research directions are presented for the enhancement of the FOCS technology.

TABLE OF CONTENTS

LIST OF FIGURES

LIST OF TABLES

LIST OF SYMBOLS

μ_0 – Vacuum permeability

r – Rogowski radius

N –number of turns of the coil

λ_B – Bragg wavelength

n_{eff} – effective fiber refractive index

Λ – fiber Bragg grating period

δn_{eff} – FBG refractive index perturbation

$\overline{\delta n}_{eff}$ – "DC" refractive index perturbation

v – fringe visibility of refractive index perturbation

ϕ – phase of index perturbation corresponding to chirp or discrete phase shift

A – forward-traveling wave amplitude in coupled-mode equations

B – backward-traveling wave amplitude in coupled-mode equations

$\hat{\sigma}$ – general "DC" self-coupling coefficient

κ – "AC" coupling coefficient

δ – wavenumber detuning from Bragg wavenumber

σ – "DC" coupling coefficient

L – FBG length

r – amplitude reflection coefficient

R – power reflectivity

ρ – amplitude reflection as a function of z

M – number of uniform grating sections assumed for numerical modeling

$\mathbf{T}_m$ – transfer matrix for uniform section m

$\mathbf{T}$ – transfer matrix of entire grating

$\mathbf{T}_p$ – transfer matrix for a phase shift

P_0 – sensor output power at zero-field or low field

P_1 – normalized increase in sensor output power

H – magnetic field intensity

ϵ – strain

p_e – Effective strain-optic coefficient

p_{ij} – components of strain-optic tensor

ν – Poisson's ratio

λ_p – peak reflection wavelength in FBG reflection spectrum

λ_0 – Peak reflection wavelength with no incident field

M_s – Saturation magnetization

K_0 – Zero-order magnetocrystalline anisotropy constant

K_1 – First-order magnetocrystalline anisotropy constant

K_2 – Second-order magnetocrystalline anisotropy constant

E_A – Anisotropy energy

E_z – Zeeman energy

E_k – Magnetocrystalline anisotropy energy

ΔT – Temperature difference between ambient temperature and room temperature

H_0 – Characteristic magnetic field for effective FBG strain fit

P_n – the power value of to the n^{th} data point out of all the wavelength meter data

V_B – Battery voltage in photodetector circuit

R_L – load resistance in photodetector circuit

$\mathcal{R}$ – photodiode responsivity

V_o – photodetector circuit output voltage

P_{OPT} – total optical power output from sensor

Δf – frequency resolution of wavelength meter

LIST OF ABBREVIATIONS

OCS – Optical Current Sensor

FBG – Fiber Bragg Grating

DC – Direct Current

AC – Alternating Current

CT – Current Transformer

FOCS – Fiber Optic Current Sensor

SLED – Superluminescent Light Emitting Diode

WLM – Wavelength Meter

OC – Optical Circulator

GUI – Graphical User Interface

rms – root mean square

GPIB – General Purpose Interface Bus

USB – universal serial bus

FWHM – Full Width at Half Maximum

OSA – Optical Spectrum Analyzer

Mf - Manufacturer

sn (S/N) – Serial Number

TD – Terfenol-D

ACKNOWLEDGEMENTS

First and foremost, I would like to thank my advisor Prof. Chiu Law. It has been an honor to work with him. I appreciate all his contributions of time, ideas, and helpful discussions to make my Ph.D. experience productive and stimulating. He motivated me to do my best in my research.

I would like to thank Dr. Rani El-Hajjar who offered me a great help to model the magentostriction of Terfenol-D using COMSOL Multiphysics. He shared with me his models which gave me a great insight into how to model my sensors.

I am very grateful to the members of my dissertation committee, Dr. Adel Nasiri, Dr. Ramin Pashaie, Dr. Sung Yongjin, and Dr. Hossein Hosseini. Their academic support and input are greatly appreciated.

Additionally, I would like to thank Aaron Muller, Daniel J Brandt, and Edward Joseph Lynch for their collaboration and their helpful ideas for improving the sensor.

I would like to thank my parents who supported me in all my pursuits and they have taught me about hard work and self-respect. I also would like to thank my sisters and my brothers for their love and support.

I would like to give a special thanks to my loving, supportive, encouraging, and patient husband Issam who endured this long process with me, always offering support and love.

Finally, I would like to thank my lovely children: Randa, Sami, and Tamem who are the pride and joy of my life. I love you more than anything and I appreciate all your patience during my Ph.D. studies.

1. INTRODUCTION

1.1 REVIEW OF CONVENTIONAL CURRENT SENSORS

The interest in sensors for electrical current metering has increased significantly over the last decade due to the massive growth in the use of electric equipment in developed countries and the worldwide increase of the electrical distribution/consumption [1]. In electrical power distribution systems fault detection devices and schemes are very important. Conventionally, a sequence of relays, current transformers (CT), and circuit breakers are deployed along power systems for the protection purpose with CTs functioning as current sensors. The CTs are used extensively for electric current sensing and monitoring the operation of the power grid [2]. The aim of this section is to provide a survey of the techniques that are available for current sensing. These techniques can be classified based upon the underlying physical principle as follow [3]:

1. Ohm's law of resistance
2. Faraday's law of induction
3. Magnetic field sensors
4. Faraday effect.

1.1.1 CURRENT SENSORS BASED UPON OHM'S LAW OF RESISTANCE

By the Ohm's law (in equation 1.1) which states that the voltage drop V across a resistor R is proportional to the current I flowing, the resistor can be used for current sensing.

$$V = IR \tag{1.1}$$

The advantages of using current sensors which are based upon Ohm's law are the low cost and reliability owing to the simple working principle.

Shunt resistor is the simplest approach that can be used for sensing direct current (DC) and alternating current (AC). The voltage drop across the shunt resistor is used as an indicator of the current flow. Trace resistance (copper trace or busbar) sensing is another approach that based upon

the ohm's law to sense the current instead of using a dedicated shunt resistor. This approach has very low cost with no additional power losses. However this approach has difficulties in maintaining reasonable accuracy owing to large thermal drift [3].

1.1.2 CURRENT SENSORS BASED UPON FARADAY'S LAW OF INDUCTION

Current sensors based upon Faraday's law of induction provide electrical isolation between the current that needs to be measured and the output signals. Rogowski coil (shown in Fig. 1.1) is a common technique that has been used for current sensing based upon Faraday's law [3]. Rogowski transducers have the following features: very high bandwidth, capability of measuring large currents, non-saturation, and ease of use [4].

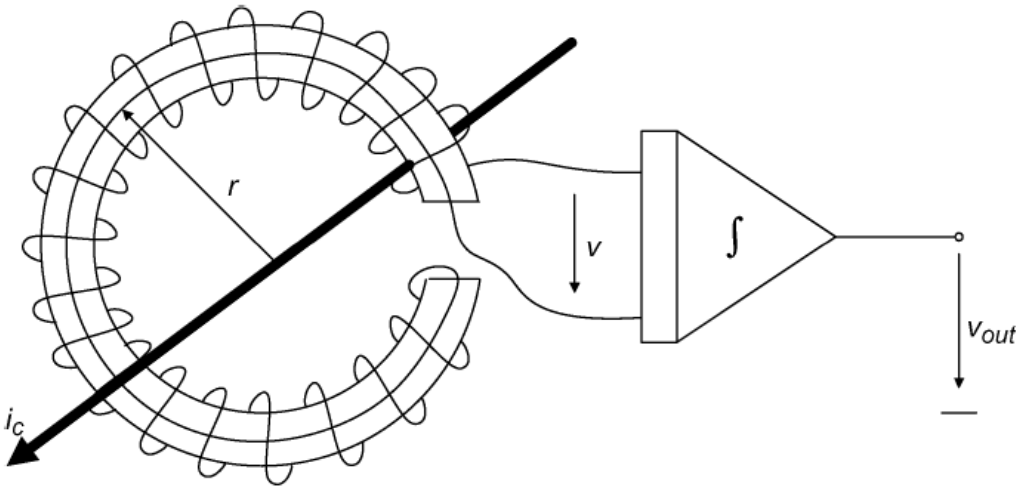

Fig. 1.1: Schematic of a Rogowski coil that uses a nonmagnetic core material [3].

The working principle of Rogowski coil is based on Ampere's law which relates the closed path integral of the magnetic flux density $\vec{B}$ inside the coil to the current $\vec{\imath}_c$:

$$\oint \vec{B} \cdot d\vec{l} = \mu_0 i_c \tag{1.2}$$

where μ_o is the air permeability and i_C flows through the area enclosed by the closed path. Then $\vec{B}$ inside the coil can be found in terms of the current i_C and the Rogowski radius r with the assumption that the cross-section diameter of the Rogowski coil is much smaller than its radius.

$$B = \frac{\mu_0 i_c}{2\pi r} \tag{1.3}$$

The induced voltage into the Rogowski coil due to the change in the current i_C can be found by applying Faraday's law of induction.

$$v = -N\frac{d\phi}{dt} = -NA\frac{dB}{dt} = -\frac{NA\mu_0}{2\pi r}\frac{di_C}{dt} \tag{1.4}$$

Where A is the cross sectional area of the coil body that is formed by the windings, and N is the number of turns. An integrator with integrating constant k is required to get a signal S_{out} proportional to the primary current i_C from the induced voltage (as shown in Fig 1.1).

$$S_{out} = -\frac{NA\mu_0}{2\pi r}k\int_t \frac{di_C}{dt}.dt + S(0)_{out} = -k\frac{NA\mu_0}{2\pi r}i_C + S_{out}(0) \tag{1.5}$$

Rogowski coil can be used to measure currents in power distribution systems, slip-ring induction motors, and short-circuit testing without saturation and hysteresis [3].

Current transform (CT) is another common technique employs Faraday's law of induction to measure current (shown in Fig 1.2). CT consists of one primary turn and N secondary turns similar to Rogowski coil but the core material has high relative permeability μ_r. The secondary winding of the current transformer is loaded with a sense resistor R_s. The current i_s through R_s generates a magnetic flux that reacts to counter the flux generated by the primary current.

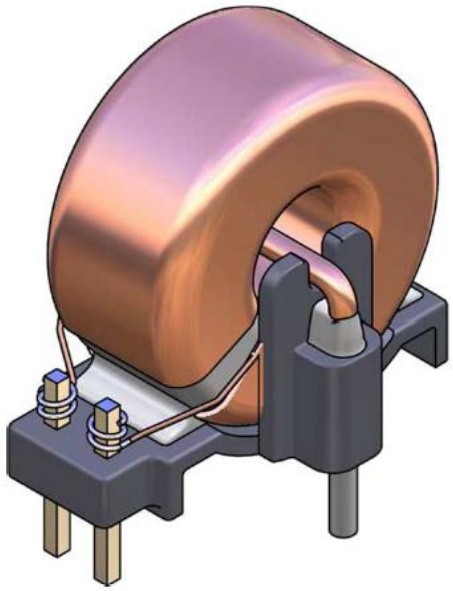

Fig. 1.2: Current transformer consisting of one primary turn and multiple secondary turn [3].

The voltage v_s across R_s can be derived and written in terms of the cross-sectional area of the core A, N, and the average circumference of the core l_m.

$$v_s = -N\frac{d\phi}{dt} = -NA\frac{\mu_0\mu_r}{l_m}\frac{d(i_c - Ni_s)}{dt} \tag{1.6}$$

To solve for i_s the above equation can be rewritten as

$$i_s = \frac{i_c}{N} - \frac{l_m}{N^2 A\mu_0\mu_r}\int_t v_s.dt \tag{1.7}$$

The CT is typically described by its current ratio between primary and secondary coils. The secondary side of a current transformer should not be disconnected from its load while current is flowing in the primary to avoid high voltage [3]. The ratings of the secondary windings of the current transformer have been standardized in order to achieve some form of interchangeability among different relays and meters from various manufactures. In the US, CT secondary windings are rated for 5A. CTs can be manufactured as free-standing devices, or they may be built inside the bushing of some power apparatus such as a circuit breaker [1].

1.1.3 MAGNETIC FIELD SENSORS

Magnetic field sensors are able to sense static and dynamic fields, and can be considered as a major advantage for the magnetic field sensors over the current sensors based on Faraday's law of induction that cannot perform DC measurements. There are different configurations for current sensing with magnetic field sensing devices. Hall Effect sensor is one of the most popular magnetic field sensors [3].

1.1.4 CURRENT SENSORS THAT USE THE FARADAY EFFECT

One of the Michael Faraday's many discoveries was finding a difference in refractive index of glass for left-handed and right-handed circularly polarized light induced by an external magnetic field. In 1854, Émile Verdet showed that the angle of rotation θ of linearly polarized light is proportional to the strength of the magnetic field and the cosine of the angle between the field and the propagation direction of the light wave [1]. This can be expressed mathematically by:

$$\theta = V \int \vec{H} \cdot d\vec{s} \tag{1.8}$$

where, V is Verdet constant of the optical material, $\vec{H}$ is the applied magnetic field intensity, and $d\vec{s}$ is the differential vector for the line integral along the direction of propagation. This effect is called the Faraday effect or linear magneto-optic effect and can be used to build optical current sensors (OCSs).

1.2 INTORDUCTION TO OPTICAL CURRENT SENSOR TECHNOLOGY

OCSs have many considerable advantages over the conventional CTs, including immunity to electromagnetic interference (EMI), wide measurement range, compact design, reduced complexity, the potential to make measurements in high voltage and/or high magnetic induction environment, lower cost of insulation and light weight [5], [6]. Owing to these advantages, interest in OCS technology has increased lately.

According to the sensing mechanisms, OCSs can be categorized into two main groups: (i) OCSs operating on the principle of Faraday magneto-optics, (ii) OCSs employing magnetostrictive materials. In Faraday magneto-optic effect, the polarization azimuth angle of a linearly polarized light beam propagating inside an optical material is rotated under the influence of a magnetic field which is generated by the electrical current to be measured [7]. On the other hand, OCSs operating on the principle of magnetostriction converts the magnetic field generated by a nearby current source into longitudinal mechanical strain, which is used to modulate an optical signal carried by a fiber. Yariv and Winsor developed OCS employing magnetostrictive material as a transducer to detect the magnetic field [8]. The basic geometry of their sensor is a low-loss optical fiber embedded in a magnetostrictive jacket that undergoes a longitudinal strain (magnetostriction) when immersed in a magnetic field. This strain affects the phase delay of a light beam propagating in the fiber [8]. Mora et al presented a magnetostrictive sensor for dc magnetic fields interrogated by two fiber Bragg gratings (FBGs) that measures electric current and temperature simultaneously [9]. This sensor consists of two rods of different alloys joined together and a fiber grating epoxy-bonded to those alloys as shown in Fig. 1.3. The first rod is made of Terfenol-D (T-D) which is a giant magnetostrictive material while the second rod is made of Monel 400. Both materials have the same thermal expansion coefficient. When T-D expands elastically under a magnetic field, the Bragg wavelength of its attached grating is shifted and the FBG outputs at longer wavelengths. However this sensor configuration requires spectral measurement and does not compensate for temperature. Yi *et al*. [10] used two techniques to compensate for the temperature effect. The first technique involved two FBGs placed perpendicular to each other and bounded onto a single T-D layer. The second technique involved two FBGs and stacking them onto two different magnetostrictive bars (T-D and nickel) which are placed physically parallel to each other. T-D and

nickel have similar thermal expansion coefficients but opposite polarity in magnetostrictive coefficients. Another configuration of sensor, proposed in [11], uses one grating, one half of the grating mounted on T-D and the other half of the FBG mounted on the Monel-400 rod. However, this design has a fragile structure owing to the brittleness of T-D, and the uncoated FBG. The severe shortcoming is in its limited response over a narrow $\vec{H}$ range. Satpathi et al. [12] proposed and prototyped an optical current sensor with a piece of T-D attached to an FBG. T-D was subjected to mechanical pre-stress and DC magnetic field bias tuning in order to obtain a linear response.

Yang et al [13] proposed in 2009 the first optic magnetic field sensor that utilizes a thin film of T-D instead of the bulk one. In this sensor, T-D thin films were deposited on etched FBGs. This method reduced the size of the sensor and increased the sensitivity to the magnetic field. Another approach was presented by Quintero et al. in [14]; they presented a sensor for both AC and DC magnetic field measurements. In this approach the sensor was prototyped by coating the grating with a layer of a composite. This composite was obtained by mixing T-D particles with an epoxy resin.

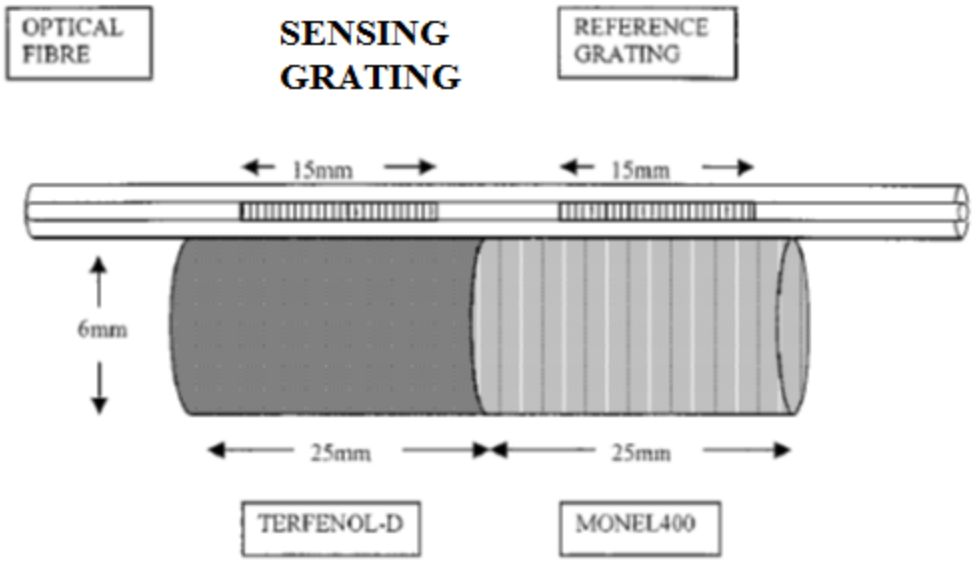

Fig. 1.3: Schematic diagram of the sensor proposed in [8]

1.3 INTRODUCTION TO MAGNETOSTRICTION

Generally, magnetostriction (λ) can be described as the change in the shape of a material due to a change in its state of magnetization (M) [15]. The dimensional change of the magnetic material due to applied magnetic field is known as the Joule effect while the magnetization change of the material due to the applied stress is known as the Villari effect. T-D and Galfenol are the most known giant magnetostrictive materials. Their typical properties are summarized in Table 1.1 below.

Material Name	Free Strain (ppm)	Modulus(GPa)	Tensile Strength (MPa)
Terfenol-D	1600-2400	25 – 35	28 (Brittle)
Galfenol	300 – 400	~ 60	500 (Ductile)

Table 1.1: General properties of Terfenol-D and Galfenol

T-D ($Tb_xDy_{1-x}Fe_y$), with x~0.3 and y~2, is an alloy of rare earths Terbium (Tb) and Dysprosium (Dy) with 3D transition metal Iron (Fe). Large axial magnetostriction at relatively small applied field is the goal of most research investigations on T-D. This alloy is a commercially available material for a large variety of applications and is currently produced in a variety of forms, solid (monolithic), powder and thin films as shown in Fig. 1.4. T-D has numerous applications, such as power ultrasonic transducers, linear motors, micro-pumps, micro-valves, and micro-positioners [16]. The performance of T-D in different applications is highly dependent on the state of the material such as the compressive mechanical load or prestress. It has been found that applying prestress to the T-D sample increases considerably the total strain capability of the material [17].

There are many shortcomings associated with the use of monolithic T-D; operation above a few kilohertz is limited by the presence of eddy-current losses. Another problem associated with monolithic T-D is brittleness, which causes difficulties in machining and device fabrication. To overcome those shortcomings, T-D composites were formed by incorporating T-D particles into a passive polymer matrix [18].

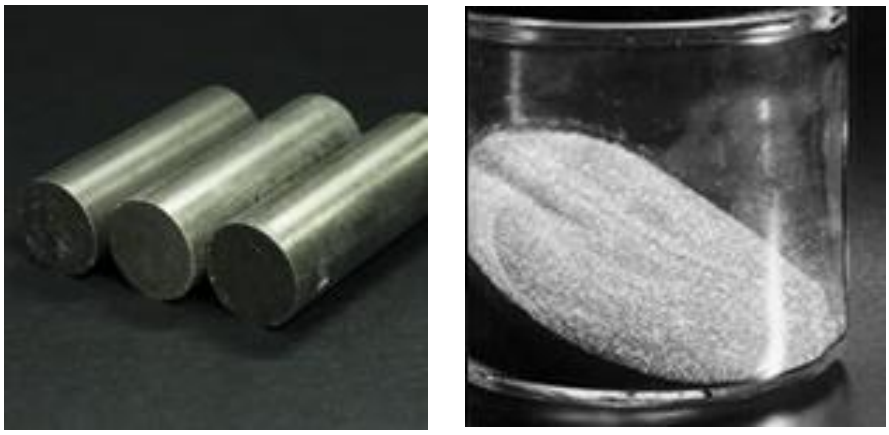

Fig 1.4: Commercially available forms of Terfenol-D.

1.4 MODELING MAGNETOSTRICTION

To fully understand the capabilities of using the magnetostrictive materials in the fiber optical current sensor, it is imperative to model and understand the mechanical and magnetic characteristics of the magnetostrictive materials. For this purpose, several models will be discussed in later chapters such as energy-based models and finite element models that have been implemented in COMSOL Multiphysics .

1.5 PROPOSED FOCS AND COMPONENTS

T-D composites can reduce the eddy current loss and improve the fracture toughness compared to monolithic T-D. In general, magnetostrictive composites can be fabricated by embedding magnetostrictive powders in a nonmetallic binder, such as epoxy. Here, a magnetostriction-based FOCS using a T-D/epoxy composite is investigated. Particularly, the FOCS is based on applying magnetostrictive composite as a transducer that transforms an external magnetic field into a corresponding magnetostrictive strain. The composite is incorporated in the FOCS for increased durability, flexibility in sensor geometry, extended frequency response, and tensile strength compared to monolithic materials. For magnetic field sensing, an FBG is embedded in the composite that converts the magnetostrictive strain distribution into the frequency chirping of the optical signal in proportion to a magnetic field. Such a sensor is compact, lightweight, and immune from electromagnetic interference. Moreover, sensors based on FBGs can be easily integrated with an optical fiber network and enable the encoding of the magnetic field amplitude at various locations into different optical channels. Here, we propose a new design of FOCS that addresses the shortcomings of the previous designs. The new design considers the use of a T-D composite with a graded particle size distribution. A magnetostrictive composite with certain engineered T-D particle distributions can exert various strain distributions according to different levels of

magnetic field. Here, the FBG is embedded in composite blocks with different distributions of T-D particles (T-D particles ranging from 20 to 300 microns are commercially available) that produce an approximately linear strain distribution along the FBG. As a result, the optical signal reflected by the FBG has a spectral width proportional to the magnetic field. The FOCS will be fabricated with specimens of different volume fractions V_f of T-D. In addition, particles of MONEL 400 were blended with T-D particles to compensate for the thermal expansion and ensure a more uniform distribution of T-D. Since strain scales up with higher V_f, the region with higher distribution of T-D particles will have higher strain in an applied magnetic field. In Fig. 1.5, areas with higher volume fraction of T-D are shown with darker gray scale. As $\vec{H}$ increases, an FBG with uniform period (see Fig. 1.5 a) is transformed into a non-uniform one (see Fig. 1.5 b).

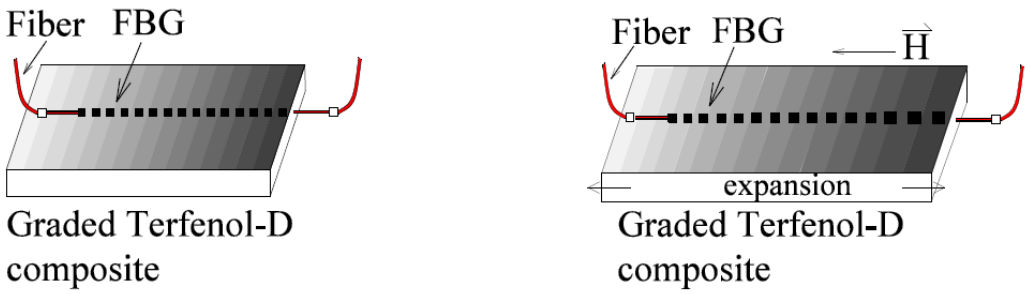

Fig. 1.5a: Chirped FOCS with graded T-D composite at H=0. **Fig. 1.5b**: Chirped FOCS with graded T-D composite at H≠0

We propose another design, the cone-shaped sensor, to improve the response over a wider magnetic field *H* range. Random oriented particles of T-D ranging from 106-300 μm were used to prepare the magnetostrictive composite. Fig. 1.6 shows that the cone has different cross sectional area along its longitudinal axis. Owing to the boundary effect from the tapered shape, the strain and magnetization will raise as the cross section decreases. Thus, the grating period of the FBG

embedded in the cone-shaped magnetostrictive composite becomes aperiodic when the composite is stressed under the effect of the applied magnetic field *H*.

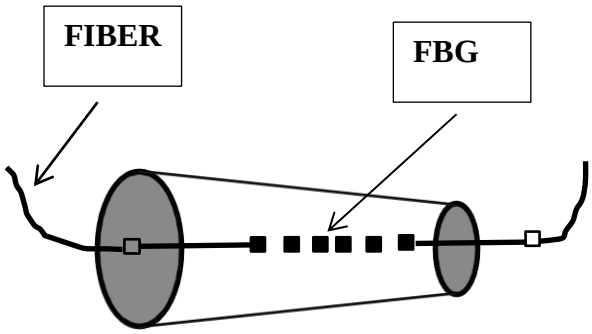

Fig. 1.6: Cone-shaped FOCS.

1.6 EXPERMINTAL COMPONETNTS AND SETUP

The cone-shaped FOCS were prototyped in our lab, and tested for DC and AC operations to obtain their output response. Broadband Superluminescent light emitting diode (SLED) was used as the light source in our experiments. Optical spectrum Analyzer (OSA) was used to characterize the spectral responses of sensors. A single channel fiber link was used to connect the SLED, the output measurement equipment and the sensor as illustrated in Fig. 1.7.

Initially, coils with air core were used to generate the magnetic fields for DC and AC testing in our experiments. The DC coil was powered by two DC power supplies, and the AC coil was powered by an autotransformer. To be able to perform tests with higher magnetic fields, we upgraded our magnetic field source to a laboratory electromagnet which has been used to generate both AC and DC magnetic fields. For both AC and DC testing, the current sensor was placed in middle of the air gap of the laboratory electromagnet to expose it to the generated magnetic fields.

Gaussmeter with a Hall probe was placed tangent to the middle of the sensor to monitor the magnitude of the magnetic field. Experiments were conducted by sweeping the magnetic field of the electromagnet with the current from a power amplifier driven by a function generator. Spectra of the FBG have been recorded with the OSA controlled by the software supplied by the instrument manufacturer, Thorlabs. Further analysis was performed with saved spectra in order to measure the reflected power form the FBG. Previously, wavelength meter associated with a LabVIEW program was used to capture spectral response. Using the OSA and its associated software was a major update to our experiment set up.

Additional experiments have been conducted to investigate the effect of the temperature on the response of our FOCS. The sensor was placed in a controlled thermal chamber. While increasing the temperature from room temperature to 39° C, the spectral data of sensors were collected.

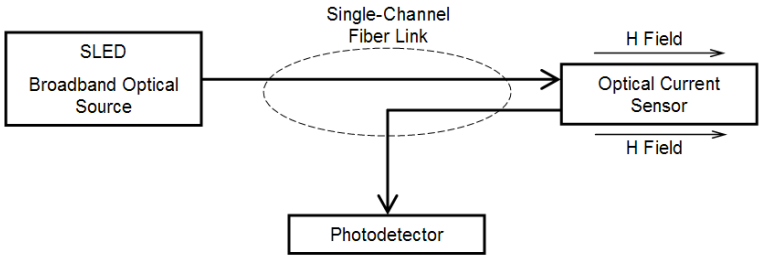

Fig. 1.7: Simplified diagram of the experimental setup

1.7 THESIS ORGANIZATION

In this thesis, the experimental set up and the sensor manufacturing process will be described in details. In addition, several models have been proposed to model the magnetostriction and the magnetization process in T-D. Furthermore, the results of the proposed models and the experimental results are discussed and analyzed. The thesis is organized in eight chapters. The first Chapter presents an overview of the optical current sensor technology and the thesis outline. The

second Chapter provides a basic background of the FBG theory for uniform gratings. Then the numerical methods for simulating the FBG spectral responses are discussed. The third Chapter presents models for the magnetostriction in T-D that have been used and developed basing on free magnetic energy l. The Chapter four explains the use of COMSOL Multiphysics software to model the magnetostriction in T-D and different methods and simulation techniques employed. The design and modeling of fiber optical current sensors will be discussed in the Chapter five. In the Chapter five, experimental procedure with different components such as photodiode circuit, OSA, and magnetometer is described. A detailed procedure for sensor manufacturing is documented in the Chapter six. The Chapter seven discusses the results of the different simulation techniques and presents the experimental data. Then the simulation results and the experimental data will be compared and analyzed. Finally, the thesis concludes by summarizing results and recommending more accurate sensor models and experiment procedure for future projects in the Chapter eight.

2. FBG THEORY AND MODELING

2.1 PROPERTIES AND TYPES OF BRAGG GRATINGS

Numerous papers and articles have described the advancements in optical-fiber technology and their use in sensing and amplification [19], [20], [21]. FBGs are excellent device for sensing strain for various applications. Readiness for integration with an optical network, low cost, and low insertion loss are some of the advantages of the FBG over other competing technologies [19].

Common Bragg reflector, blazed Bragg grating, and chirped Bragg grating are the most common types of FBG structures. The grating pitch (the spacing between the gratings planes), the tilt (the angle between the grating planes) and the fiber axis are the parameters used for distinguishing among the different types of Bragg grating structures. The simplest and most popular Bragg reflector is the one with uniform grating period, i.e. the uniform fiber grating, illustrated in the Fig. 2.1 where the phase fronts are perpendicular to the fiber longitudinal axis. This type of Bragg grating has been used in many applications such as strain and temperature sensing. It has also been used as a tunable filter.

In the blazed Bragg grating the grating planes are written at certain angles to the fiber axis, this will cause some radiation modes outside the fiber. In this case, specific wavelengths and modes emerge at certain angles. On the other hand, axial variation of either the period of the grating Λ or the refraction index of the core leads to the formation of chirped Bragg grating.

The Bragg wavelength, λ_B, an important parameter for the FBG, is defined as the free space central wavelength of the reflected optical signal from the FBG where maximum reflection occurs. The Bragg wavelength can be determined by:

$$\lambda_B = 2n_{eff}\Lambda \tag{2.1}$$

where n_{eff} is the effective refractive index of the fiber core at λ_B, Λ is the grating spacing, and L is the length of the grating as shown in Fig. 2.1. When an optical signal with different wavelengths $\lambda_1 - \lambda_7$ enters the FBG, all wavelengths of light will be transmitted through the FBG except the wavelength that satisfy the Bragg condition λ_B will be reflected back.

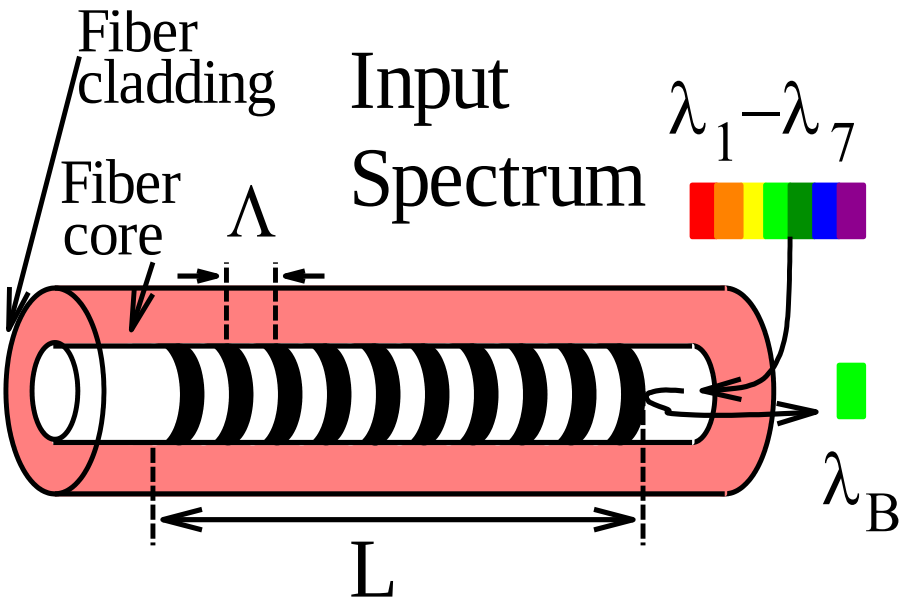

Fig. 2.1: Illustration of a uniform Bragg grating with a periodic index modulation.

The spectral response of a uniform, chirped, or apodized Bragg grating can be calculated through numerical solution of the coupled-mode equations or through approximation methods, such as the transfer matrix (T-matrix) method [19, 20].

2.2 COUPLED-MODE THEOTY

The Bragg grating is defined as a periodical perturbation to the effective index of refraction n_{eff} of the optical fiber core, which can be written as

$$\delta n_{eff}(z) = \overline{\delta n}_{eff}\left(1 + v(z)\cos\left[\frac{2\pi}{\Lambda}z + \phi(z)\right]\right) \tag{2.2}$$

where $\overline{\delta n}_{eff}$ is the "DC" index change spatially averaged over a grating period, $v(z)$ is the fringe visibility of the index change, z is the fiber axis, and $\phi(z)$ is the grating chirp.

Coupled mode theory is considered as straightforward method to accurately model the optical properties of most fiber gratings. The notations here follow very closely those of [19]. The transverse component of the electric field in the ideal-mode approximation to coupled-mode theory can be written as a superposition of the ideal modes with slowly varying amplitudes $A_j(z)$ and $B_j(z)$ of the j^{th} mode traveling in the +z and –z directions, respectively (modes in an ideal waveguide with no grating perturbation) [19]:

$$\vec{E}(x,y,z,t) = \sum_j \left[A_j(z)\exp(i\beta_j z) + B_j(z)\exp(-i\beta_j z) \right] \overrightarrow{e_{jt}}(x,y)\exp(-i\omega t) \tag{2.3}$$

where $\overrightarrow{e_{jt}}(x,y)$ represents the transverse mode fields for guide LP modes or cladding modes. The amplitudes A_j and B_j evolve along the z axis owing to the presence of the dielectric perturbation as described in the following two equations:

$$\begin{aligned} \frac{dA_j}{dz} &= i\sum_j A_k \left(K_{kj}^t + K_{kj}^z\right)\exp\left[i(\beta_k - \beta_z)z\right] \\ &+ i\sum_j B_k \left(K_{kj}^t - K_{kj}^z\right)\exp\left[-i(\beta_k + \beta_z)z\right] \end{aligned} \tag{2.4}$$

$$\begin{aligned} \frac{dB_j}{dz} &= -i\sum_j A_k \left(K_{kj}^t - K_{kj}^z\right)\exp\left[i(\beta_k + \beta_z)z\right] \\ &- i\sum_j B_k \left(K_{kj}^t + K_{kj}^z\right)\exp\left[-i(\beta_k - \beta_z)z\right] \end{aligned} \tag{2.5}$$

In the above two equations K_{kj}^z is the longitudinal coupling coefficient, K_{kj}^t is the transverse coupling coefficient between modes j and k. It can be described by:

$$K_{kj}^{t}(z) = \frac{\omega}{4} \iint_{-\infty}^{\infty} \vec{e}_{kt}(x,y)\, \Delta\epsilon(x,y,z) \cdot \vec{e}_{jt}(x,y) dxdy \tag{2.6}$$

where $\Delta\varepsilon$ is the perturbation to the permittivity. Generally $K_{kj}^{z} \ll K_{kj}^{t}$ for fiber modes and it is usually neglected.

The above coupled mode theory equations may be used to solve the total transverse electric fields propagating in the forward and backward directions. Equations (2.4) and (2.5) can be greatly simplified if we consider only one pair of forward and backward propagation modes. For a Bragg grating etched in a single-mode optical fiber, the following coupled differential equations can be used to model forward (*R*) and backward (*S*) propagation modes through the grating (*z* is the propagation distance):

$$\frac{dR}{dz} = i\hat{\sigma}R(z) + i\kappa S(z) \tag{2.7}$$

$$\frac{dS}{dz} = -i\hat{\sigma}S(z) - i\kappa^{*}R(z) \tag{2.8}$$

In Eqs. (2.7) and (2.8),

$$\kappa = \frac{\pi}{\lambda} v\overline{\delta n}_{eff} \tag{2.9}$$

$$\hat{\sigma} = \delta + \sigma - \frac{1}{2}\frac{d\phi}{dz} \tag{2.10}$$

$$\delta \equiv \beta - \frac{\pi}{\Lambda} = \beta - \beta_{D} = 2\pi n_{eff}\left(\frac{1}{\lambda} - \frac{1}{\lambda_{D}}\right) \tag{2.11}$$

$$\lambda_{D} \equiv 2n_{eff}\Lambda \tag{2.12}$$

$$\sigma = \frac{2\pi}{\lambda}\overline{\delta n_{eff}} \tag{2.13}$$

Where κ is the "AC" cross-coupling coefficient, $\hat{\sigma}$ is the "DC" self-coupling coefficient, and λ_{D} is the design wavelength. The amplitudes R and S are;

$$R(z) = A(z)e^{i\delta z - \frac{\phi}{2}} \tag{2.14}$$

$$S(z) = B(z)e^{-i\delta z + \frac{\phi}{2}} \tag{2.15}$$

If the grating is uniform then $d\phi / dz = 0$, and thus $\kappa, \sigma, \overline{\delta n_{eff}}$, and $\hat{\sigma}$ are all constants. A Bragg grating with length of L has an extent of $(-L/2) \le z \le (L/2)$ under boundary conditions $R(-L/2) = 1$ and $S(L/2) = 0$. Then the field reflection coefficient $\rho = \frac{S(-L/2)}{R(-L/2)}$ for the grating can be simply expressed in terms of FBG parameters as:

$$\rho = -\frac{\kappa}{\hat{\sigma} + i\alpha \coth \alpha L} \tag{2.16}$$

where $\alpha = \sqrt{\kappa^2 - \hat{\sigma}^2}$. The power reflectivity $r = |\rho|^2$ is then given by

$$r = \frac{1}{-\frac{\hat{\sigma}^2}{\kappa^2} \operatorname{csch}^2 \alpha L + \coth^2 \alpha L} \tag{2.17}$$

It can be seen from equation (2.17) that the resultant reflectivity increases as the length of the grating increases. Fig. 2.2 shows a calculated reflection spectrum as a function of the wavelength.

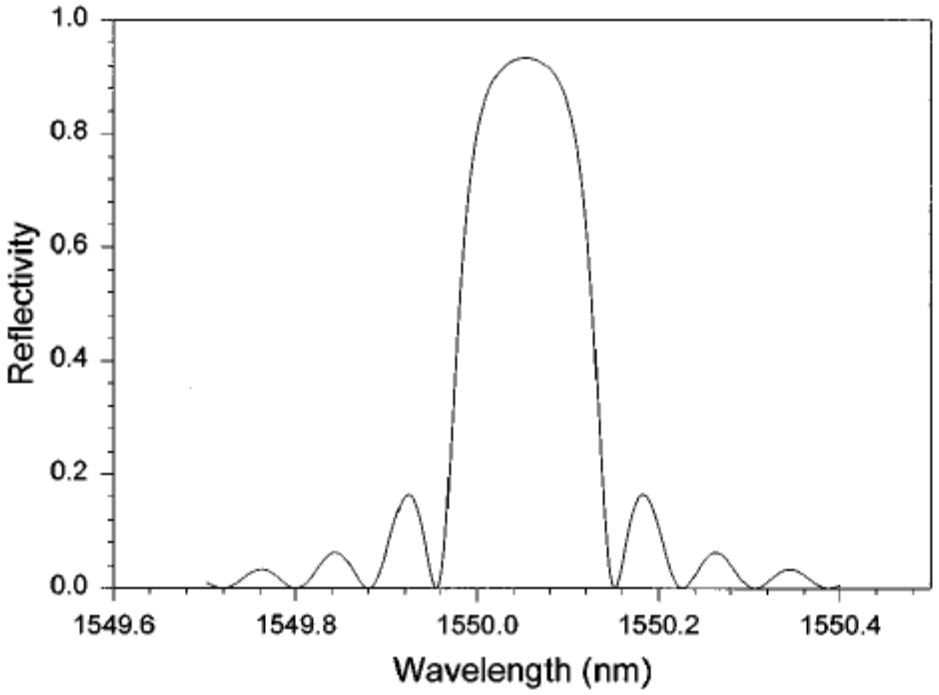

Fig. 2.2: Bragg grating reflection spectrum as a function of wavelength detuning [20].

2.3 TRANSFER MATRIX APPROXIMATION

Alternatively the transfer matrix (T-matrix) approximation method can be used to model Bragg gratings with varying parameters. Piecewise uniformity is assumed in this approach. In this method, the grating is divided into *M* uniform sections, each represented by a 2x2 T-matrix. The number of sections cannot be made arbitrarily large since several grating periods are required for complete coupling. M ~ 100 is sufficiently accurate for most chirped and apodized gratings [19]. It is required that the section length $\Delta z \gg \Lambda$ to keep the coupled-mode-theory approximation valid. Therefore, it is required that

$$M \ll \frac{2n_{eff}L}{\lambda_B}. \tag{2.18}$$

For simulations of our FOCS, 5 sections are used. The transfer matrix of the m^{th} section is given by

$$\mathbf{T}_m$$

$$= \begin{bmatrix} \cosh(\gamma_m \Delta z_m) - i\frac{\hat{\sigma}_m}{\gamma_m}\sinh(\gamma_m \Delta z_m) & -i\frac{\kappa_m}{\gamma_m}\sinh(\gamma_m \Delta z_m) \\ i\frac{\kappa_m}{\gamma_m}\sinh(\gamma_m \Delta z_m) & \cosh(\gamma_m \Delta z_m) + i\frac{\hat{\sigma}_m}{\gamma_m}\sinh(\gamma_m \Delta z_m) \end{bmatrix}. \quad (2.19)$$

Here, Δz_m is the width of the m^{th} section, $\gamma_m = \sqrt{-\hat{\sigma}_m^2}$, $\hat{\sigma}_m$, and κ_m are the same parameters as those defined in Eqs. (2.7) and (2.8), evaluated at the middle of the m^{th} section. Once all the matrices for each individual section are known, we can find the output amplitudes from.

$$\begin{bmatrix} R_M \\ S_M \end{bmatrix} = \mathbf{T}\begin{bmatrix} R_0 \\ S_0 \end{bmatrix} \quad (2.20)$$

This means that the whole FBG can be characterized by a total matrix **T** which is equal to the multiplication of all of the matrices of the subsections, i.e.

$$\mathbf{T} = \begin{bmatrix} t_{11} & t_{12} \\ t_{21} & t_{22} \end{bmatrix} \quad (2.21)$$

$$\mathbf{T} = \mathbf{T}_M \mathbf{T}_{M-1} \ldots \mathbf{T}_m \ldots \mathbf{T}_1 \quad (2.22)$$

This method can be used to implement phase-shifted gratings by inserting a phase-shift matrix $\mathbf{T}_{pm}$ between the factors $\mathbf{T}_m$ and $\mathbf{T}_{m+1}$ in the product in (2.22) for a phase shift after the m^{th} section. The phase shift matrix is of the form

$$\mathbf{T}_{pm} = \begin{bmatrix} \exp\left(\frac{-i\phi_m}{2}\right) & 0 \\ 0 & \exp\left(\frac{-i\phi_m}{2}\right) \end{bmatrix} \quad (2.23)$$

Fig. 2.3 shows the reflection spectral response for three uniform FBGs of various lengths that have been calculated using the T-matrix [21].

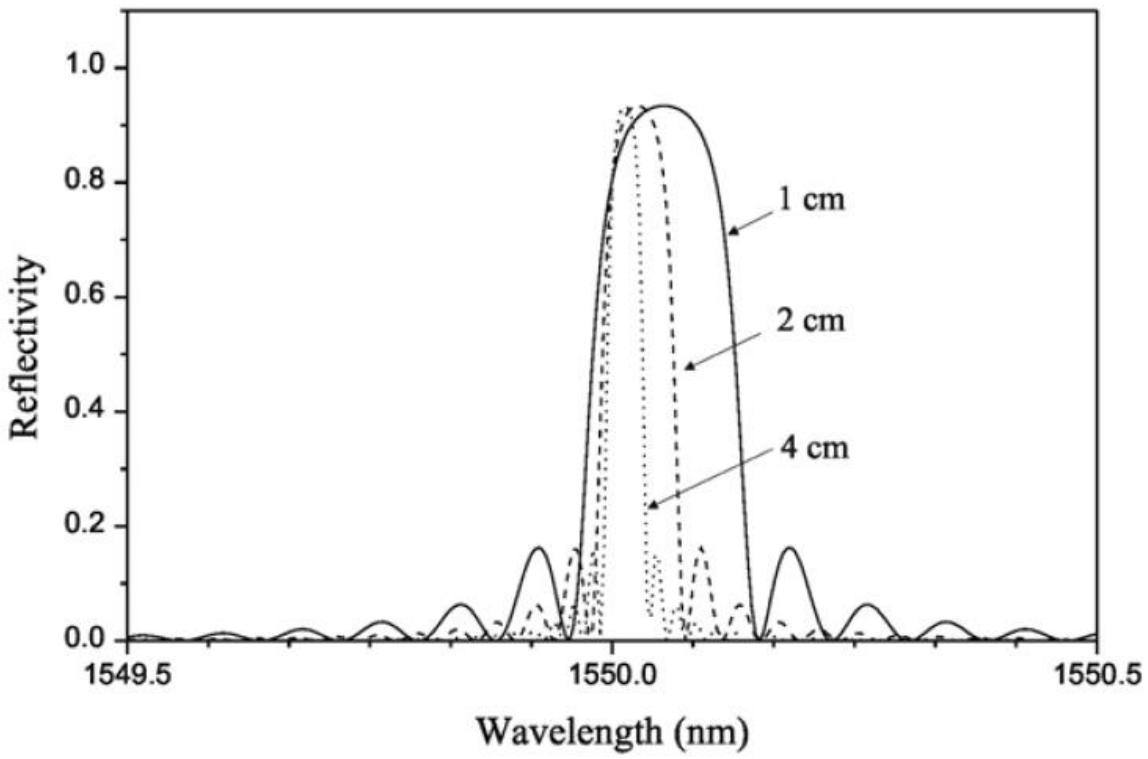

Fig. 2.3: Spectral reflectivity response for uniform Bragg gratings with different lengths [20].

2.4 STRAIN AND TEMPERATURE SENSITIVITY OF BRAGG GRATINGS

When a stress is applied to the FBG, it can affect the refractive index of the core and the periodic spacing between the grating planes. Based on equation (2.1), the shift in the Bragg wavelength $\Delta\lambda_B$ of the FBG under an applied stress can be expressed by:

$$\Delta\lambda_B = 2\left(\Lambda\frac{\partial n}{\partial l} + n\frac{\partial\Lambda}{\partial l}\right)\Delta l \tag{2.24}$$

This equation can further be expressed in terms of axial strain ϵ_z as:

$$\Delta\lambda_B = \lambda_B\left(1-p_e\right)\varepsilon_z \tag{2.25}$$

where p_e is the effective strain-optic constant which can be defined as:

$$p_e = \frac{n^2}{2}\left[p_{12} - \nu\left(p_{11} + p_{12} \right) \right] \tag{2.26}$$

Where p_{11} and p_{12} are the components of the strain-optic tensor, n is the index of the core, and ν is the Poisson's ratio. For a typical optical fiber $p_{11} = 0.113, p_{12} = 0.252, \nu = 0.16,$ and n = 1.482 [20].

To represent the temperature effect on the optical fiber a second term should be added to equation (2.24), then the shift in the Bragg grating center wavelength will be given by

$$\Delta\lambda_B = 2\left(\Lambda \frac{\partial n}{\partial l} + n\frac{\partial \Lambda}{\partial l} \right)\Delta l + 2\left(\Lambda \frac{\partial n}{\partial T} + n\frac{\partial \Lambda}{\partial T} \right)\Delta T \tag{2.27}$$

2.5 SIMULATION OF SPECTRAL RESPONSE FROM BRAGG GRATINGS

The Bragg grating as a strain sensor can assume non-uniform grating period for the following conditions [21]: (i) an initially uniform (constant period) grating is subjected to a non-uniform strain field, (ii) an initially chirped (aperiodic) grating is subjected to a constant strain field, and (iii) an initially chirped grating is subjected to a non-uniform strain field. Eqs. (2.7) and (2.8) can be solved numerically to model these conditions. They can be transformed into a Ricatti differential equation by introducing $\rho(z) = S(z) / R(z)$. Differentiating ρ with respect to z and substituting into Eqs. (2.7) and (2.8) yields

$$\frac{d\rho(z)}{dz} = -i\kappa - 2i\hat{\sigma}\rho(z) - i\kappa\rho(z)^2 \tag{2.28}$$

with the modified boundary condition $\rho(L/2) = 0$. A fourth-order Runge-Kutta method with adaptive step size can numerically solve Eqs. (2.7), (2.8) or Eq. (2.28) by integrating backward from $z = L/2$ to $z = -L/2$. The power reflectivity of the Bragg grating is then obtained with

$$r(\lambda) = \left| \frac{S\left(\frac{-L}{2}\right)}{R\left(\frac{-L}{2}\right)} \right|^2 = \left| \rho\left(\frac{-L}{2}\right) \right|^2 \tag{2.29}$$

Alternatively we can use the transfer matrix which sufficiently accurate and faster than the previous method. The field reflection coefficient can be determined as $\rho = t_{21} / t_{11}$ with the transfer matrix method.

With the theory that has been explained above, we were able to simulate the spectral response of the sensor shown in Fig. 1.5 which consists of the FBG embedded in composite blocks with different distributions of T-D particles. However, we consider monolithic T-D with varying magnetostrictive strain to represent the composite blocks. In Figs. 2.4 and Fig 2.5, we use the following FBG parameters: effective refractive index $n_{eff} = 1.46547$, unchirped Bragg wavelength λ_B = 1550 nm, number of uniform sections M=5, and overall length L = 3cm. Fig. 2.4 shows the spectral reflectivity as a function of the percentage of deviation from λ_B is $\overline{\Delta\lambda} = (\lambda - \lambda_B)/\lambda_B$ for various H's. Fig. 2.5 presents the FOCS transfer function in terms of normalized power $\overline{P} = \left[P(H) - P(0) \right] / P(0)$ where $P(H)$ is the reflected power at particular H from Fig. 2.4 and $P(0)$ is the power at H=0.

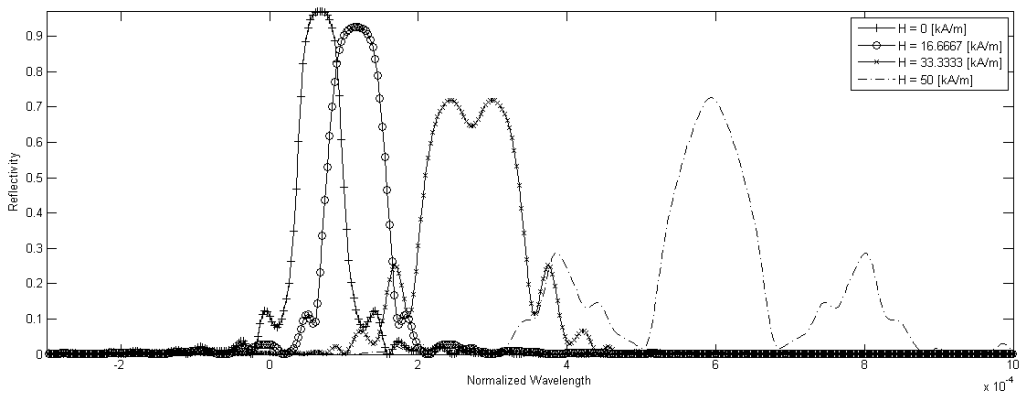

Fig. 2.4: Variation of spectral reflectivity with magnetic field (H) in chirped FOCS.

In Fig. 2.4, as *H* increases, the bandwidth of the reflected optical signal increases. The rise in bandwidth translates into increases in returned power (the area under each spectrum). As a result, the chirped FOCS will respond to a wide range of *H* without saturation as it can be seen in Fig. 2.5.

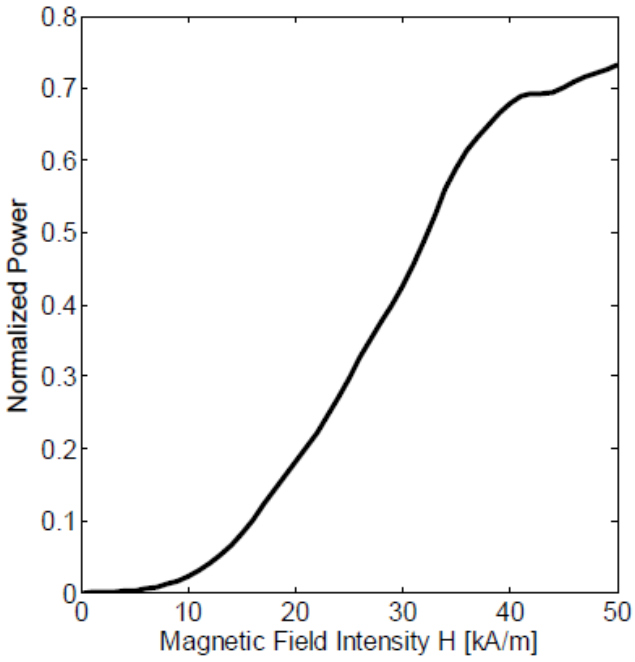

Fig. 2.5: Response of the chirped FOCS.

The numerical simulation in Fig. 2.4 and Fig. 2.5 were performed using Matlab to find the reflectance spectrum. Modeling of chirped FBG is based on the "synchronous approximation" to the coupled mode equations describing forward – and backward propagation modes in the fiber at wavelengths near resonance. Since the FOCS prototype in Fig. 1.5 is composed of a composite with a piece-wise graded particle distribution it is natural to consider a uniform structure for the grating, and the power reflectance at each wavelength is determined by multiplication of a series of transfer matrices. With this numerical technique, the power spectra of the FOCS returned signals under various magnetic fields H were obtained as shown in Fig. 2.4.

3. MAGNETIZATION AND MAGNETOSTRICTION IN TERFENOL-D

3.1 TERFENOL-D MATERIAL BEHAVIOR

It is imperative to examine the material behavior models of T-D in order to understand the experimental results and to optimize the transducer performance. The simplest model that has been used to explain the magnetostriction in T-D is the ellipsoid model in which magnetic domains are represented by ellipsoids with the magnetization direction pointing towards the major axis for T-D since it has positive magnetostriction as shown in Fig. 3.1. Assuming that the ellipsoids have rigid structure, then the magnetization can be rotated with either an applied field or an applied strain [15].

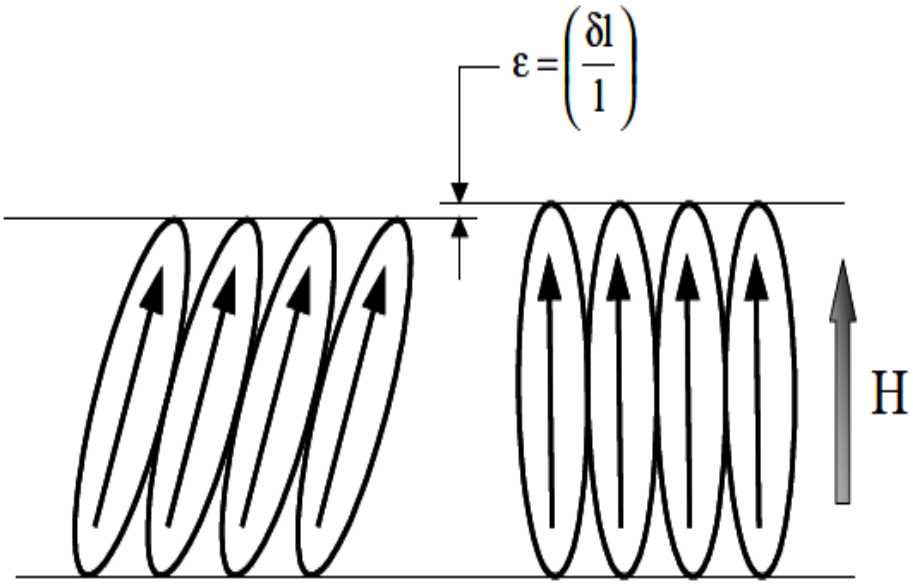

Fig. 3.1: The ellipsoid model of magnetostriction [15].

This model is capable of explaining the effect of pre-stress and how it can increase the magnetostriction; if a stress is applied first to the material such that the ellipsoids are rotated away

from the applied stress, then we apply a magnetic field in the direction of the applied pre-stress the resulting magnetostriction will be larger than if the pre-stress had not been applied. While the ellipsoid model enabled us to describe and explain certain T-D behavior, it is incapable of handling more complicated phenomena. For these complex situations, other models have been proposed. These models are based on the minimization of the free energy of a magnetoelastic system. It is necessary to review the crystal structure of T-D before we explain these models.

3.2 TERFENOL-D CRYSTAL STRUCTURE

For the crystalline structure of T-D, following vector conventions are used: planes are denoted by round bracket, directional indices are represented by square brackets, and angular brackets are used to summarize an entire set of indices. T-D has a cubic crystal structure and the magnetic moments prefer to align along the <111> orientations when no stress or field is applied due to the negative anisotropy constant. In other words, the <111> directions are the easy magnetization axes, as schematically illustrated in Fig. 3.2. The term magnetic anisotropy refers to the dependence of magnetic properties on the direction in which they are measured. There are several kinds of magnetic anisotropy such as magnetocrystalline anisotropy, stress anisotropy, and shape anisotropy [22]. T-D has a large magnetostriction anisotropy, where the strain along the <111> directions is much larger than the <100> direction ($\lambda_{111} = 1640$ ppm, $\lambda_{100} = 90$ ppm). T-D rods can be manufactured with <111>, <110>, or <112> preferred orientations. In thermal demagnetized <111>, <110>, and <112> Tb-Dy-Fe single crystal, there are eight kinds of magnetic moments along the <111> directions. The different domains are named by the angles between the crystal axes and the <111> directions to which the domains orient in thermal demagnetized state. Those different domains are shown in the tables below for different crystal axes.

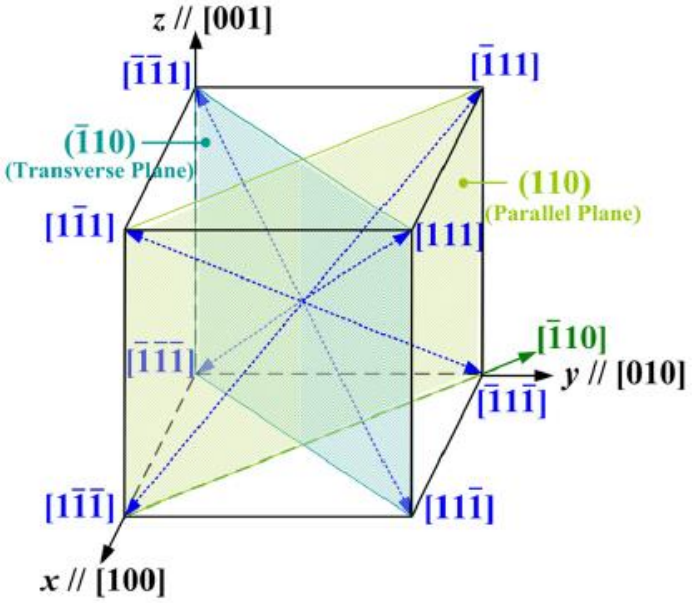

Fig. 3.2: sketch of <111>easy axes in the cubic principal axes space [23].

Crystal axis is [111]	
Domain configuration	Angle w/s crystal axis
[111]	0°
[-1-1-1]	180°
[-111]	71°
[1-1-1]	109°
[1-11]	71°
[-11-1]	109°
[11-1]	71°
[-1-11]	109°

Table 3.1: Eight domains in the <111> Tb-Dy-Fe single crystal

Crystal axis is [112]	
Domain configuration	Angle w/s crystal axis
[111]	19.5°
[-1-1-1]	160.5°
[-111]	62°
[1-1-1]	118°
[1-11]	62°
[-11-1]	118°
[11-1]	90°
[-1-11]	90°

Table 3.2: Eight domains in the <112> Tb-Dy-Fe single crystal

Crystal axis is [110]	
Domain configuration	Angle w/s crystal axis
[111]	35°
[-1-1-1]	145°
[-111]	90°
[1-1-1]	90°
[1-11]	90°
[-11-1]	90°
[11-1]	35°
[-1-11]	145°

Table 3.3: Eight domains in the <110> Tb-Dy-Fe single crystal

The angles in the above tables have been calculated as follows: Suppose we have two vectors [x,y,z] and [u,v,w] then the angle between those two vectors is:

$$\cos\theta = \frac{x.u + y.v + z.w}{\sqrt{x^2 + y^2 + z^2}\sqrt{u^2 + v^2 + w^2}}$$

Example:

$[111] \Rightarrow [\bar{1}10]$

$$\theta = \cos^{-1}\left(\frac{1\times -1+1\times 1+1\times 0}{\sqrt{1+1+1}\sqrt{(-1)^2+1^2}}\right) = \cos^{-1}(0)$$

$$\Rightarrow \theta = 90^{\circ}$$

3.3 MAGNETIZATION AND MAGNETOSTRICTION MODELS BASED ON FREE ENERGY

Numerous articles have been written to describe the magnetization and magnetostriction of T-D, such as in Refs. [24] [25] [26] [27]. Some are based on purely physical principles while others model the magnetostriction and the magnetostriction processes using the phenomenological approach. The Stoner-Wohlfath model is the simplest model to describe the magnetization and the magnetostriction processes [28]. The model assumes that the material is composed of non-interacting single domain ellipsoidal particles. According to this model, the orientation of the magnetization vector with respect to the measurement direction can be found by minimizing the total free energy which in this case is due to the shape of the particles and the applied field. At T = 0 K, the total energy can be written as [28]:

$$E = E_A + E_z = K\sin^2\theta - HM_s\cos(\theta - \phi) \qquad (3.1)$$

The term E_A refers to the anisotropy energy which is given by the term $K\sin^2\theta$ where θ is the angle between the magnetization and the z-axis. If $K > 0$ the anisotropy energy will be minimum when $\theta = 0$. The term $E_z = -\vec{M}\cdot\vec{H} = -HM_s\cos(\theta - \phi)$ represents the Zeeman energy. ϕ is the angle between the external magnetic field and the easy axis, where H is the external applied

magnetic field, M is the magnetization, and M_s is the saturation magnetization. The moment is along a direction such that the total energy E is minimized. The minimal condition at θ^* is

$$\left(\frac{\partial E}{\partial \theta}\right)_{\theta=\theta^*} = 0 \text{ and } \left(\frac{\partial^2 E}{\partial \theta^2}\right)_{\theta=\theta^*} > 0 \tag{3.2}$$

The Stoner-Wohlfath model works best for non-ferromagnetic metals and alloys that contain ferromagnetic impurities. The results of this model cannot be applied to T-D which exhibits low hysteresis.

For the phenomenological approach, the magnetic domain in a single-crystal ferromagnetic material is extremely dependent on extrinsic variables such as the strength and direction of magnetic field, stress, as well as intrinsic material parameters such as the anisotropy of the material.

Without the magnetic domain interaction, the equilibrium positions (also considered as magnetization orientations) for the cubic T-D can be simply determined by the local minima of the total free magnetic energy, which can be expressed as

$$E_{total} = E_K + E_{field} + E_\sigma \tag{3.3}$$

where E_K, E_{field}, and E_σ are the magnetocrystalline anisotropy energy, the external magnetic field energy, and the stress induced magnetoelastic energy respectively. For T-D, the magnetocrystalline anisotropy energy is given by [29]

$$E_K = K_0 + K_1 \sum_{i<j}^{3} \alpha_i^2 \alpha_j^2 + K_2 \alpha_1^2 \alpha_2^2 \alpha_3^2 = K_0 + K_1 \left(\alpha_1^2 \alpha_2^2 + \alpha_2^2 \alpha_3^2 + \alpha_3^2 \alpha_1^2\right) + K_2 \alpha_1^2 \alpha_2^2 \alpha_3^2 \tag{3.4}$$

where α_i denotes the direction cosine of the magnetization with respect to the crystal axes <100>, <010>, and <001> and K_0, K_1, K_2 are the zero-order, first-order and second-order magnetocrystalline anisotropy constants respectively. The external magnetic field energy can be written as:

$$E_{field} = -\mu_0 H M_s \sum_{i=1}^{3} \alpha_i \beta_i \tag{3.5}$$

H denotes the magnetic field, and β_i is the direction cosine of the magnetic field with respect to the crystal axes, and μ_0 is the of free space magnetic permeability. The strain induced magentoelastic energy is given by:

$$E_\sigma = -\frac{3}{2}\lambda_{100}(\alpha_1^2\sigma_{11} + \alpha_2^2\sigma_{22} + \alpha_3^2\sigma_{33}) - 3\lambda_{111}(\alpha_1\alpha_2\sigma_{12} + \alpha_2\alpha_3\sigma_{23} + \alpha_1\alpha_3\sigma_{13}) \tag{3.6}$$

λ_{100} and λ_{111} are the saturation values of the longitudinal magnetostriction along [100] and [111], respectively. σ_{ij} denotes the component of the applied stress.

When the sample is subjected to the uni-axial stress σ, the above equation can be simplified as

$$E_\sigma = -\frac{3}{2}\sigma\lambda_{100}\sum_{i=1}^{3}\alpha_i^2\gamma_i^2 - 3\sigma\lambda_{111}\sum_{i<j}^{3}\alpha_i\alpha_j\gamma_i\gamma_j. \tag{3.7}$$

Or it can be written as

$$E_\sigma = -\frac{3}{2}\sigma\lambda_{100}(\alpha_1^2\gamma_1^2 + \alpha_2^2\gamma_2^2 + \alpha_3^2\gamma_3^2) - 3\sigma\lambda_{111}(\alpha_1\alpha_2\gamma_1\gamma_2 + \alpha_2\alpha_3\gamma_2\gamma_3 + \alpha_1\alpha_3\gamma_1\gamma_3). \tag{3.8}$$

γ_i is the direction cosine of the stress with respect to the crystal axes. The following table summarizes the properties of T-D.

M_s, saturation magnetization	$0.8\times10^6 A/m$
K_0	$3\times10^5 J/m^3$
K_1,magnetocrystalline anisotropy	$-0.06\times10^6 J/m^3$
K_2	$-2\times10^5 J/m^3$
λ_{111}	$1640\times10^{-6} mm/mm$
λ_{100}	$90\times10^{-6} mm/mm$

Table 3.4: Physical properties of T-D crystal [30].

Armstrong [30][31], formulated a model for T-D where bulk magnetization and strain are calculated as the expected value of a number of possible energy states or domain orientations with energy based probability density function. The model evaluates the magnetic free energy of a unit volume of magnetization, M_s at a spherical polar orientation of $[\theta_m,\phi_m]$ within a single crystal. The above expression for the energy terms can be rewritten in terms of θ and ϕ where θ is defined as the polar angle from z axis with $0 \le \theta \le \pi$, and φ is the azimuthal angle on the x-y plane measuring from the x axis with $0 \le \varphi \le 2\pi$.

For the magnetocrystalline energy:

$$\alpha_1 = \sin[\theta_m]\cos[\phi_m]$$
$$\alpha_2 = \sin[\theta_m]\sin[\phi_m]$$
$$\alpha_3 = \cos[\theta_m]$$

$$E_K = K_0 + K_1\begin{Bmatrix}(\sin[\theta_m]\cos[\phi_m])^2(\sin[\theta_m]\sin[\phi_m])^2\\ +(\sin[\theta_m]\sin[\phi_m])^2\cos^2[\theta_m]\\ +\cos^2[\theta_m](\sin[\theta_m]\cos[\phi_m])^2\end{Bmatrix} \qquad (3.9)$$
$$+K_2\left\{(\sin[\theta_m]\cos[\phi_m])^2(\sin[\theta_m]\sin[\phi_m])^2\cos^2[\theta_m]\right\}$$

where $[\theta_m, \phi_m]$ is the magnetization direction in spherical polar coordinates. The field contribution to the magnetic free energy is:

$$E_{field} = -\mu_0 M_s H \times \begin{Bmatrix} (\sin[\theta_m]\cos[\phi_m])(\sin[\theta_f]\cos[\phi_f]) \\ +(\sin[\theta_m]\sin[\phi_m])(\sin[\theta_f]\sin[\phi_f]) \\ +\cos[\theta_m]\cos[\theta_f]) \end{Bmatrix} \tag{3.10}$$

$$\beta_1 = \sin[\theta_f]\cos[\phi_f]$$
$$\beta_2 = \sin[\theta_f]\sin[\phi_f]$$
$$\beta_3 = \cos[\theta_f]$$

where H is the field strength and $[\theta_f, \phi_f]$ is the applied field orientation. When the magnetization and the applied field are perpendicular, the field energy is zero. On the other hand, the energy is at maximum negative value when the magnetization and the applied field are parallel. In a similar manner, the stress induced magnetoelastic energy for cubic crystal can be expressed as follow [30]:

$$E_\sigma = \begin{Bmatrix} -(3/2)\lambda_{100}\sigma \begin{Bmatrix} (\sin[\theta_m]\cos[\phi_m])^2(\sin[\theta_\sigma]\cos[\phi_\sigma])^2 \\ +(\sin[\theta_m]\sin[\phi_m])^2(\sin[\theta_\sigma]\sin[\phi_\sigma])^2 \\ +\cos^2[\theta_m]\cos^2[\theta_\sigma] \end{Bmatrix} \\ -3\lambda_{111}\sigma \begin{Bmatrix} (\sin[\theta_m]\cos[\phi_m])(\sin[\theta_m]\sin[\phi_m])(\sin[\theta_\sigma]\cos[\phi_\sigma])(\sin[\theta_\sigma]\sin[\phi_\sigma]) \\ (\sin[\theta_m]\sin[\phi_m])\cos[\theta_m](\sin[\theta_\sigma]\sin[\phi_\sigma])\cos[\theta_\sigma] \\ +\cos[\theta_m](\sin[\theta_m]\cos[\phi_m])\cos[\theta_\sigma](\sin[\theta_\sigma]\sin[\phi_\sigma]) \end{Bmatrix} \end{Bmatrix} \tag{3.11}$$

$[\theta_\sigma, \phi_\sigma]$ is the orientation of the stress, σ.

$$\gamma_1 = \sin[\theta_\sigma]\cos[\phi_\sigma]$$
$$\gamma_2 = \sin[\theta_\sigma]\sin[\phi_\sigma]$$
$$\gamma_3 = \cos[\theta_\sigma]$$

3.4 SIMULATION OF FREE ENERGY DISTRUBTION

In the present simulation, the following assumptions are used, the same as those in previous models [31] [32] [33] [34]:

(1) Perfect TbDyFe single crystals
(2) No internal interaction among domains, and thus neglecting internal stresses produced during magnetization.
(3) Ignoring domain wall movement, only considering domain rotation.

Particularly, if we have the magnetic field applied along the [112] direction, then we can find the direction cosines of the applied field and then we can eventually find the angles θ_f and ϕ_f.

$$\beta_1 = \sin[\theta_f]\cos[\phi_f] = \frac{1}{\sqrt{6}}$$

$$\beta_2 = \sin[\theta_f]\sin[\phi_f] = \frac{1}{\sqrt{6}}$$

$$\beta_3 = \cos[\theta_f] = \frac{2}{\sqrt{6}}$$

So

$$\beta_3 = \cos[\theta_f] = \frac{2}{\sqrt{6}} \Rightarrow \theta_f = \cos^{-1}\left(\frac{2}{\sqrt{6}}\right) = 35.2^\circ$$

$$\beta_2 = \sin[\theta_f]\sin[\phi_f] = \frac{1}{\sqrt{6}} = \sin(35.2^\circ)\sin[\phi_f] \Rightarrow \phi_f = 45^\circ$$

If we assume that the stress is also applied along the [112] direction then

$$\gamma_3 = \cos[\theta_\sigma] = \frac{2}{\sqrt{6}} \Rightarrow \theta_\sigma = \cos^{-1}\left(\frac{2}{\sqrt{6}}\right) = 35.2^\circ$$

$$\gamma_2 = \sin[\theta_\sigma]\sin[\phi_\sigma] = \frac{1}{\sqrt{6}} = \sin(35.2^\circ)\sin[\phi_\sigma] \Rightarrow \phi_\sigma = 45^\circ$$

Now to reduce this model to 2 D we assume that the domain lies in the (110) plane, this plane makes 45degree with the x-axis.

Figs. 3.3 to 3.5 show how the variation of the energy versus angle θ_m, the polar angle of the magnetization from z axis, for various orientations and magnitudes of magnetic field H.

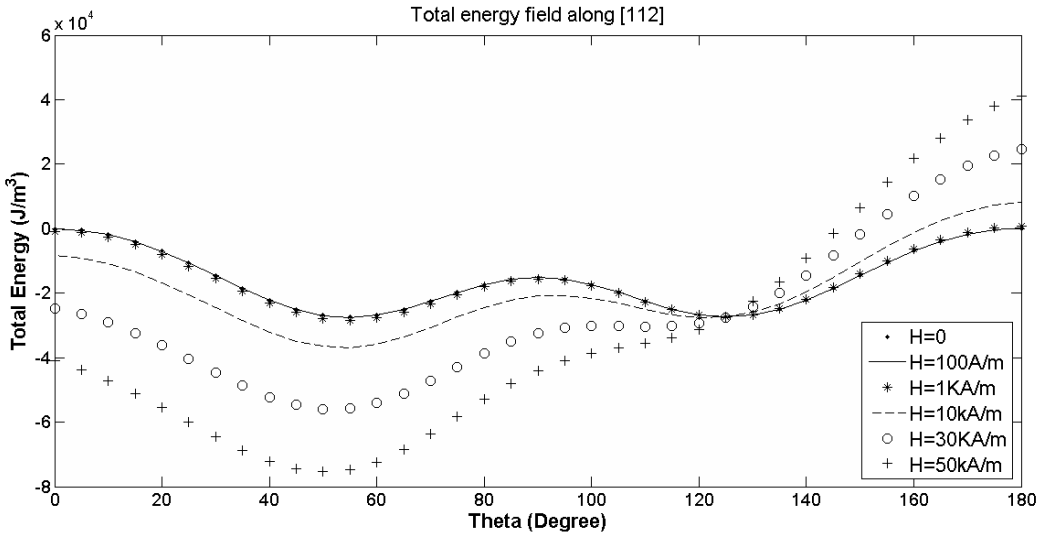

Fig 3.3: Variation of the energy with angle θ_m for different values of the magnetic field. The field orientation is along [112]

Fig 3.3 shows the variation of the energy with angle θ_m for different values of the magnetic field when the field direction is along [112]. It can be seen that at H=0A/m we had two minimum points in the total energy distribution. This means that the domains preferred to align in these two directions where the energy is minimized. However, as the magnetic field intensity increased the domains rotate and aligned with the direction where the magnetic field is applied, i.e. along the [112] direction. As we can see in Fig 3.3 the second minimum point locating around 120º disappears as the intensity of the magnetic field is increased. The same observations can be applied to Fig. 3.4 and 3.5; the only difference between these plots and Fig. 3.3 is the direction of the applied magnetic field.

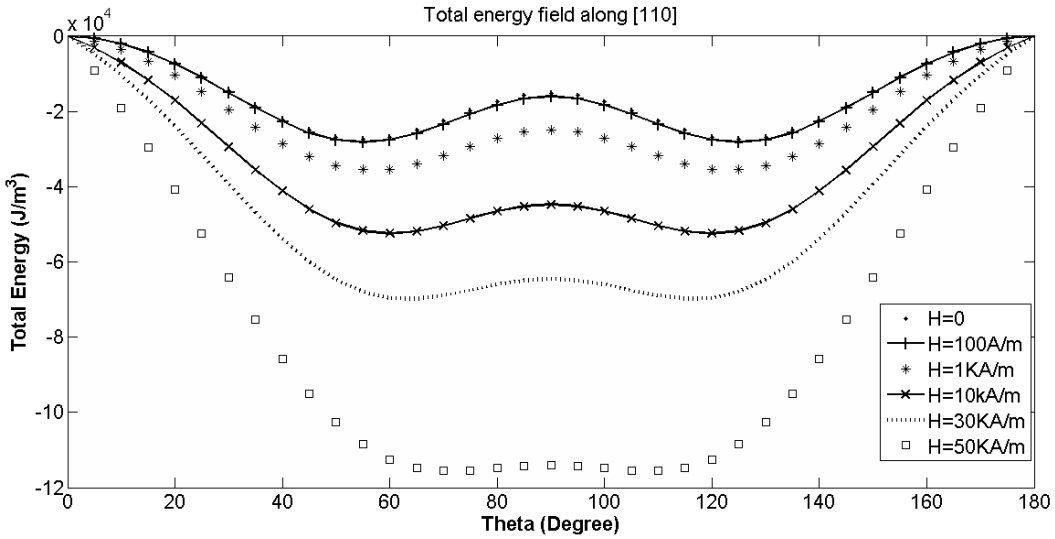

Fig 3.4: Variation of the energy with angle θ_m for different values of the magnetic field. The field orientation is along [110]

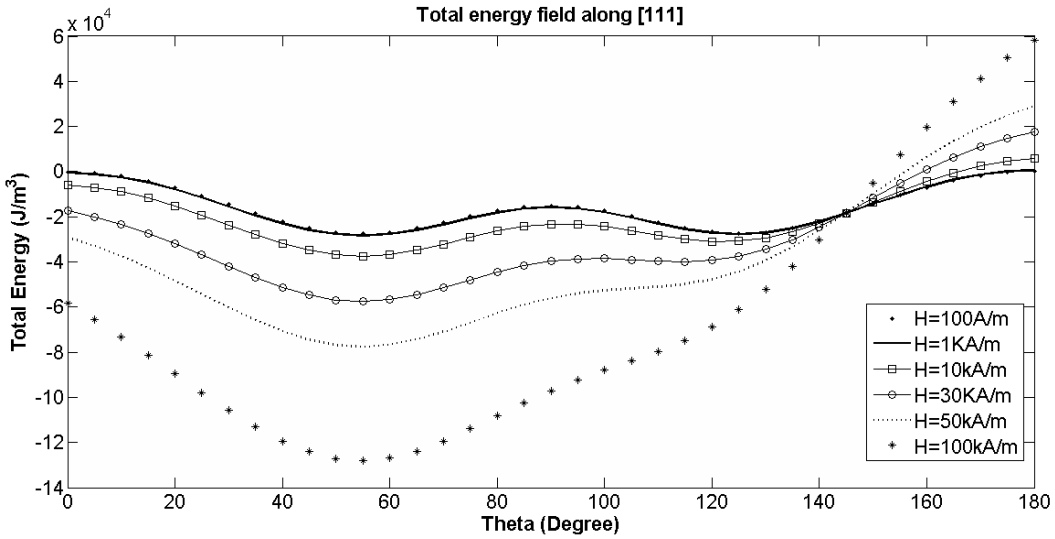

Fig 3.5: Variation of the energy with angle θ_m for different values of the magnetic field. The field orientation is along [111]

Fig. 3.6 shows an example of 3 D simulation for the free energy when the magnetic field and the stress are applied along the [112] direction. In this case H=10kA/m and the applied stress is 5MPa.

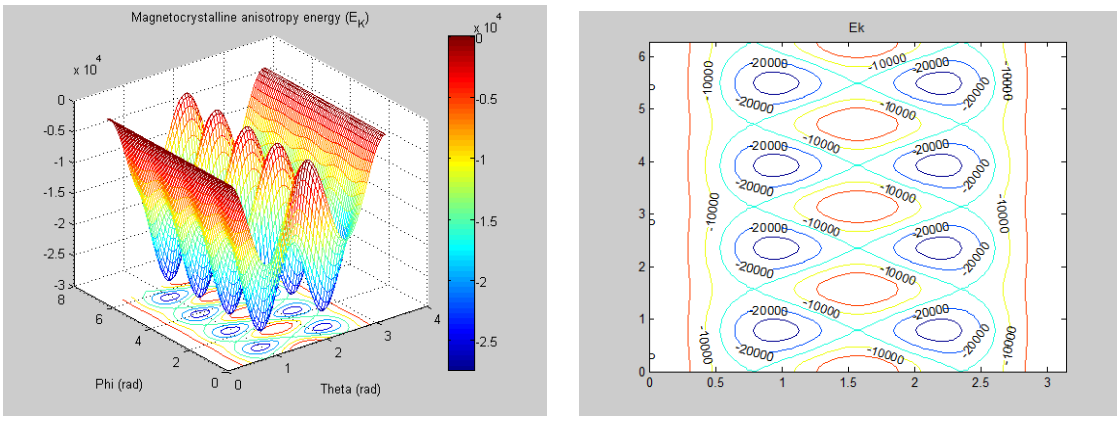

Fig 3.6: Three dimensional energy surface and contour plot of the magnetocrystalline energy.

As shown in the above figure, there are eight minima in the total free energy. If we apply a magnetic field of H=10kA/m and the applied stress is 5MPa, the domains will rotate to follow the new state of minimum free energy, as shown in Fig 3.7.

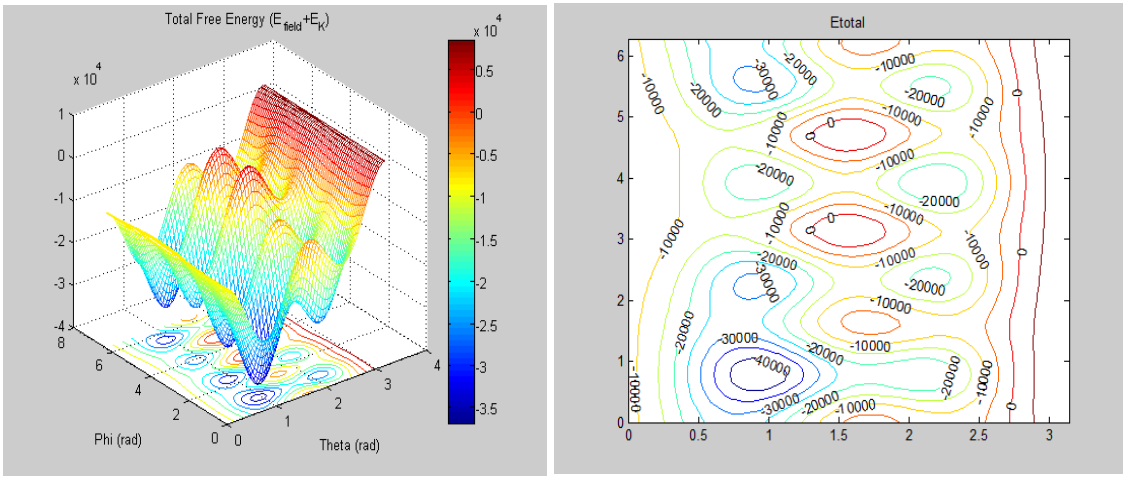

Fig 3.7: Three dimensional energy surface and contour plot of the total energy.

Based on the principles described above, free energy distribution above (001) plane is in demagnetized state i.e. no external stress and magnetic field. As shown in Fig. 3.6, free energy

distribution is symmetry in directions above (001) plane due to T-D alloy with a symmetry cubic structure. It can be seen also that eight points contact with the (001) plane corresponding to eight <111> orientations, consistent with the fact that domains prefer to orient to <111> orientation where the free energy is minimum. The same conclusion can be drawn from the contour plot in Fig. 3.6.

4. TERFENOL-D MAGNETOSTRICTION MODELING WITH COMSOL

Accurate modeling of magnetostrictive materials requires coupling of electrical, mechanical, and magnetic domains. There are very few finite element software packages that include all these physical models. This chapter describes several models that were implemented by combining finite element solutions of mechanical and magnetic boundary value problems with the COMSOL Multiphysics (Finite Element) modeling software. These models describe the magnetomechanical behavior of T-D. An understanding of the mechanical and magnetic characteristics of magnetostrictive materials is essential for the exploration of their potentials in different applications such as transducers.

4.1 MODEL DEFINITION

The first step in creating a finite element model is to create the geometry. Creating the geometry in COMSOL can be done using several methods. COMSOL script can be used to develop the geometry but this method requires the knowledge of geometry creating commands. Geometry can also be created with graphical user interface such as those in COMSOL Multiphysics or any other commercially available drawing software. The geometry for all of the models in this research was created in the COMSOL Multiphysics GUI (version 4.4). Material properties, boundary and loading conditions as well as the meshing were also defined using COMSOL Multiphysics.

The COMSOL models can be used to capture the magnetoelastic behavior of materials subjected to magnetic fields. We have implemented several models to study the nonlinear behavior of monolithic and composite T-D samples. In this Sub-section the graded FOCS model will be investigated. The geometry of the problem is solved as a 2D model as shown in the Fig. 4.1. The model consists of five rectangles representing the epoxy while the ellipses in each rectangle represent the T-D particles with the minor axis of 0.5mm in length and the major axis of 0.7mm

in length. Each block has different number of T-D particles, each block in the model is 7mm×5mm. The volume fraction in the first, second, third, fourth, and fifth block are 0.1, 0.13, 0.16, 0.19, and 0.28 respectively. The gray shaded region with size of a50mm×50mm square represents the air domain enclosing the composite.

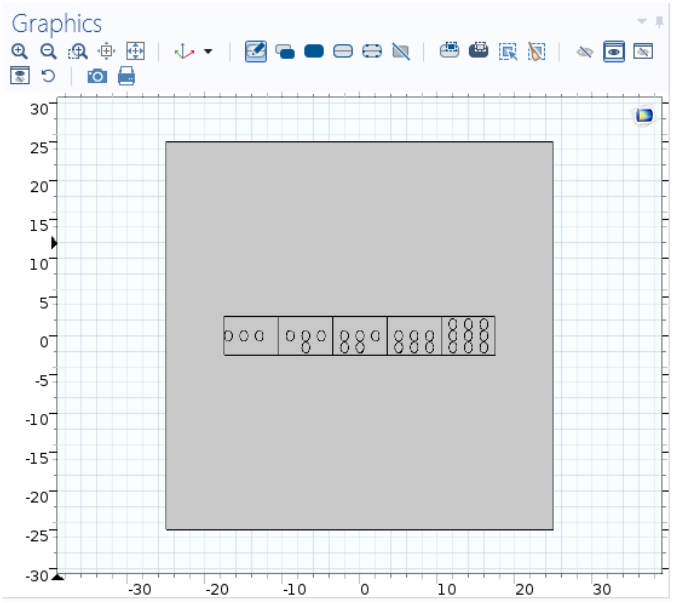

Fig 4.1: 2D view of the graded FOCS surrounded by an air domain. The geometric dimensions are in millimeters.

The purpose of the air domain around the composite T-D blocks is to realistically model the magnetic flux path. Two boundaries of the air domain are magnetically insulated to ensure that flux does not diverge out of the modeling domain. The nonlinear magnetic behavior of the T-D particles is modeled by using a HB curve to specify the magnetic constitutive relation in the magnetostrictive material. The HB data for the T-D material is stored in a table and is imported into COMSOL. Then this table is used to generate a value of the magnetic field (*H*) for a given magnetic flux density (*B*) in the material by interpolation. Other material properties pertinent to T-D are shown in Table 4.1 while the material properties of the epoxy are shown in Table 4.2.

	Property	Name	Value	Unit	Property group
✓	Relative permittivity	epsilonr	1	1	Basic
✓	Young's modulus	E	60e9	Pa	Basic
✓	Poisson's ratio	nu	0.45	1	Basic
✓	Density	rho	7870	kg/m³	Basic
✓	Magnetic field norm	normH	HB(normB[1/T])[A/m]	A/m	HB curve
	Electrical conductivity	sigma	0	S/m	Basic
	Relative permeability	mur	3.5	1	Basic
	normB	normB	sqrt(B1^2+B2^2+B3^2)	T	HB curve

Table 4.1: Material properties of T-D

Property	Variable	Expression	Unit
Electrical conductivity	sigma ; sig...	0	S/m
Relative permittivity	epsilonr ; e...	1	1
Young's modulus	E	3e9	Pa
Poisson's ratio	nu	0.35	1
Density	rho	1000	kg/m³
Relative permeability	mur ; murii...	1	1

Table 4.2: Material properties of the epoxy material

4.2 STRAIN AND MAGNETIC RESPONSES OF T-D

A material model is needed to correctly represent the λ-H and B-H behavior of T-D. COMSOL Multiphysics 4.4 allows the user to input B-H data to describe material magnetic behavior. In earlier versions of COMSOL the behavior of a magnetic material was described in terms of relative permeability μ_r. With newer versions of COMSOL Multiphysics, the model will determine μ_r directly from the B-H plots for each pre-stress. The nonlinear behavior of T-D is modeled by the constitutive model described in [35] [36]. In this model the relations among stress σ, strain ε, and magnetization M along the magnetostrictive composite are given by equation (4.1). In this model, the out-of-plane components of stress are assumed to be zero.

$$\begin{Bmatrix}\varepsilon_x\\ \varepsilon_y\\ \varepsilon_{xy}\end{Bmatrix}=\begin{bmatrix}1/E & -\nu/E & 0\\ -\nu/E & 1/E & 0\\ 0 & 0 & 1/G\end{bmatrix}\begin{Bmatrix}\sigma_x\\ \sigma_y\\ \tau_{xy}\end{Bmatrix}+\frac{\lambda_s}{M_s}\begin{bmatrix}1-\tilde{\sigma}_x/\sigma_s & -1/2-\tilde{\sigma}_x/\sigma_s & 0\\ -1/2-\tilde{\sigma}_y/\sigma_s & 1-\tilde{\sigma}_y/\sigma_s & 0\\ -2\tilde{\tau}_{xy}/\sigma_s & -2\tilde{\tau}_{xy}/\sigma_s & 3\end{bmatrix}\begin{Bmatrix}M_x^2\\ M_y^2\\ M_xM_y\end{Bmatrix} \tag{4.1}$$

where E is the Young's modulus, M_s is the saturation magnetization, λ_s is the saturation magnetostrictive coefficient, M_x and M_y are the magnetization in-plane values. The stresses are given by $\tilde{\sigma}_x = \sigma_x - \frac{1}{2}\sigma_y$, $\tilde{\sigma}_y = \sigma_y - \frac{1}{2}\sigma_x$ and $\tilde{\tau}_{xy} = \frac{3}{2}\tau_{xy}$. The relationship between H and M is given by:

$$\begin{Bmatrix}H_x\\ H_y\end{Bmatrix}=\frac{1}{kM}f^{-1}\left(\frac{M}{M_s}\right)\begin{bmatrix}1 & 0\\ 0 & 1\end{bmatrix}-\frac{\lambda_s}{\mu_0 M_s^2}\begin{bmatrix}2\tilde{\sigma}_x-\left(I_\sigma^2-3II_\sigma\right)/\sigma_s & 2\tilde{\tau}_{xy}\\ 2\tilde{\tau}_{xy} & 2\tilde{\sigma}_y-\left(I_\sigma^2-3II_\sigma\right)/\sigma_s\end{bmatrix}\begin{Bmatrix}M_x\\ M_y\end{Bmatrix} \tag{4.2}$$

where $k=3\chi_m/M_s$ (χ_m is the magnetic susceptibility), and f is a nonlinear scalar function which can be approximated using various expressions, such as the hyperbolic function $f(x)=\tanh(x)$ or the Langevin function $f(x)=\coth(x)-1/x$. In Eq. (4.2), $I_\sigma^2 - 3II_\sigma = \sigma_x^2 + \sigma_y^2 - \sigma_x\sigma_y + 3\tau_{xy}^2$, where I_σ and I_σ are the first and second stress invariants respectively. σ_s represents the axial pre-stress value.

To input a B-H plot, it must be in the form of H(B,σ), which requires a conversion of the model output of B(H,σ) to H(B,σ). A similar matrix conversion should be done for the λ(H,σ) matrix to obtain a λ(B,σ) matrix. There are several ways for COMSOL Multiphysics 4.4 to read the material data. These methods include the use of a table, MATLAB function, or text file. In this

work, a table was used for purposes of determining λ(B,σ) and H(B,σ). An example interpolation file is shown below.

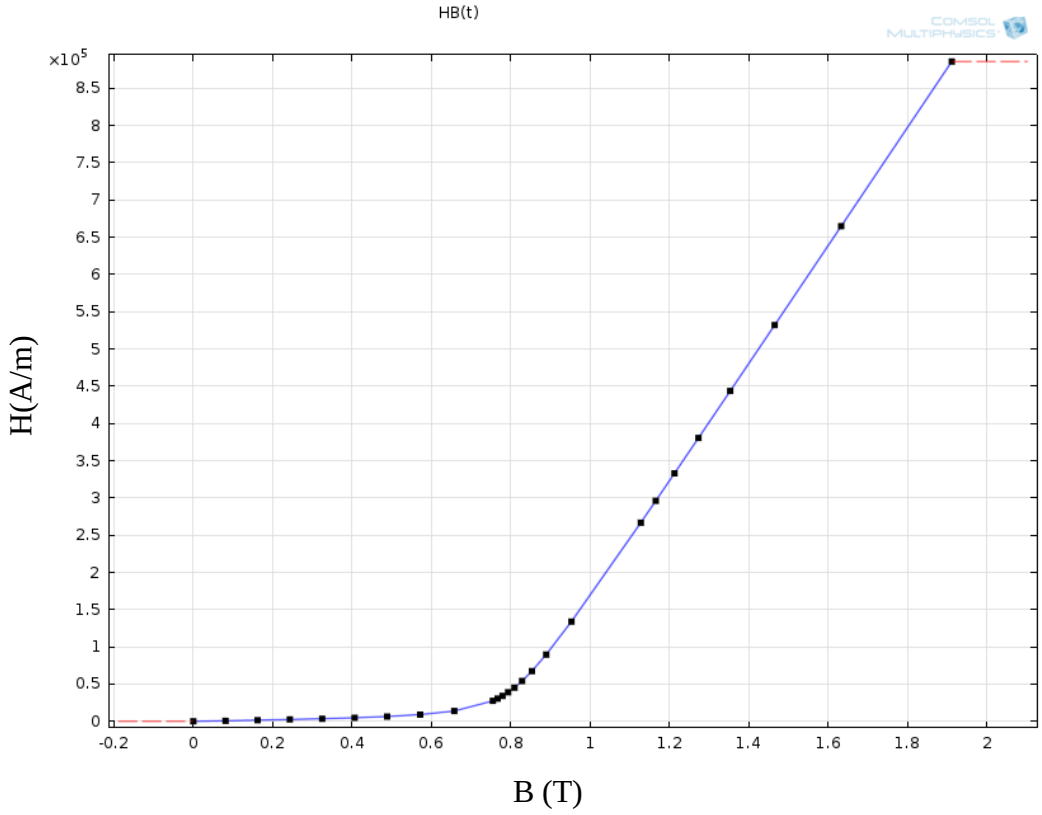

Fig. 4.2: Interpolation data for T-D

4.3 MICROSTRUCTURE GENERATOR TOOL

The generation of T-D particles manually as ellipses in the geometry is time consuming and is inefficient for realistically modeling the composite T-D particles that are embedded in the epoxy. Another method was developed to generate the T-D particles. With the Synthetic Microstructure Generator Tool and the LiveLink for MATLAB, more complicated geometry was created to represent the T-D particles and imported into COMSOL.

Synthetic Microstructure Generator tool has been developed to examine the influence of particle aspect ratio, area fraction, and orientation on representative length scales in two-phase microstructures [37]. This tool also includes the ability to generate particles with various distributions of

particle sizes and orientations. This MATLAB GUI script can be used to generate synthetic two-phase microstructures with elliptical particles in a voxelated image [37]. In this model, Synthetic Microstructure Generator Tool has been used to generate the image which represents the T-D particles since this tool has the ability to generate particles with different distributions, aspect ratios, orientations, and area fractions.

The first step is to enter values for volume fraction of particles and the image size (a_0 and b_0 define the major and the minor axis of the ellipses). The image size is the dimensions of the binary image, i.e., 2048 = 2048 x 2048 image. The resolution of the image and the particle size can be checked before proceeding to the next step. Given the particle size, the program will compute the number of particles that will fit within the image. The above steps are shown in Figs. 4.3 to 4.

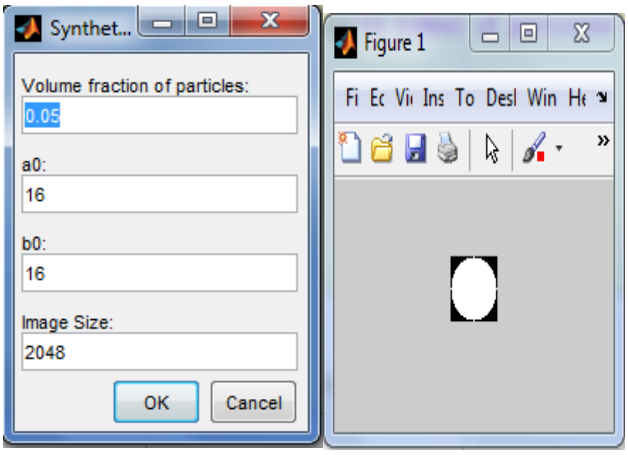

Fig 4.3: Default particle size in Synthetic Microstructure Generator Tool.

The next default step is to choose the lognormal size distribution for the particles and to enter the lognormal distribution parameters such as mean, sigma, and the increments parameter which indicates the number of bins for the lognormal distribution (as shown in Fig. 4.4). This will enable the program to randomly generate a list of particle sizes that best approximates the analytical form of the lognormal distribution and plots its representation.

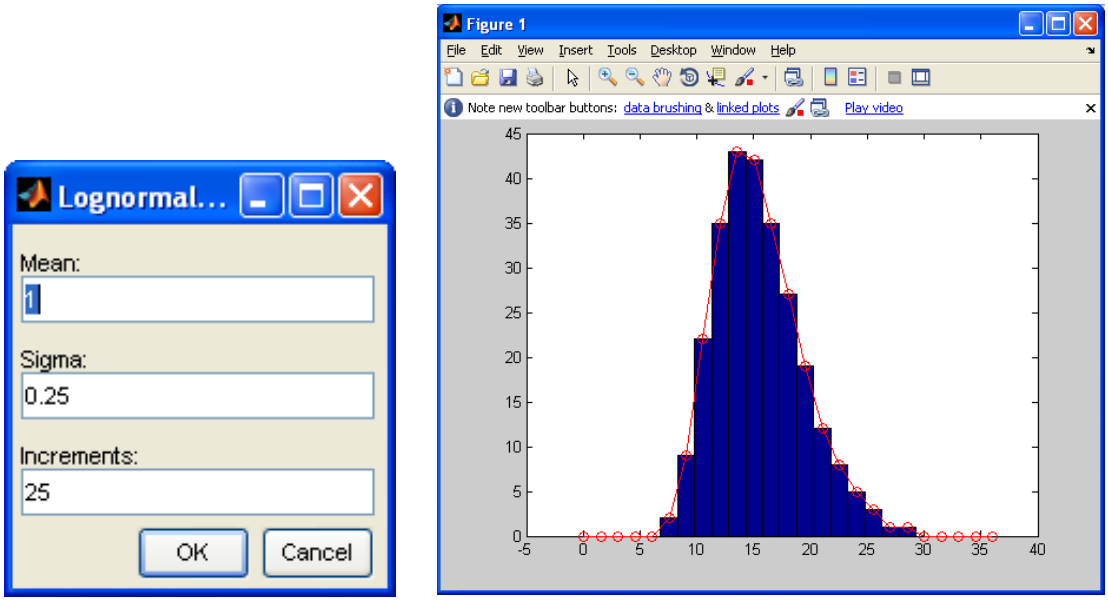

Fig 4.4: Lognormal size distribution for the particles

The other important feature for this program is the ability to choose the particles orientation distribution. There are three options that determine how the particles should be oriented: Aligned, random, and normal distribution. Aligned option is for the fully aligned case where we can select the orientation angle for the ellipses. Random is for perfectly random oriented particles, and the normal distribution allows the user to input the mean and the standard deviation (sigma) parameters for a normal distribution about an orientation angle.

The final step is to choose the filename and the location for saving the generated image. After the program finishes execution a microstructure will be generated according to these inputs. Two images will be displayed once the program is done; the first image displays the microstructure while the second image displays a close-up image showing the size and the orientation of the particles (see Fig. 4.5).

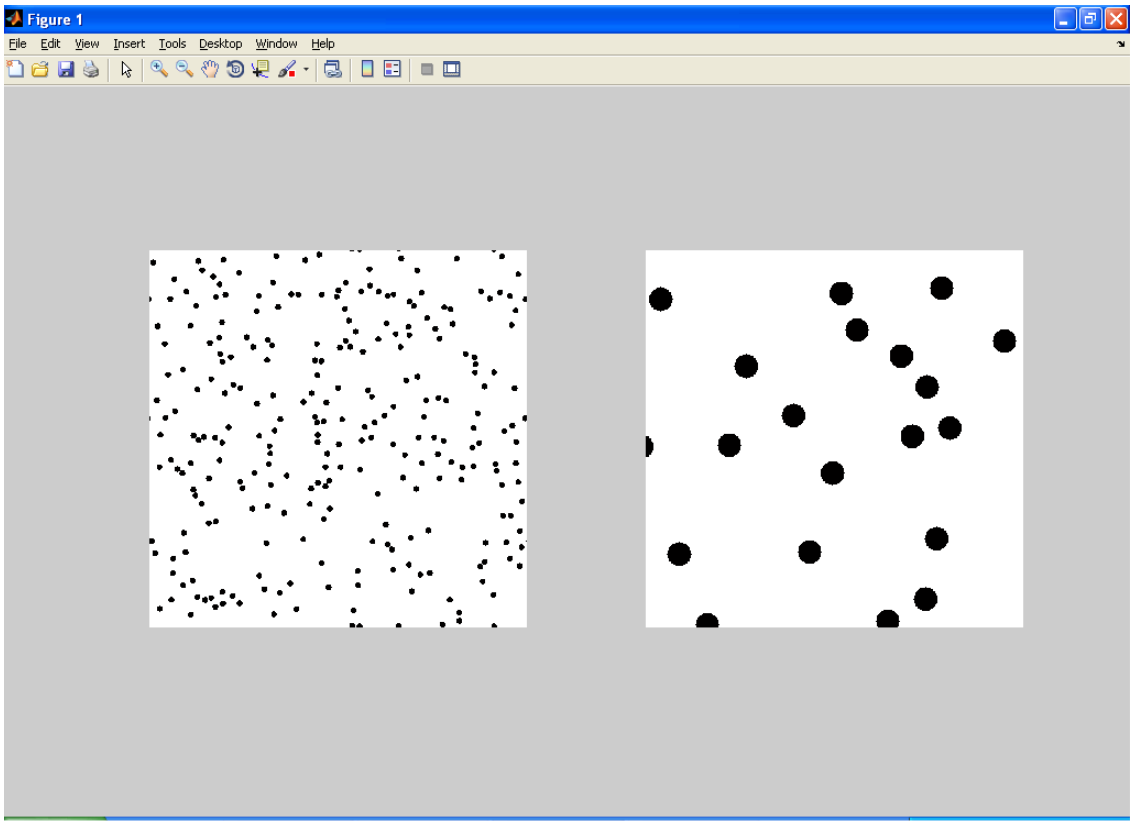

Fig 4.5: Final image displays the microstructure and a close-up image showing the size and the orientation of the particles.

In order to generate images with microstructures that is similar to the T-D particles, the default values in the Synthetic Microstructure Generator tool has to be adjusted. The volume fraction of the particles has been set to 0.05, a_0 has been set to 16, and b_0 has been set to 10. The size of resulting image is 2048 and the number of generated particles is 426. Fig. 4.6 shows the new generated image along with the distribution of T-D particles. Several other images have been created with larger particles size and different orientations as shown in Fig. 4.7.

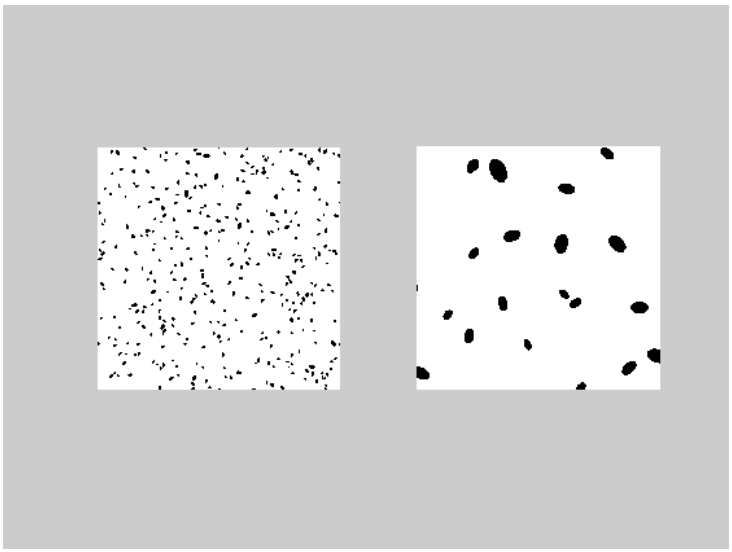

Fig.4.6: Image displays the microstructure that is similar to T-D particles.

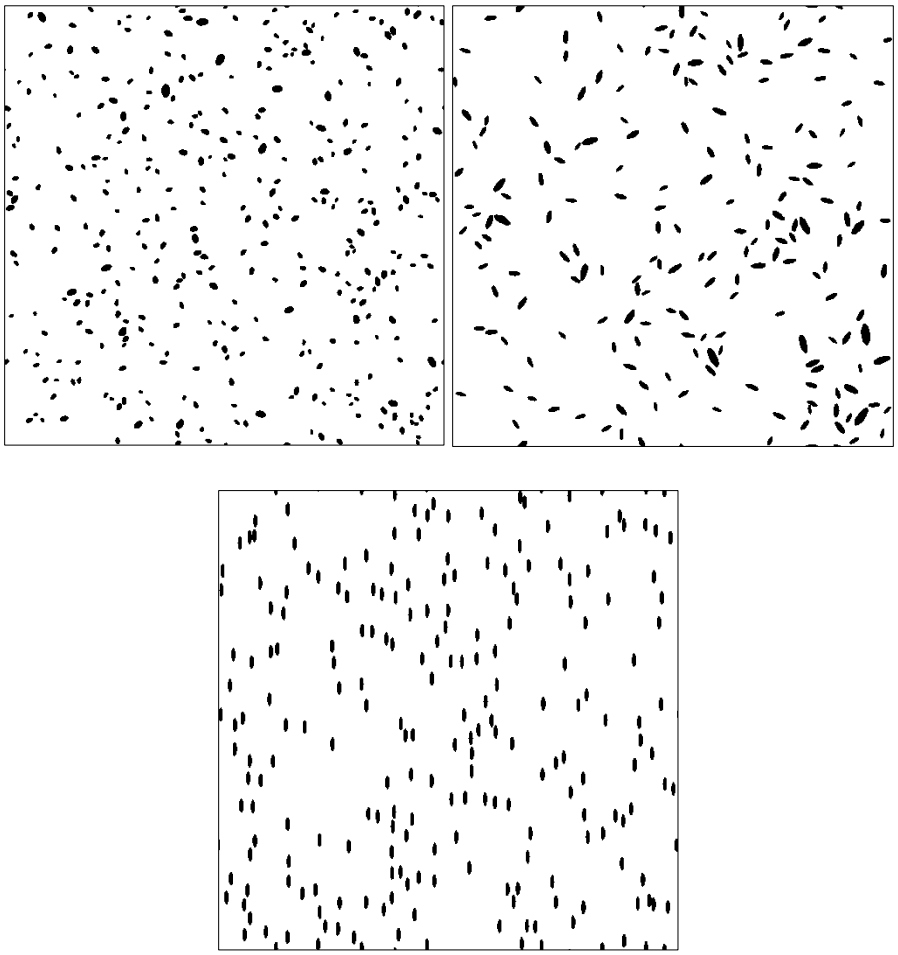

Fig. 4.7: Generated images with different particle sizes and different orientations.

4.4 CREATING GEOMETRY FROM IMAGE DATA

The function mphimage2geom has been used to create geometry from the image data which was generated using the Synthetic Microstructure Generator tool (see Fig. 4.8). The image data format can be *M*-by-*N* array for a gray scale image or *M*-by-*N*-by-3 array for a true color image. With the function 'mphimage2geom' provided in Matlab LiveLink it's possible to convert a grey scale image into geometry. A COMSOL model can be generated with this function, and then physics can be assigned to the geometry in the COMSOL model. LiveLink *for* MATLAB uses the client-server mode to connect COMSOL Multiphysics and MATLAB. When starting COMSOL with MATLAB, two processes are started— a COMSOL server and the MATLAB desktop. LiveLink *for* MATLAB connects COMSOL Multiphysics to the MATLAB scripting environment. Using this functionality we can build models using the LiveLink interface. We can also use the function mphgeom: mphgeom(model) to display the geometry in a MATLAB figure. The function mphsave can be used to save the model object linked to the MATLAB object model and its calling format is: mphsave (model,'filename'). If the filename is provided without a path, the file is saved relative to the local MATLAB path. The file extension determines the format to use (*.mph, *.m, or *.java).

A model for the geometry based on the T-D composite from the microstructure generation tool is enclosed by a rectangular air domain as shown in Fig. 4.9. Similar to the first model that was generated manually, two boundaries of the air domain are magnetically insulated to ensure that flux does not diverge out of the modeling domain. The other two boundaries of the of the air domain are assigned to be the sources of the magnetic field. The geometry consists of a single square which is 1200mm×1200mm to represent the epoxy while the ellipses in the square represent the T-D particles, the size of the ellipses are varying since they were generated randomly using the microstructure generation tool. The volume fraction of the particles has been set to 0.05. The

rectangle in the geometry model represents the air domain enclosing the composite. The material properties used in this model for T-D and epoxy are similar to the one that used in the previous model as shown in Tables 4.1 and 4.2.

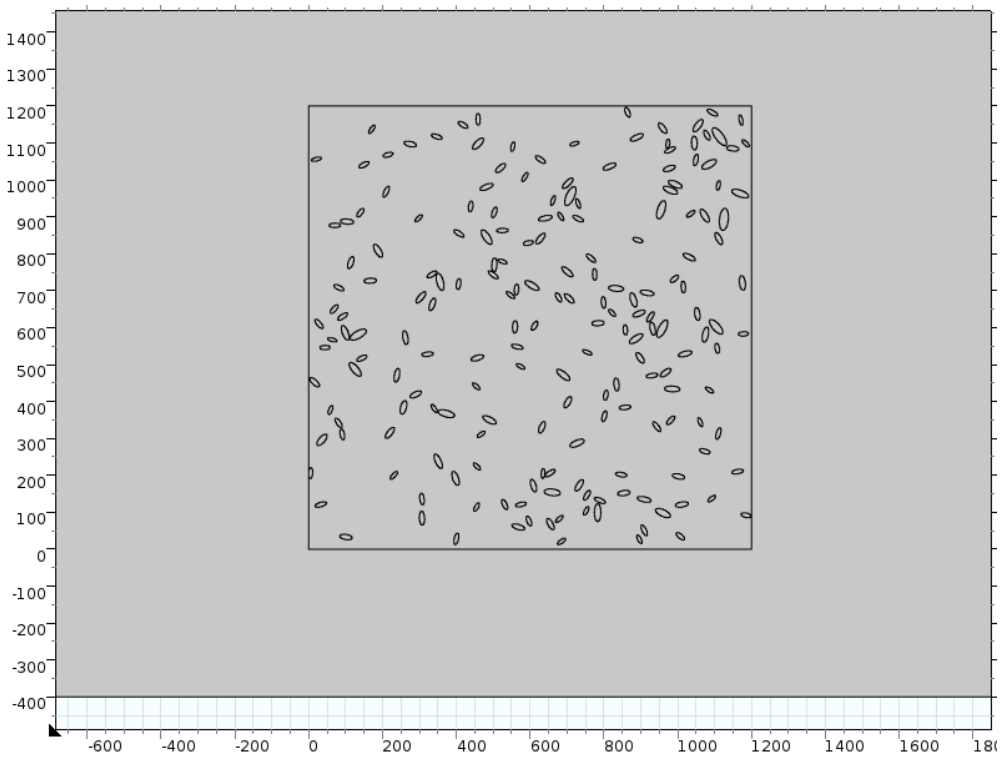

Fig. 4.8: Geometry generated with the function mphimage2geom.

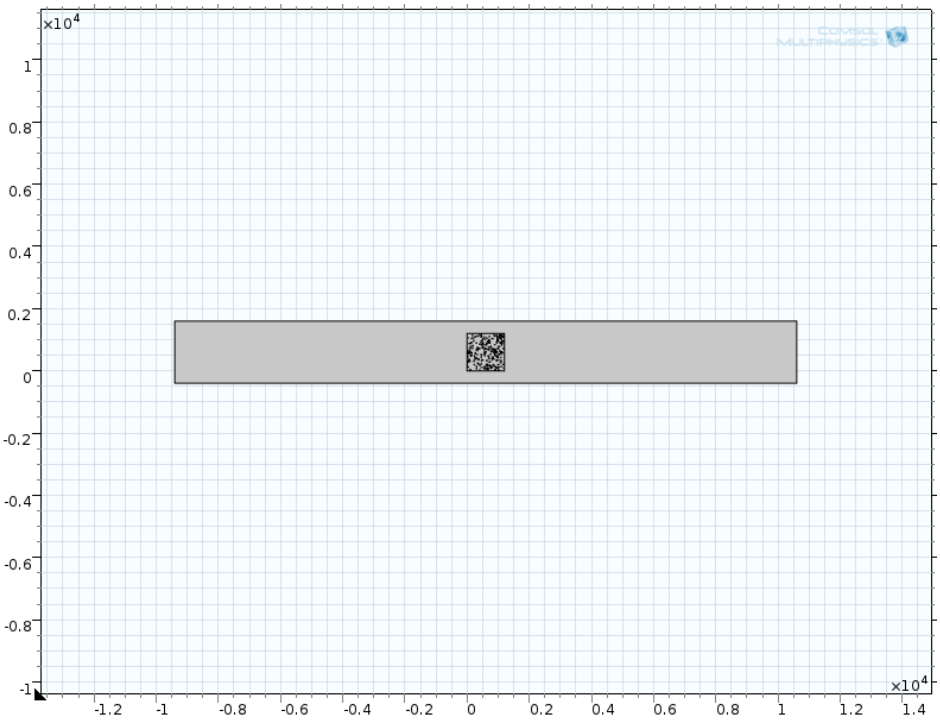

Fig.4.9: Geometry of the composite T-D with the air domain represented by the rectangle.

Using the function mphimage2geom, another image has been used to depict the geometry for the T-D composite. The image is shown below in Fig 4.10 while the generated geometry is shown in Fig. 4.11.

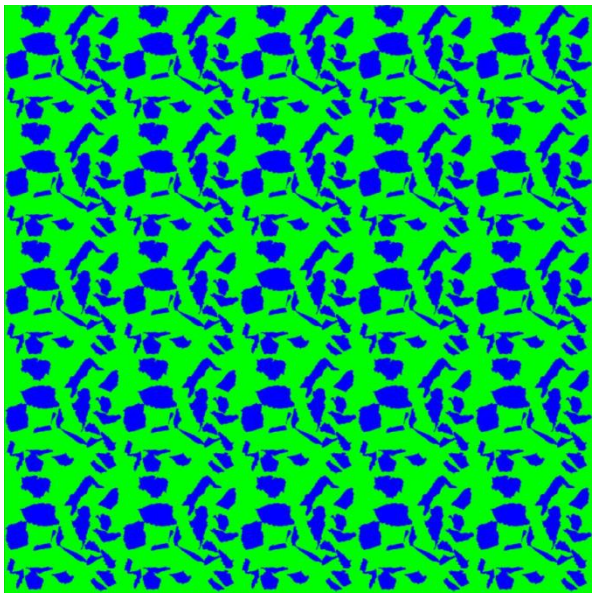

Fig. 4.10: Image depicts the real distribution and shape of T-D particles in composite block.

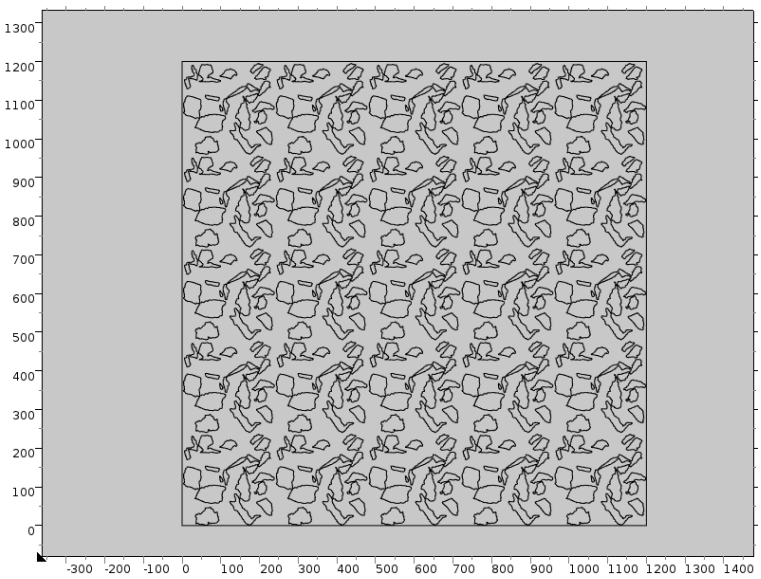

Fig. 4.11: Geometry generated using the function mphimage2geom from the image in Fig.4.10.

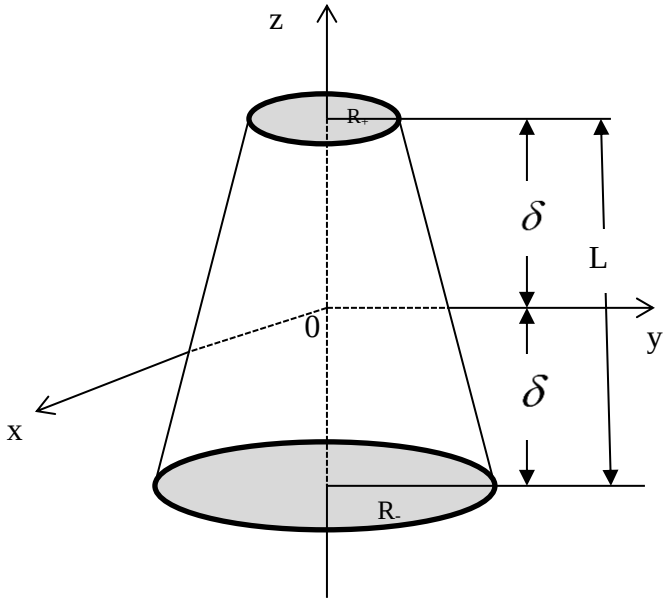

Fig. 4.12: Geometry of the cone-shaped transducer.

To predict the performance of the cone-shaped transducer, we have modeled its strain and magnetic field distribution with COMSOL. In the geometry setting for the cone model, the length

L of the cone was set to 37mm, the same length as the actual cone sensor that we prototyped in the laboratory (see Fig. 4.12). In COMSOL, the origin of the coordinates locates at the center of the object. Hence, $\delta = 18.5$ mm is the half height of the cone. The upper radius is R_+ = 2 mm and the lower radius is R_- = 5 mm. In Fig. 4.12, we do not show the middle narrow rectangle region that represents the channel filled with epoxy for the embedment of an FBG inside the sensor. The material properties for the cone are the same as those listed in Table 4.1 for the monolithic T-D while the material properties for the channel are the same as those listed in Table 4.2. Exploiting the cylindrical symmetry of the cone geometry, we have performed 2D simulations with COMSOL since the problem can be solved easily with less execution time under reduced dimension.

4.5 MESHING

A benefit of the finite element method is the ability to discretize the problem into several parts. This allows for a more computationally efficient solution for problems with complicated geometry and interactions among various physical properties. This section analyzes how an understanding of meshing properties is fundamental to obtaining an accurate and computationally efficient solution. A mesh is a discretization of geometry into pieces known as elements. Each element contains nodes which help to define the relationships of the key variables of the problem. In a 2D model, the most traditionally used elements are triangular and rectangular. Most triangular elements contain either three, six or seven nodes.

There are several options to choose from when creating a mesh. The predefined free mesh parameters vary from extremely fine to extremely coarse. For this study a coarse mesh was implemented. Clearly, there is a tradeoff between computational efficiency and model accuracy, as a finer mesh normally requires more memory and computational time, but generally gives a more accurate solution. Multiphysics model can be created, solved, and analyzed in COMSOL

Script. This includes creating the geometry, meshing, assigning loads and boundary conditions, solving the model, post-processing, etc.

4.6 CALCULATING NONLINEAR MAGNETOSTRICTION

The magnetostriction component along any direction can be calculated as a nonlinear function of the magnetization using Eq. 4.3 [38].

$$\lambda_i = \frac{3}{2}\lambda_s\left(\alpha_i^2 - \frac{1}{3}\right) = \frac{3}{2}\lambda_s\left(\left(\frac{M_i}{M_s}\right)^2 - \frac{1}{3}\right) \tag{4.3}$$

Magnetostriction (λ_i) along the direction i depends on the magnetostriction constant (λ_s) and the magnetization direction cosine (α_i). The direction cosine is the ratio of magnetization along the required direction (M_i) and the saturation magnetization (M_s) of the material. Those values have been specified for this model under the global parameters as shown in the figure below.

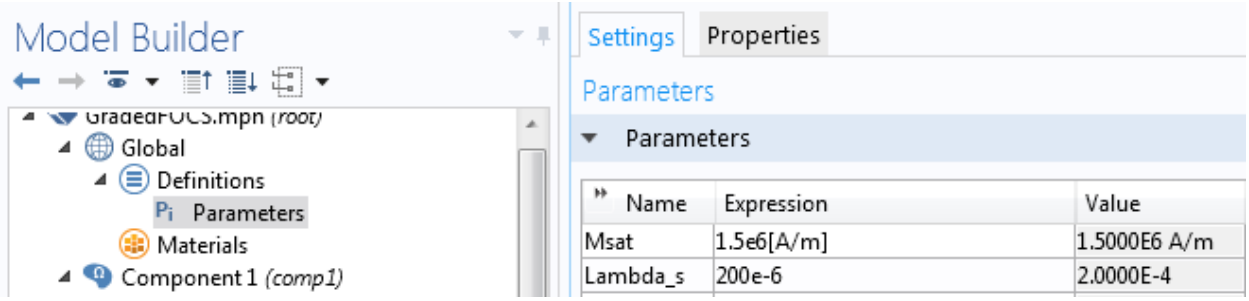

Fig 4.13: Magnetostriction and magnetization saturation values of the model.

4.7 RESULTS

Fig.4.14 shows the magnetic flux concentration in the magnetostrictive T-D ellipsoid particles for the first model where the T-D particles have been generated manually in COMSOL. Fig. 4.15 shows a surface plot of the norm of the magnetic flux density in the second model. The mesh size that has been used in these models is fine. It can be seen from Fig. 4.14 that the magnetic flux density is concentrated in the ellipses which represents the T-D particles. As the number of

particles increases in each block the magnetic flux density increases in that particular block especially the last block which has more T-D particles. Fig 4.15 shows that the magnetic flux density represented by the arrows is also concentrated in the T-D particles. Due to the random orientation of T-D particles the arrows that represent the T-D particles are also oriented randomly in the model.

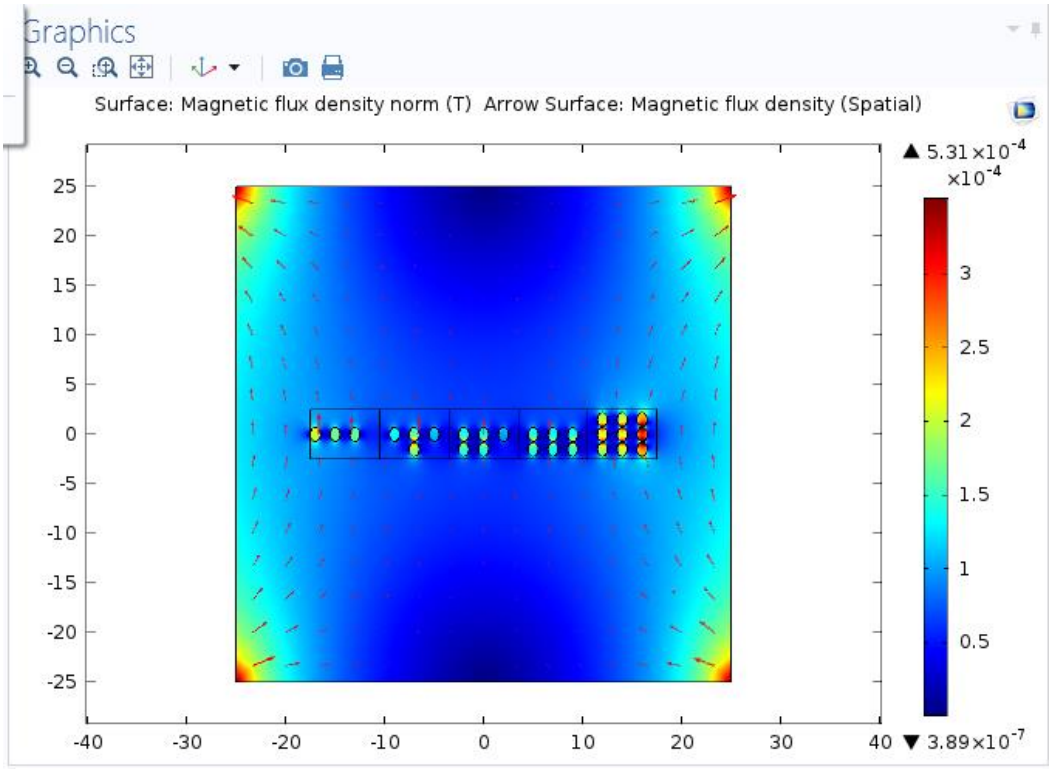

Fig. 4.14: Surface plot of the norm of the magnetic flux density and a normalized arrow plot of its x and y-components showing the closed flux path in the first model.

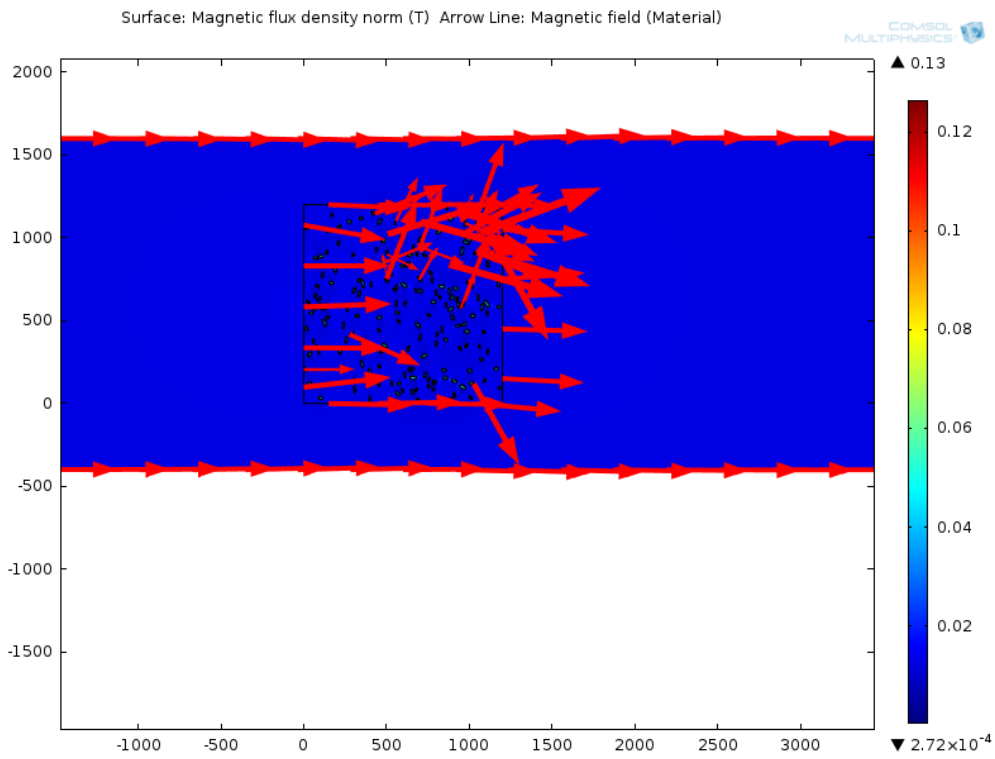

Fig. 4.15: Surface plot of the norm of the magnetic flux density and a normalized arrow plot of its x and y-components showing the closed flux path in the second model.

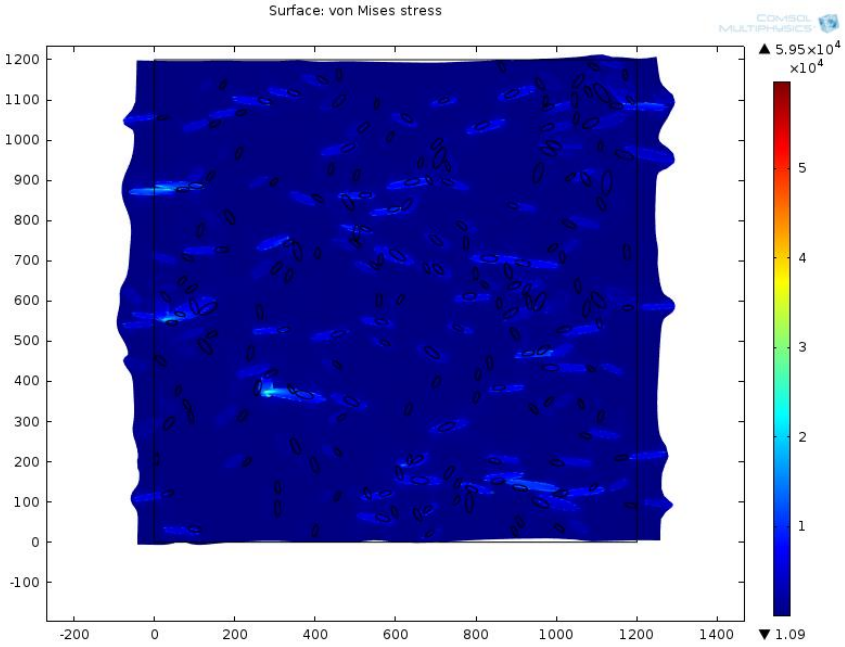

Fig. 4.16: Surface plot of stress and deformation of the T-D particles for the second model.

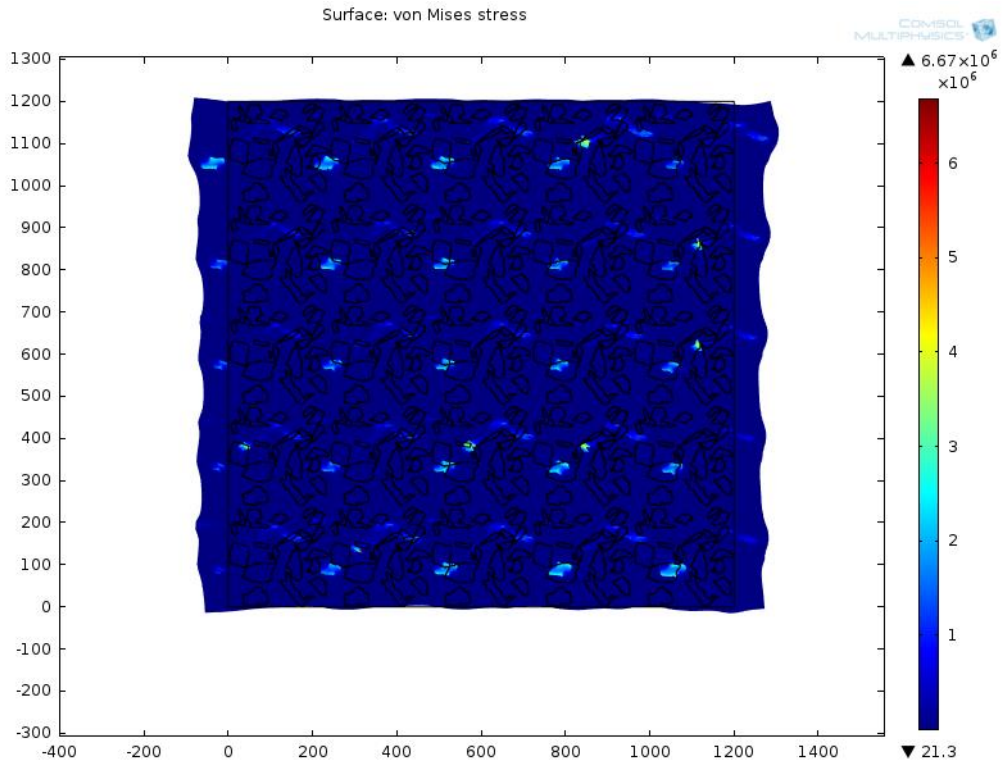

Fig. 4.17: Surface plot of stress and the deformation of the T-D particles for the third model.

Fig 4.16 shows the surface plot of stress and deformation of the T-D particles for the second model while Fig 4.17 shows the surface plot of stress and the deformation of the T-D particles for the third model. In both figures we can notice the deformation that occurred to the T-D particles due to the applied field. The T-D particles have expanded in direction of the applied field. A parametric sweep study has been done to the second model where the magnetic field range was specified and the strain on a certain point on the T-D composite was measured. The resulted saturation strain was in order of 1000με (a very high for composite T-D) since the saturation magnetization for monolithic T-D has been used in this study. This may contribute to the high saturation in the strain values for the composite T-D model at high magnetic intensity (on the order of 10^6 kA/m). If we scale the saturation magnetization based on the volume fraction of T-D, the saturation in the strain values will be on the order of 100's με.

Figs. 4.18 and 4.19 illustrate the typical results from simulations for the cone-shaped transducer under uniform magnetic field intensity of 10 kA/m. Particularly, Fig. 4.18 shows the disturbance in the magnetic field with a surface plot of the magnitude of the magnetic flux density and a normalized arrow plot of its x and y-components after the introduction of the cone to the external field. It clearly shows that the closed flux path in the cone sensor model satisfies the magnetic boundary conditions. We notice that the magnetic field near the upper end reaches the peak value rapidly while the magnetic field near lower end increases to the peak gradually. This tendency can be interpreted as the cone focusing the magnetic flux. More precisely, this is a manifestation of the demagnetization. With the upper end having higher longitudinal to transverse aspect ratio, this end experiences less demagnetization than the lower end. The surface plot of strain along the Z axis of the cone sensor model in Fig. 4.19 indicates the strain distribution tracking that of the magnetic field since the applied magnetic field is rather low and there is no saturation.

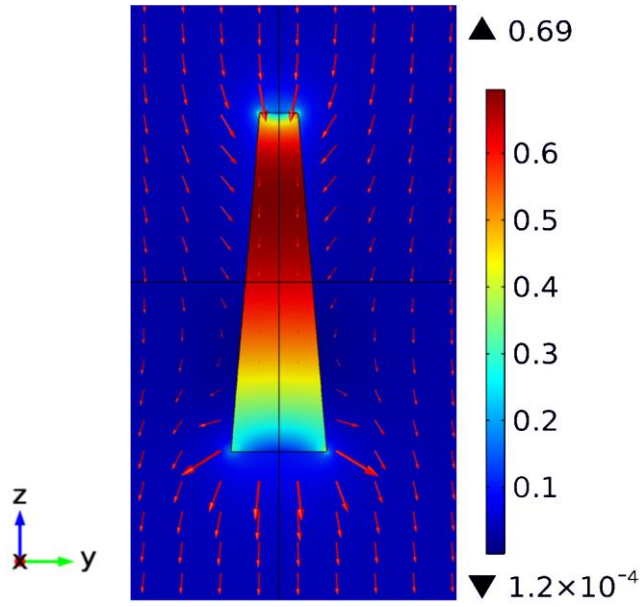

Fig. 4.18: Surface plot of the magnitude of the magnetic flux density and a normalized arrow plot of its x and y-components showing the closed flux path in the cone sensor model.

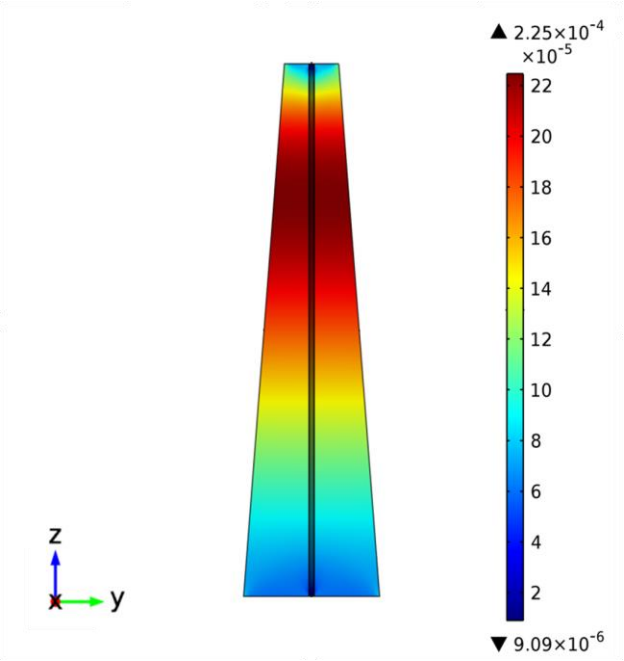

Fig. 4.19: Surface plot of strain along Z axis of the cone sensor model, H = 10 [kA/m].

4.8 ANALYTICAL EXPRESSION FOR THE MAGNETIC FIELD INSIDE THE CONE

In this Section, we develop an analytical expression for the axial magnetic field in the cone-shaped transducer in order to verify the correctness of the COMSOL simulations. The formulation of the analysis is based on the demagnetization from the magnetization $\vec{M}$ inside the cone sensor induced by the external field $\vec{H}$ [39]. The analysis is similar to Ref. 39 but has been updated for the cone shape instead of a cylindrical one. We follow the geometry defined in Fig. 4.12 where radius R_+ is the upper radius, R_- is the lower radius, the height of the cone is L along the z-axis, which is the longitudinal axis of the cylinder. Since the origin $z = 0$ is at the middle of the cone, the upper end of the cone is at $z = +\delta$ and the lower end lies at $z = -\delta$. For later calculation, we need to definite the slanted angle between the side wall of the cone and z-axis $\alpha = \tan^{-1}\left(\frac{R_- - R_+}{L}\right)$ and the radius of the side wall on the x-y plane $R_0 = R_+ + \delta \tan\alpha$.

In the case of current-free region (i.e. $\vec{J} = 0$), the magnetic field can be found as follows:

$$\vec{H} = -\vec{\nabla}\phi \,. \tag{4.4}$$

where ϕ is the magnetic field scalar potential.

Similar to the electric field and potential being expressed in terms of charges, we can define magnetization surface charge density $\rho_{ms} = \vec{M} \cdot \hat{n}$ where $\hat{n}$ is the outward pointing normal on the surface of the cone and magnetization volume charge density $\rho_{mv} = -\nabla \cdot \vec{M}$ relates to the divergence inside the cone. Hence, we can calculate with

$$\phi = \frac{1}{4\pi}\oint_{s'} \frac{\rho_{ms}}{R} ds' + \frac{1}{4\pi}\int_{v'} \frac{\rho_{mv}}{R} dv' \,. \tag{4.5}$$

where $R = |\vec{r} - \vec{r}'|$ is the distance between the source point with position vector $\vec{r}' = \rho'\hat{\rho}' + z'\hat{z}$ and the observation point .with position vector $\vec{r} = \rho\hat{\rho} + z\,\hat{z}$. Notice that ρ is the radial direction for the observation point, ρ' is the radial direction for the source point and $\hat{z}$ is the unit vector for the z-axis. We observe from the COMSOL simulation that there is very little transverse magnetic field component and the external field is uniform. As the first order approximation, we assume the induced magnetization to be uniform with magnitude M_z and along the longitudinal direction, i.e. $\vec{M} = M_z\hat{z}$. Owing to uniform magnetization, $\rho_{mv} = 0$ but there are surface charge densities. Particularly, $\rho_{ms} = \pm M_z$ at $z = \pm\delta$, respectively. This means that the top end has a positive charge while the bottom end has a negative charge. In addition, ρ_{ms} on the side wall cannot be neglected and is a function of z-axis which is different from a cylinder. The magnetic field $\vec{H}$ inside the cone is generated by an effective magnetic charge density that can be written as:

$$\begin{aligned} \phi &= \frac{M_z}{2}\Phi(z) \\ &= \frac{M_z}{2}\left(2z + \sqrt{R_+^2 + (z-\delta)^2} - \sqrt{R_+^2 + (z-\delta)^2}\right) \end{aligned} \tag{4.6}$$

$$+\frac{M_z}{2}\sin\alpha\left[\mathrm{R}_0\cos^2\alpha\left(1-\frac{z}{R_0}\tan\alpha\right)\ln\left|\frac{z'}{R_0}\sec\alpha-\sin\alpha\right.\right.$$

$$\left.\left.-\frac{z}{R_0}\cos\alpha+\Delta(\mathrm{z},\mathrm{z}')\right|-R_o\Delta(z,z')\sin\alpha\right]\Bigg|_{z'=-\delta}^{z'=\delta}$$

where $\Delta(\mathrm{z},\mathrm{z}')=\sqrt{\left(1-\frac{\tan\alpha}{R_0}z'\right)^2+\frac{1}{R_0^2}(z-z')^2}$. The second line of Eq. (4.6) contains potentials of the top and bottom of the cone while the third and fourth lines of Eq. (4.6) account for the potential of the side. Then H_z can be found as a function of z with:

$$H_z=-\frac{d\phi}{dz}=-\frac{M_z}{2}\frac{d\Phi(z)}{dz}. \tag{4.7}$$

Since the internal field $H_{int}\approx H_z$ should the sum of the external field H_{ext} and the field from magnetization which opposes the external field and $M_z\approx\chi_m H_z$ where χ_m is the magnetic susceptibility, we can estimate

$$H_{int}=\frac{H_{ext}}{1+\frac{\chi m}{2}\frac{d\Phi(z)}{z}}. \tag{4.8}$$

In the cone-shaped transducer case, $\delta=1.85cm, R_{+}=2mm, R_{-}=5mm$. Fig. 4.20 below shows the behavior of the demagnetization magnetic field H_{int} along the z-axis of the cone for $H_{ext}=\frac{0.01}{\mu_o}$. and $\chi_m=9$. We find that the curve in Fig. 4.20 matches COMSOL very well.

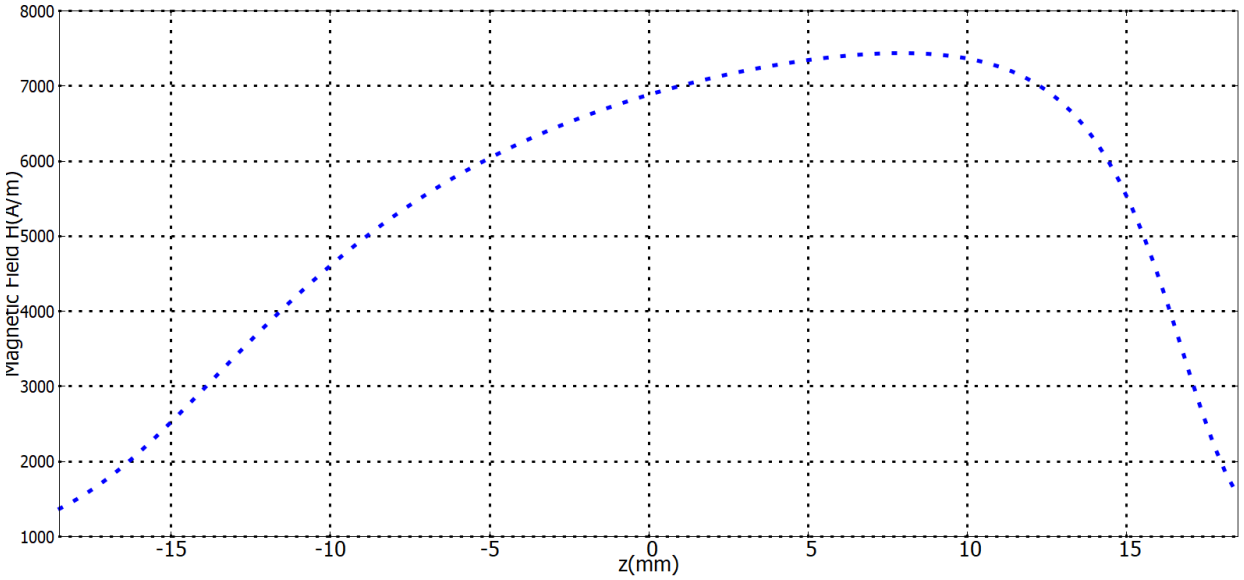

Fig. 4.20: Magnetic field intensity along z-axis of a cone under uniform external field.

5. EXPERIMENT COMPONENTS AND PROCEDURES

5.1 EXPERIMENT COMPONENTS

Optical components and instruments as well as electric power supplies, and many other magnetic components have been used to set up experiments for the characterization and fabrication of prototypes. The fiber type used in the experiments is SMF-28, single- mode with 900μm or 250μm jackets. An Exalos SLED with around 1547nm central wavelength, 16mW output power, and 7.9THz bandwidth was used as the source of the broadband optical signal (shown in Fig. 5.1).

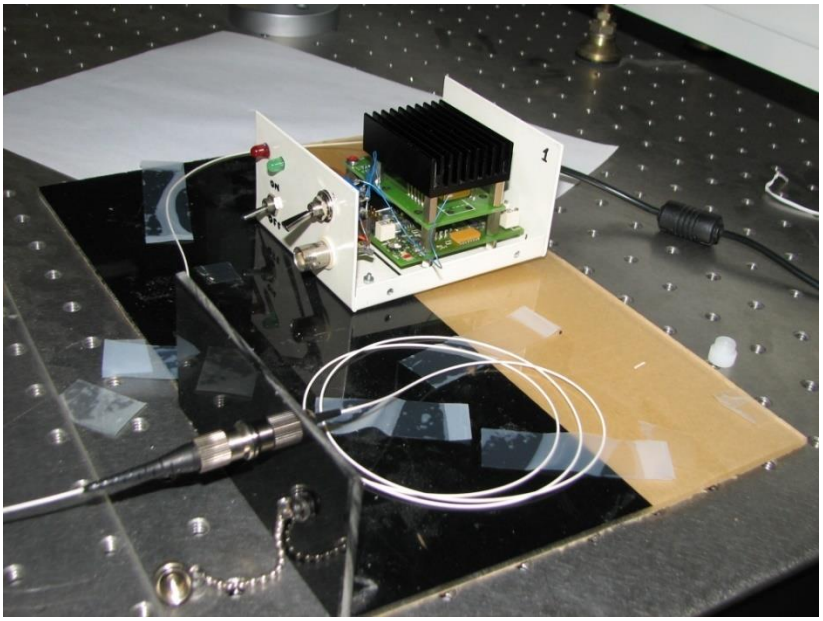

Fig. 5.1: Superluminous LED (SLED)

Optical circulator has been used in the experiment setup. The optical circulator is a special fiber-optic component used to control the flow of optical signals so that signals travel in one direction among its 3 ports (see Fig. 5.2). In addition, an optical isolator (shown in Fig. 5.3) has been used in the setup to prevent light from being reflected back to the source. The broadband optical signal from the SLED passes through the optical isolator and enters port 1 of the optical circulator. Then the light signal exits from port 2 of the circulator and propagates through the fiber

Bragg grating FBG. Port 3 of the circulator routes the reflected signal from the FBG that enters port 2 to an optical spectrum analyzer, a wavelength meter, or a power meter.

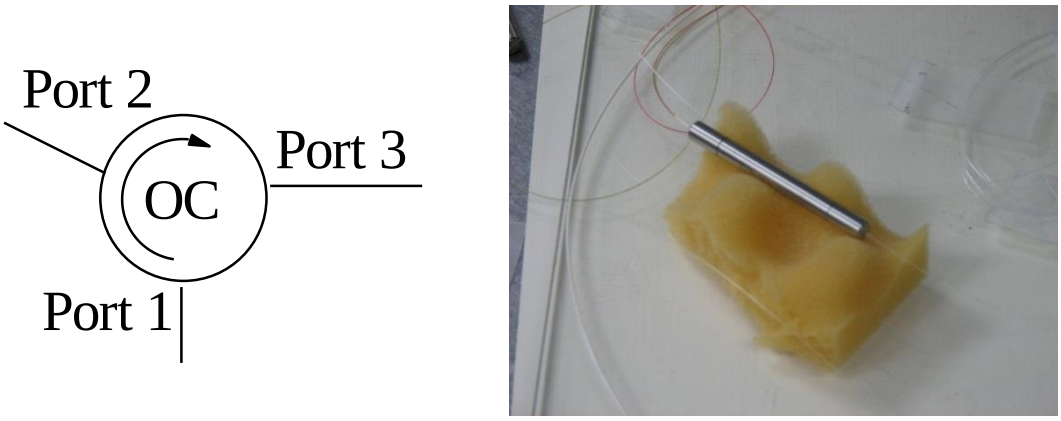

Fig. 5.2: Optical circulator**.**

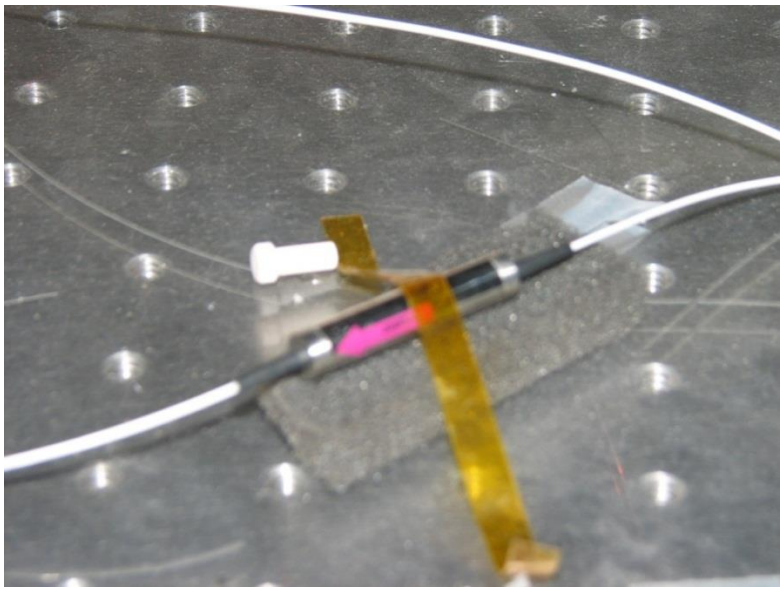

Fig. 5.3: Optical isolator

Two magnetic field sources have been used for testing. In previous trials, a magnetic coil of about 1050 turns of 14 AWG conductors has been used as the source of the magnetic field (shown in Fig. 5.4). The coil has a resistance of about 6 Ω and a measured inductance of about

$\pi/40 \sim 0.0785$ H. For measurement purposes, the sensor is placed in the middle of the coil's air core.

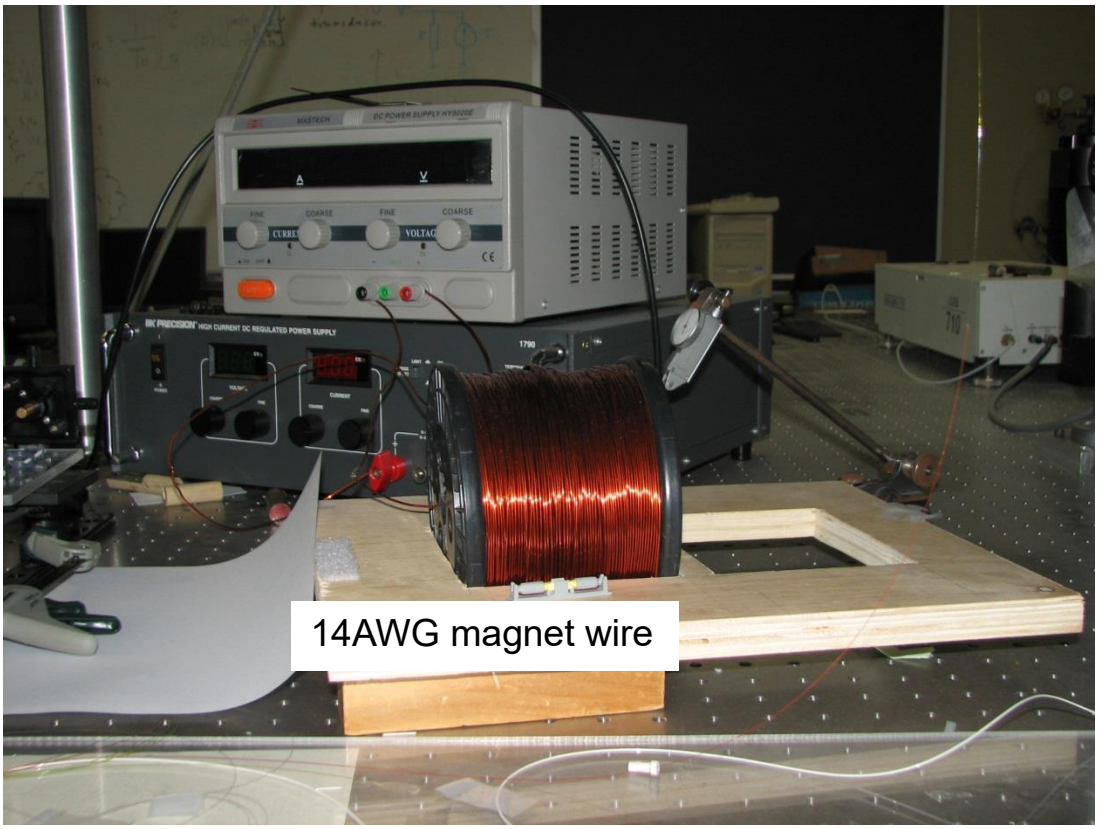

Fig. 5.4: Magnetic coil for magnetic field source.

Later, a laboratory electromagnet has been acquired and was used to generate the magnetic field for the testing of the cone-shaped sensor (see Fig. 5.5). A magnetometer/Gauss-meter has been used in measuring and monitoring the magnetic field level. OSA is not practical for measurement in the field and is mainly used for sensor characterization in the laboratory. For sensing in the field, we can use a photodiode. The photodiode circuit converts the optical power into electrical signals that can be easily processed and measured as the output voltage; e.g. an oscilloscope was used in our experiments. The setups of the previous and the current setups for the DC and AC magnetic field testing are shown in Fig. 5.4 and Fig. 5.5, respectively.

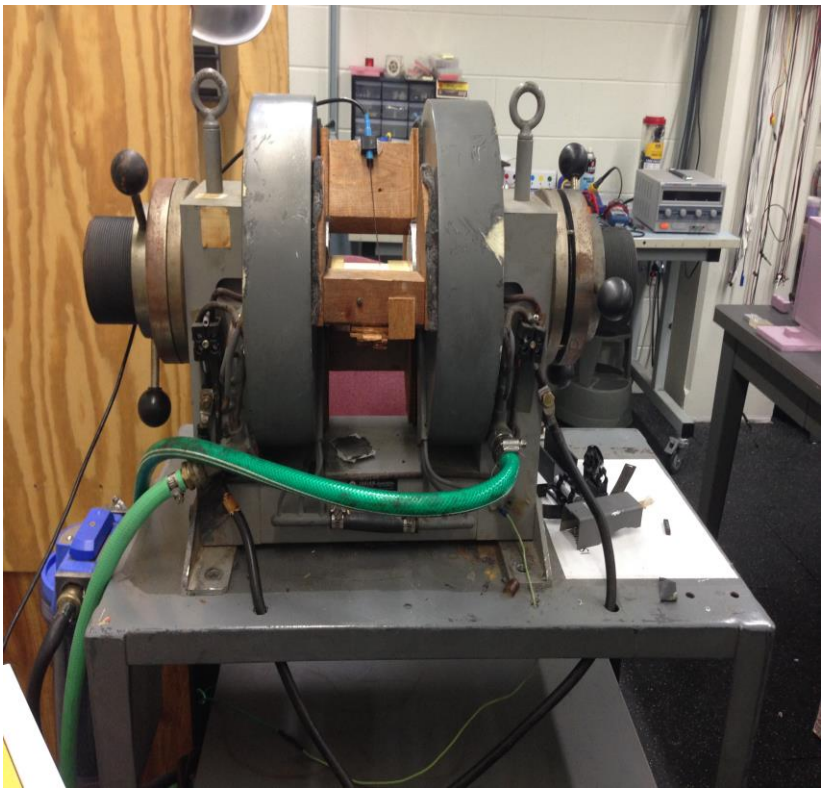

Fig. 5.5: Laboratory electromagnet for magnetic field source.

For the AC magnetic field generation, the electromagnet was driven by a 7224 AE Techron power amplifier that boosts the power of the AC signal from a function generator to sufficient level for high field level.

5.2 EXPERIMENTAL SETUP

Using the components described in the previous sections, a single channel optical link has been built and connected to the current sensor as shown in Figs. 5.6 and 5.7.

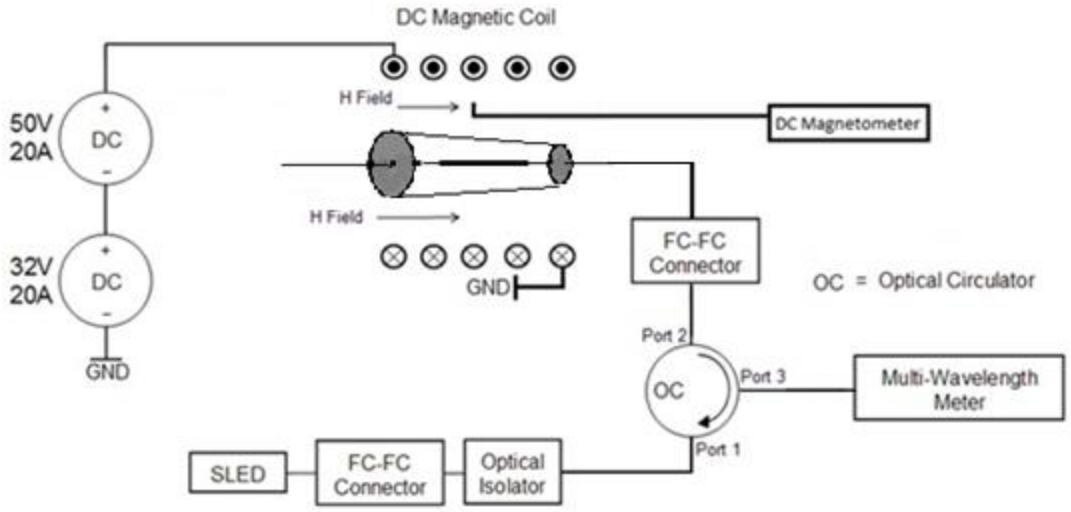

Fig. 5.6: Experimental setup used for DC magnetic field experiments in the laboratory.

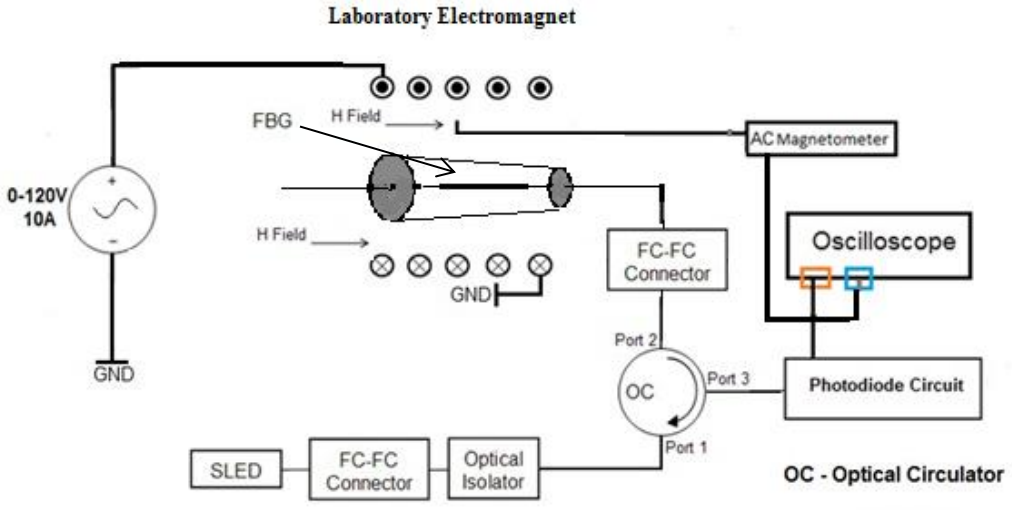

Fig. 5.7: Experimental setup used for AC magnetic field experiments in the laboratory.

Various optical circuit components including the sensor, i.e. the FBG, in the circuit are connected together by fiber splicing. The components required for this procedure include: fiber optic stripper, optical fiber cleaver, and non-abrasive wipes, and fusion splicer. The quality of

splicing is very important for our experiment setup since it affects the losses and reflections in the optical circuit.

The first step is to prepare the fiber to be spliced by stripping about 1 to 1.5 cm of the outer fiber jacket. Then the stripped portion of the fiber is cleaned with a non-abrasive wipe after wetting it with one to two drops of methanol. With the cleaver, smooth surfaces perpendicular to the fiber axis are created a both ends of the fibers that are going to be spliced by following the instructions on the cleaver. The fiber ends need to be cleaned again with the non-abrasive wipe and methanol to remove any unwanted particles. The two ends are now ready to be spliced; each end is inserted into the fusion splicer until it is centered in the view window of the splicer. To keep the fiber ends secured, the lock nuts on the slice should be closed. The splice can be verified through the view window of the splicer where the estimated loss is displayed.

5.3 MEASUREMENT PROCEDURES

5.3.1 MAGNETIC FEILD MEASUREMENTS

Accurate measurement of the magnetic field is required in order to correctly characterize the FOCS performance. In our sensor prototype, we used T-D composite to perform as the transducer which converts the magnetic energy from the current source into the mechanical energy as the composite expands in the presence of the magnetic field. An AC/DC-selectable magnetometer has been used to measure the magnetic field surrounding the sensor. The magnetometer has an adjustable range, and measure the magnetic field in Gauss. When testing with the magnetometer in the laboratory setup for the graded sensor, the probe of the magnetometer is placed inside the coils and attached to the holder using one piece of tape. In the setup for the cone-shaped sensor, the probe is positioned so that the probe head lies directly above the sensor inside the electromagnet. The probe was attached to the electromagnet with hot glue. When testing

of the graded FOCS at various levels of current, the values for the magnetic field were read directly from the magnetometer while the output spectrum data were collected by the WLM controlled by a labVIEW program. The range on the magnetometer needs to be adjusted to match the generated field by the coil. For further data processing and analysis, the measurements of the magnetometer in Gauss have been converted to kA/m by simply dividing them with a factor of 4π since the magnetometer probe is placed in air for all relevant measurements. In order to compare AC field measurements to DC ones, the root mean square (rms) value recorded from the magnetometer is multiplied by a conversion factor (determined by the shape of the waveform) for obtaining the peak field value.

5.3.2 SPECTRAL POWER MEASUREMENTS

Spectral power measurement is very important to determine the input-output transfer characteristics of the various prototypes of FOCS. With the old experimental set up, the FBG reflection spectrum from the sensor was acquired with the WLM. On the WLM screen the complete spectrum, peak powers, and peak power wavelengths can be displayed. During sensor construction, it is useful to view the spectrum shape, peak power and wavelength as a quick check of the correct procedure of sensor prototyping. For example, when embedding the FBG into the T-D transducer, a visual check of these parameters helps determining the next step. For further processing of the spectrums of the sensors, the WLM is connected to a computer via GPIB-USB interface. With LabVIEW program, the spectrum can be viewed and stored for further processing and the calculation of the total spectrum power.

The LabVIEW program that has been used to collect and record data from the WLM has been created by Aaron Muller [6]. This program has a user-selectable measurement range which allows the user to specify the wavelength range of interest. An acceptable range for our

experiments is 1548nm-1554 nm. For collection of FOCS data at various levels of current/magnetic field, the magnetic field value is read from the magnetometer while the LabVIEW program downloads data from the WLM at discrete levels of current.

In the new experiment setup we used the OSA instead of the WLM to monitor the spectrum. With the software for the OSA, the spectrum of the FBG can be recorded and saved through a straightforward and responsive GUI that controls the OSA while calculating various parameters, e.g. the total power, the peak wavelength and the full width at the half maximum (FWHM) spectral width.

5.3.3 DIRECT POWER MEASUREMENTS

In the laboratory, we record the output spectrum of the sensor and numerically integrate the output to obtain the total reflected power or we use the OSA to obtain the total reflected power. In field applications, this approach is slow and result in massive amount of data. In the actual implementation of this sensor, only the returned optical power will be used as the output. There are a few ways of measuring total power output in the lab. For DC magnetic field measurements, we used the OSA software to obtain the total power under each spectrum. For AC magnetic field measurements, the sensor output from port 3 of the optical circulator is routed to a simple photodiode circuit, shown in Fig. . In the photodiode circuit used in the experiments, V_B was supplied by a 9V battery and the photodiode had a responsivity $\mathcal{R}$ =0.94 A/W at λ=1550 nm. We used various values of load resistances R_L (4.75kΩ, 32kΩ, and 52kΩ) to obtain a clear output signal from the photodiode, we used. The output voltage V_o of this circuit in response to the input optical power P_{OPT} is given by

$$V_o = P_{OPT} \times \mathcal{R} \times R_L \, . \tag{5.1}$$

For measuring V_o in response to a DC magnetic field, a multi-meter was used. In addition, we used the oscilloscope to record the amplitude, the frequency, and the shape of the output waveform for AC magnetic field measurements.

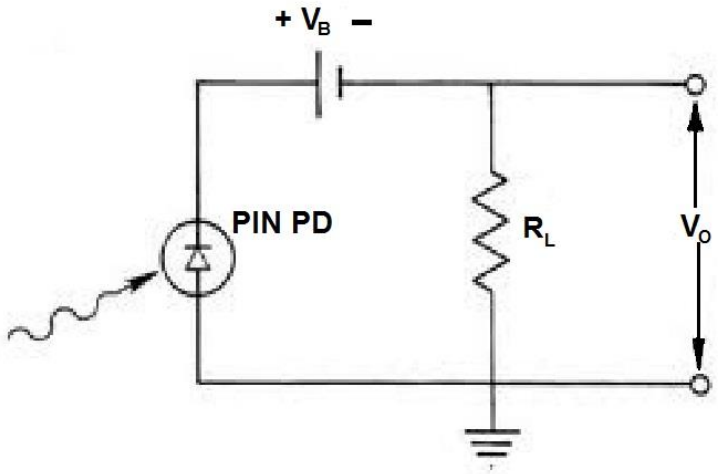

Fig. 5.8: PIN photodiode circuit used for power measurement.

5.3.4 TEMPERATURE MEASUREMENTS

For the investigation of thermal effect on the response of the FOCS, several experiments have been performed. A conventional oven with attached proportional integral (PI) controller has been used in the beginning. The sensor was placed in the middle of the oven. Special holder was fabricated with a 3D printer for fixing the sensor position inside the oven. In order to ensure that the heat will be distributed uniformly inside the oven, a fan was inserted inside the oven. The controller has a display to show the current temperature inside the oven and push buttons to increase or decrease the temperature. While increasing the temperature from room temperature to 50° C with an increment of 2° C degrees, the spectrum was recorded by the WLM or the OSA. This method has some shortcomings; the heating element in the oven was at the top of the oven and this was a direct heat source above the sensor. Besides, we had to leave the door of the oven open in order to get a stable temperature reading on the display of the PI controller.

To get more precise results and to be able to automate the process of the temperature adjustments and spectral data collection, we improved the setup and procedure for thermal measurement in several areas. We used a thermal chamber instead of the oven. The heating element inside the chamber was made of four light bulbs. Two fans have been installed inside the chamber to ensure that the heat will circulate uniformly; one has been installed in the back of the chamber while the other is in the top. To obtain accurate temperature measurements, we used a digital thermometer (Data Logger RTD Thermometer, SE-376) that has a measurement range of -100°C to 400°C with an accuracy of ±0.05% reading + 0.1ºC). Data from the built-in-memory on the digital thermometer was transferred to the PC through a USB cable under the control of the SE376 software. The time interval between each data to be recorded can be specified by setting the sampling rate. The resulting real time graph is effective for monitoring the temperature inside the

chamber (as shown in Fig 5.9). Since the temperature sensor is located at the end of the metal sheath of the sheath type temperature probe, the thermometer probe should be inserted horizontally through a hole inside the chamber and put very close to the cone-shaped sensor which lies on the floor of the chamber in order to obtain accurate temperature measurements.

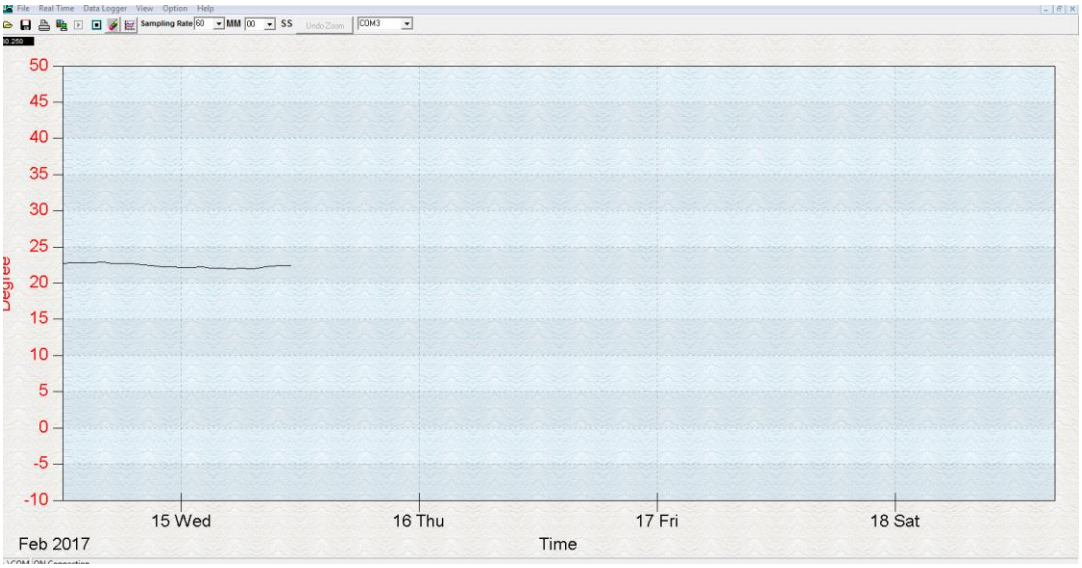

Fig. 5.9: Real time graph in the SE376.

In addition, we used a LM35AH temperature sensor to measure the temperature inside the chamber for the controller. The LM35 series are precision integrated-circuit temperature devices with an output voltage linearly proportional to the Centigrade temperature. The temperature sensor and the light bulbs are connected with National Instruments NI cDAQ-9174 and Arduino UNO to set and measure the temperature inside the chamber (as shown in Fig. 5.10). Both the RTD digital thermometer probe and the DAQ temperature sensor were placed very close to the sensor in order to monitor the temperature and to get more reliable data. We put a small barrier of insulating material between the sensor and the heating element to prevent direct heat from effecting our measurements.

It has been noticed that at temperature higher than 30° C it takes very long time to reach the next temperature set point. In addition, we have to wait for half an hour at each temperature set point before collecting the spectrum to ensure that the temperature equilibrium has been reached. Hence, the automation of data collection becomes. With MATLAB and CS-Script files, a program was developed, with the collaboration of Edward Lynch and Daniel Brandt, to control the OSA with the CS-Script named osascript.cs that synchronizes data collection from the OSA and thermal probe. For each data collection session, a folder is created to save the files with the temperature and the time stamp incorporated into their names. The program is set to save the spectrum for every degree over the range 22° C to 50° C. However the maximum temperature that we were able to achieve inside the thermal chamber was 39C. The results of the thermal testing are presented in chapter seven.

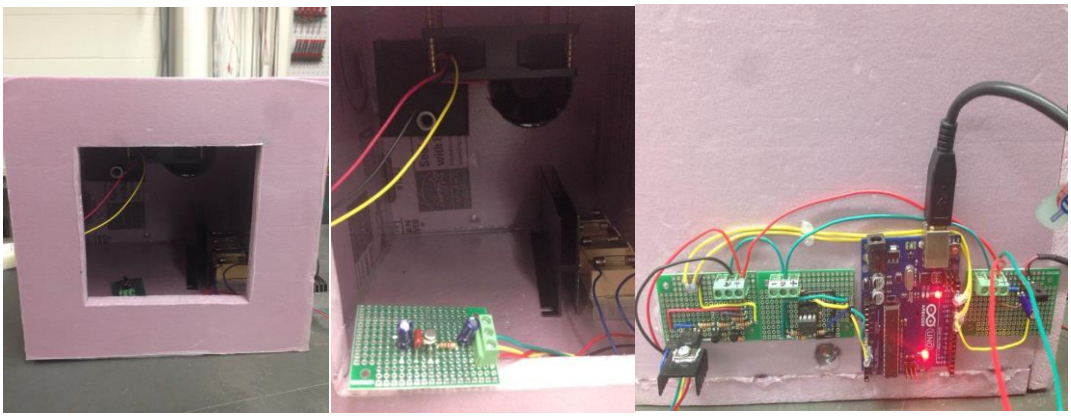

Fig. 5.10: Setup for temperature measurement.

6. SENSOR PROTOTYPES

6.1 CONE-SHAPED SENSOR CONSTRUCTION

All the sensors prototyped in our laboratory are based on embedding an FBG in a T-D composite which was prepared by mixing T-D particles with a polymer. The employed polymer is a kind of adhesive, which is normally in a liquid state. In order to fabricate the transducers in different shapes, we applied several methods. All the methods required mold manufacturing. For sensor prototypes with simple geometry, we used the EasyMold Silicone Putty with a Plexiglas template that was fabricated by cutting a piece of Plexiglas into the required shape and specified dimensions. The EasyMold Silicone Putty has 3 minutes of working time at 70° F. Cooler temperatures will result in slightly slower cure rates while higher temperatures will fasten the cure rates. Therefore, it is important to work quickly when making the molds. The template was cut and ready in the correct dimensions before the mold was prepared. First, the EasyMold Silicone Putty was quickly kneaded together in equal amounts by weight or volume of components A and B until swirl free uniform color was achieved. This process usually takes about 1 minute. Then roll the kneaded components into a ball and then flatten slightly. The next step is to press the object with the template in desired shape into putty to form the mold. Then the template was left in putty to cure for 25 minutes. Finally, the object was removed and the mold was ready to use. Some of the molds that have been constructed with this method are shown in Fig. 6.1. For accelerating the cure process with heat, the mold on the top of an aluminum foil was either placed in the center of an oven at least 6” from the heating elements or near a heat lamp.

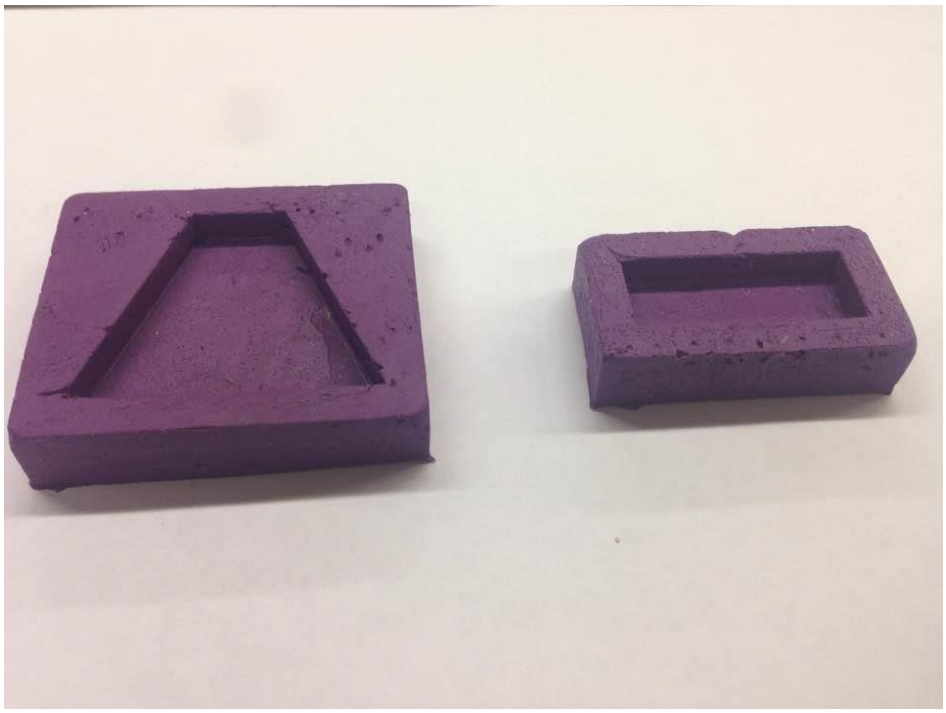

Fig. 6.1: Molds for simple shapes manufactured with EasyMold Silicon Putty

However, it was hard to cut the cone shape and construct a mold with the silicon putty method which was appropriate for simple shapes as shown in Fig 6.1. The cone shape was chosen since it has different cross sectional area along the z-axis which means that the number of T-D particles will be different across the length of the embedded FBG particles. Owing to the taper shape of the composite, the strain distribution varies with the magnitude of the magnetic field. In order to construct the cone-shaped sensor, a cone was created with a 3-D printer (as shown Fig. 6.2). Then two silicon compounds have been mixed and poured into a hollow cylinder which was also 3-D printed. In this process, we used Alumilite's High Strength 2 silicone mold making rubber since it is soft enough but is sufficiently rigid for multiple re-use while maintaining good alignment. In addition, High Strength 2 silicone has a low viscosity and is capable of replicating the exact detail of the original piece. It is a tin based silicone and cures under all different types of clay and substrate. Temperature and humidity may affect the cure speed of the rubber. There are two components: A side or component which is the base and B side which is the catalyst. To prepare

the mold with Alumilities's High Strength 2 silicon, the amount of material for the mold was first calculated. The mixing ratio of the High Strength series silicon rubber is 10:1 by weight. The two components were poured in a large container to give adequate room for the thorough mixing of the rubber. Moreover, the large container allows the rubber to expand /grow if degas/vacuum is necessary and prevents the mixture from over flowing into the vacuum chamber. Degassing the mixture may be required since air bubbles are introduced during mixing. The base and the catalyst were mixed thoroughly for about 2-3 minutes. Once the material was mixed thoroughly, it was poured slowly into the hollow cylinder to avoid air entrapment. The Silicon has a very high tear strength and ability to bond to other surfaces. Therefore, it is imperative to use the mold release to prevent the mold from adhering to the inside surface of the hollow cylinder. Then the cone-shaped template was immersed into the mixture and left to harden. The full cure schedule of the Silicon is seven days. Next the mold was extracted out of the hollow cylinder. Finally, the mold was ready to be used to fabricate the cone-shaped sensor as shown in Fig. 6.2.

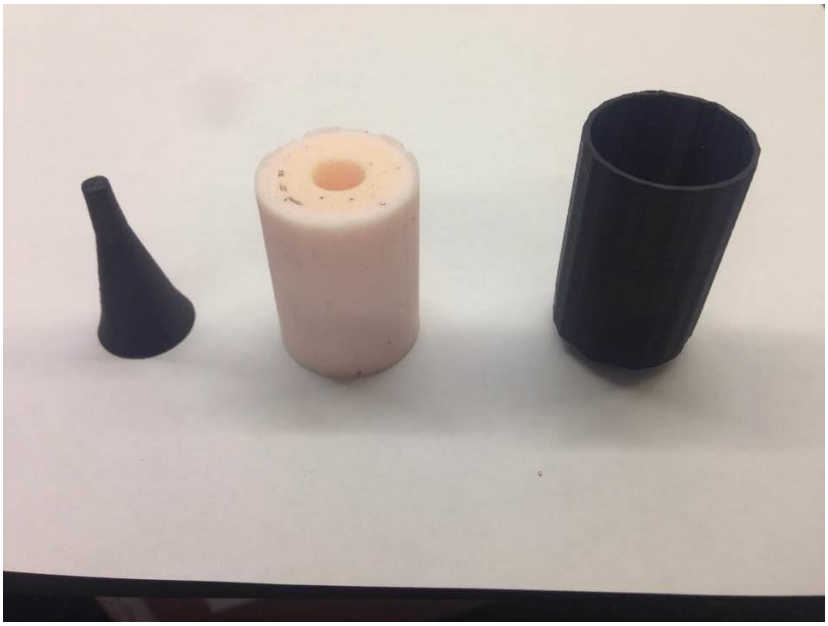

Fig. 6.2: Cone-shaped template and its mold produced with the first method.

The production of the transducer requires the manufacturing of the epoxy-bonded Terfenol-D particulates in sizes of 250–300 μm. The first stage of the manufacturing process is to prepare the epoxy by mixing the epoxy resin (part A) with the Super Sap 1000 hardener (Entropy Resins, Inc) in 2:1 ration by volume or 100:48 by weight. The mixing of the two parts must be performed thoroughly and slowly to reduce the air bubbles. The epoxy mixture was put in a vacuum chamber to remove the trapped air bubbles. This process was done very quickly before the epoxy started to harden since the work time of this epoxy is 25 minutes. The T-D particles weighted using a probable milligram scale. For accurate reading, the scale was placed on a horizontal flat surface. Predetermined quantities of T-D particles and epoxy (4.512g epoxy: 1.263g T-D) were homogenously mixed. After proper stirring; the mixture was placed inside the vacuum chamber. Since the resin had a relatively low viscosity, the process allowed to get rid of unnecessary air trapped inside the mixture during the stirring process. Then the mixture was poured into the previously prepared cone shaped mold.

Before pouring the mix into the mold, a PL013 (0.33mm) acoustic/electric high carbon steel guitar string (D'Addario & Company, Inc) was used to create the hole in the transducer. The guitar wire was fixed from one end and a weight was attached to the other end to keep it straight and centered inside the mold. Now the T-D composite mixture was then poured inside the mold with the embedded guitar wire that prepared a channel for the introduction of an FBG inside the transducer. Week later (the recommended full cure time for the Super Sap epoxy), the cone-shaped transducer was ready to be extracted out of the mold. The next step for prototyping the sensor is to embed the FBG inside the cone shaped composite. This process will be discussed in section 6.3.

A second method has been used to construct the cone-shaped transducer. In this method, a cone, hollow cylinder, two lids for the cylinder, and a base were manufactured in the machine shop

with aluminum (the schematics are shown in appendix B). In the middle of the cylinder lids, there are two small Plexiglas pieces with a central hole for the traverse of the guitar string through the mold (shown in Fig 6.3). Plexiglas has been used in fabricating those two small pieces since a thin drill bit for the size of the small hole was brittle and failed to penetrate a thick piece of aluminum without breaking. The mold making process for the second method is similar to the first one. With the cone placed inside the hollow cylinder, the mold making silicon rubber was poured around the cone. After the silicon hardened, the cone was taken out of the hollow cylinder. Then the guitar wire was inserted into one end of the hollow cylinder where the mold was attached to the lid with a hole for the wire. Now the T-D and the epoxy mix can be poured inside the mold. The other side of the guitar wire can go through the hole in the second lid. After one week, the cone-shaped transducer is ready to be released from the mold as shown in Fig 6.4.

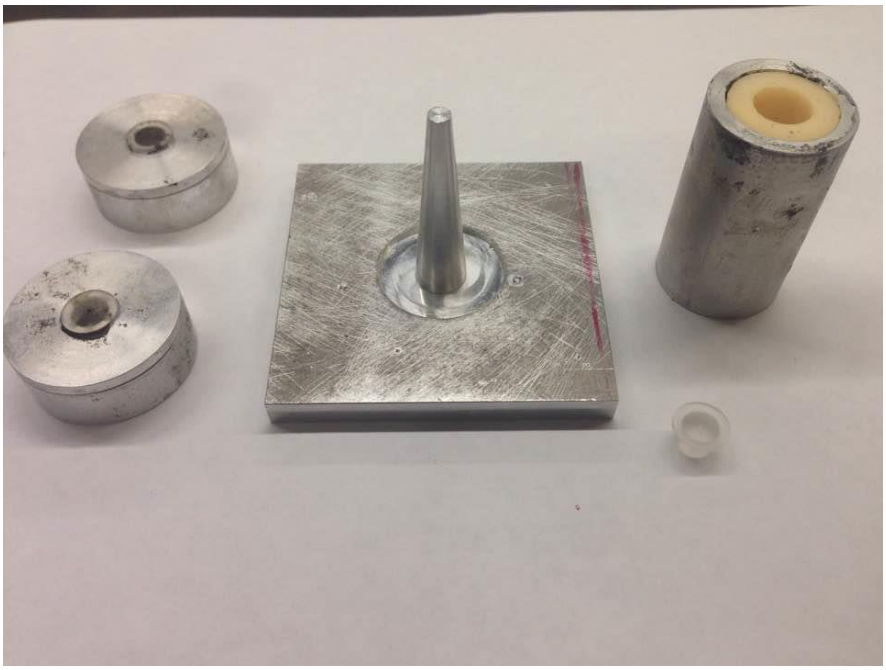

Fig. 6.3: Cone shape mold and associated pieces for the second method.

Fig. 6.4: Cone shaped Transducer

6.2 GRADED SESNOR CONSTRUCION

To manufacture the graded sensor, the FBG was embedded in a T-D composite with a graded particle size distribution. T-D particles ranging from 20 to 300 microns were used. The FOCS was prototyped by fabricating layers with different volume fractions of T-D. Particles of MONEL-400 were blended with T-D particles to compensate for thermal expansion and ensure more uniform distribution of T-D. MONEL-400 was grinded with Dremel wheels to MONEL-400 powders. A rectangular piece with five squares has been 3-D printed. Then the mold material (Alumilite's High Strength 2 silicone mold making rubber) was mixed and poured inside. One week later, the mold was ready. The resulting sensor is shown in Fig. 6.5.

Fig 6.5: Graded FOCS

6.3 FBG EMBEDDING PROCEDURES

An appropriate method for embedding a FBG onto a transducer was of the utmost importance in the sensor fabrication. If the FBG is not properly embedded onto the transducer, the current sensor will not perform as expected and the gathered data will not suitably describe the practical events of interest. Before the FBG is embedded, it is spliced to the optical fiber link. This was done so that the output characteristics of the FBG which include the peak wavelength, spectral width, the spectral power density at the peak wavelength, the total power, and the overall spectral shape can be actively monitored with the OSA during the embedding procedure. Being able to see the real time output is crucial for deciding how to proceed in the embedding process. In the following descriptions, the portion of the grating fiber spliced to the link is identified as the link side, while the unconnected side is referred to as the open side. The FBG with an overall length L=3cm,

linewidth (FWHM) = 0.066nm, and unchirped Bragg wavelength $\lambda_B = 1550nm$ was used to fabricate the FOCS.

Embedding the FBG in both cone-shaped and graded sensors requires the same basic set of equipment, including the optical rails, rail carriers, posts, fiber optic positioners, fiber holders, and linear stage. The fiber containing the grating is held taut with fiber optic positioners while the output characteristics of the FBG were monitored with the OSA. Then the open side of the link was inserted inside the hole in the cone-shaped transducer. The transducer rests on a thin acrylate polymer platform which itself rests on a manual linear stage. The fiber optic positioners are mounted on standard posts and optical rail carriers which have been slid onto a mini optical rail secured to an optical table. The fiber optic positioners are generally kept about 20-25cm apart. This apparatus is shown in Fig 6.6.

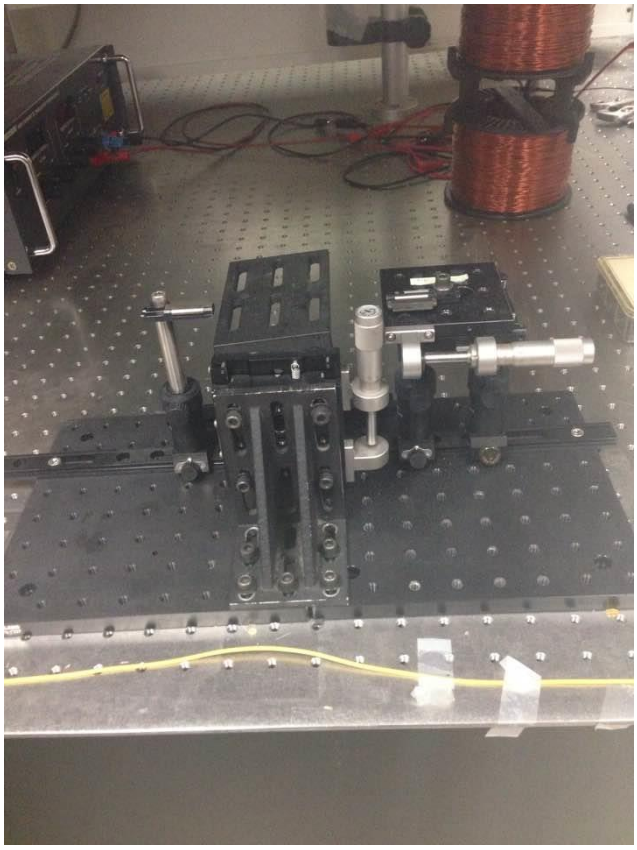

Fig. 6.6: The FBG Embedding setup.

To attach the FBG inside the transducer, a small hole was drilled on the narrow end of the cone composite. This hole functioned as a port for the injection of the epoxy which will attach the FBG to the transducer. Several types of epoxy were experimented on such as AA-BOND F113 resin (Atom Adhesives. Inc) and F120 two-part fiber optic connecter epoxy (Thorlabs, Inc). The goal was to use a low viscosity epoxy that flowed from the hole at one end of the cone to the other end. In addition, a fast curing epoxy was used for rapid bonding of the FBG to the transducer. The F120 epoxy satisfied the requirement of fast cures and low shrinkage for quick high performance fiber optic connections. At room temperature, the FBG will be attached to the transducer within 30 minutes; however, fully cured bonds require up to 48 hours. Unfortunately, the work time of this epoxy is five minutes which was too short for the epoxy to pass through the channel. LOCTITE ECCOBOND F112 BIPAX or known as TRA-BOND F112 (Henkel Electronic Materials, LLC.)

was used instead for its longer work time of 40 minutes. After mixing the two parts of the epoxy, a syringe was used to inject the epoxy through the injection port. The cured color of the epoxy is blue which enabled us to determine if the epoxy has filled the whole channel inside the transducer and surrounded the FBG all the way to the other end. The complete cone-shaped sensor with the FBG embedded inside is shown in Fig. 6.7. The success in attaching the FBG to the transducer is indicated by the maintenance of reflection spectrum throughout the whole embedding process. The sensor is now ready for experiments. A holder with a cone shape in middle was 3-D printed to hold the cone-shaped sensor in the middle of the electromagnet for testing.

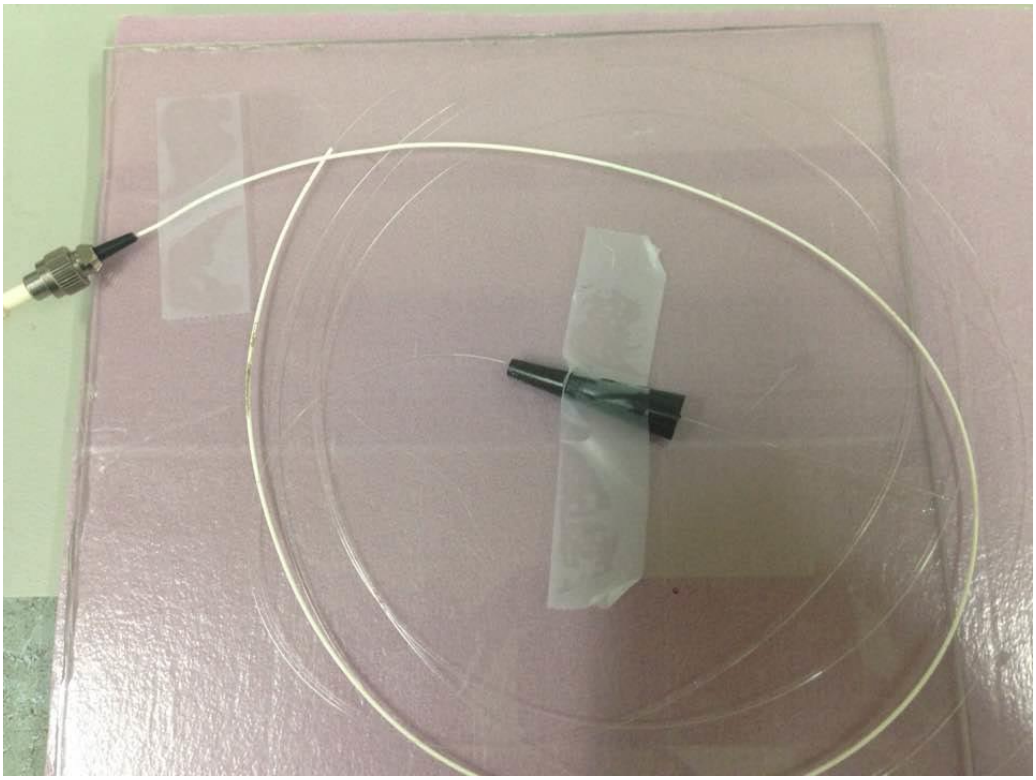

Fig. 6.7: Cone-shaped FOCS with an embedded FBG.

7. RESULTS AND ANALYSIS

In this chapter, the results from the DC magnetic field experiments are presented first. Then, the AC magnetic field results are presented. Next, thermal testing results are presented. Finally, the experimental results are compared with theoretical results determined from simulations. Most of the experimental results are plotted in terms of the sensor output optical powers versus DC or AC magnetic field.

7.1 DC MAGNETIC FIELD EXPERIMENTAL RESULTS

WLM and OSA were used to collect data for the DC experiments. With the WLM, the spectra had to be numerically integrated to obtain the total power reflected by the FBG. On the other hand, the OSA can provide the reflected optical power through the Thorlabs OSA software. Two cone-shaped sensors have been fabricated in the laboratory. Fig. 7.1 illustrates the typical results from DC experiments with the first cone-shaped sensor. In Fig 7.1 the reflected optical power is plotted as a function of the DC magnetic field from a coil. To explain the data in Fig.7.1, we next show a set of the reflection spectra for DC magnetic field ranging from 4kA/m to 384kA/m in Fig. 7.2. The experimental results in Fig. 7.1 show the expected monotonic increase of optical power with magnetic field when H is larger than 125kA/m. However, at low magnetic fields the total power dipped with increasing magnetic field owing to an initial strain distribution imposed on the FBG from the poor bonding of FBG to the cone with epoxy. It should be noted that this sensor was fabricated with the first method as described in Chapter six. In addition, the old experiment setup was used to obtain the results shown in Figs. 7.1 and 7.2 where we used the WLM to obtain the spectral power under the DC magnetic field generated by the DC coils.

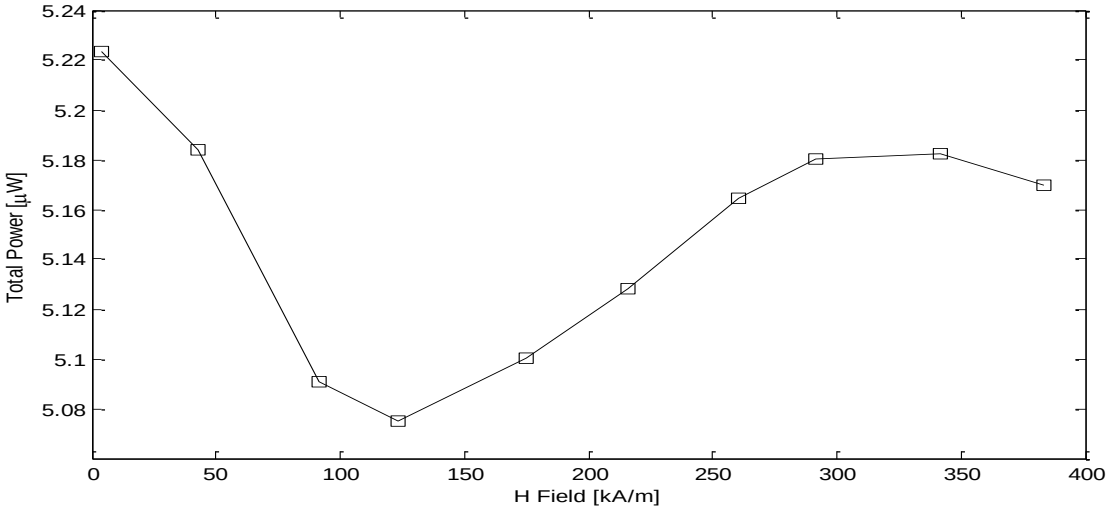

Fig. 7.1: The measured optical power as a function of magnetic field for the first cone-shaped FOCS.

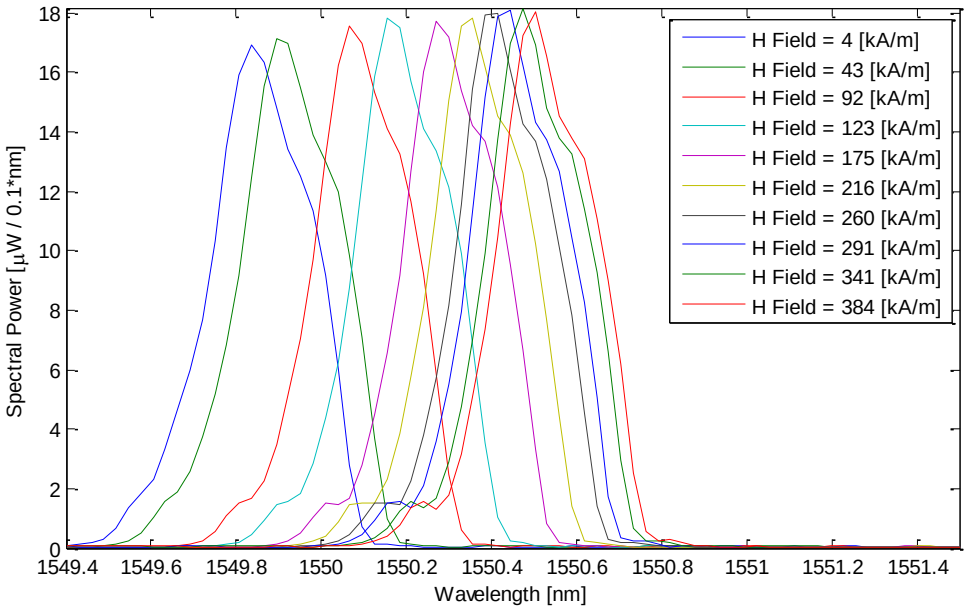

Fig. 7.2: Reflection spectra at various field values for the first cone sensor.

To overcome the drawbacks of the first sensor, a second cone-shaped sensor was fabricated with the second method (see chapter six). In addition, a new experimental was set up with the electromagnet as the source for the magnetic field and with the OSA as the instrument for acquiring the spectral data from the sensor. With the Thorlabs OSA software, the automatic setup routine was used to measure spectral power of the sensor. The automatic setup performs a series of measurements on the light source currently being coupled into the OSA and adjusts the measurement settings to those most suitable for that source. The settings that will be adjusted are the resolution, sensitivity, apodization, and gain. This routine is started by clicking on the "Auto-Setup" button in the sweep menu. It can take up to a minute to complete, and no other measurements can be performed while it is running. Upon the completion of the routine, the OSA software will obtain one measurement with the automatically determined settings, allowing user to inspect the result. The Thorlabs OSA software contains a number of analysis modes, each of which analyzes one aspect of the data. The result of each analysis is shown below the data display area. Total power, peak wavelength, and FWHM linewidth can be directly obtained from the analysis modes with the OSA software. During the embedding of the FBG inside the cone-shaped sensor, the FBG spectrum was monitored. Fig. 7.3 shows the spectrum power of the second cone sensor after the FBG was embedded and the epoxy was cured to bond the FBG inside the sensor. This enabled us to compare the spectra of the FBG before and after the embedding and the curing processes.

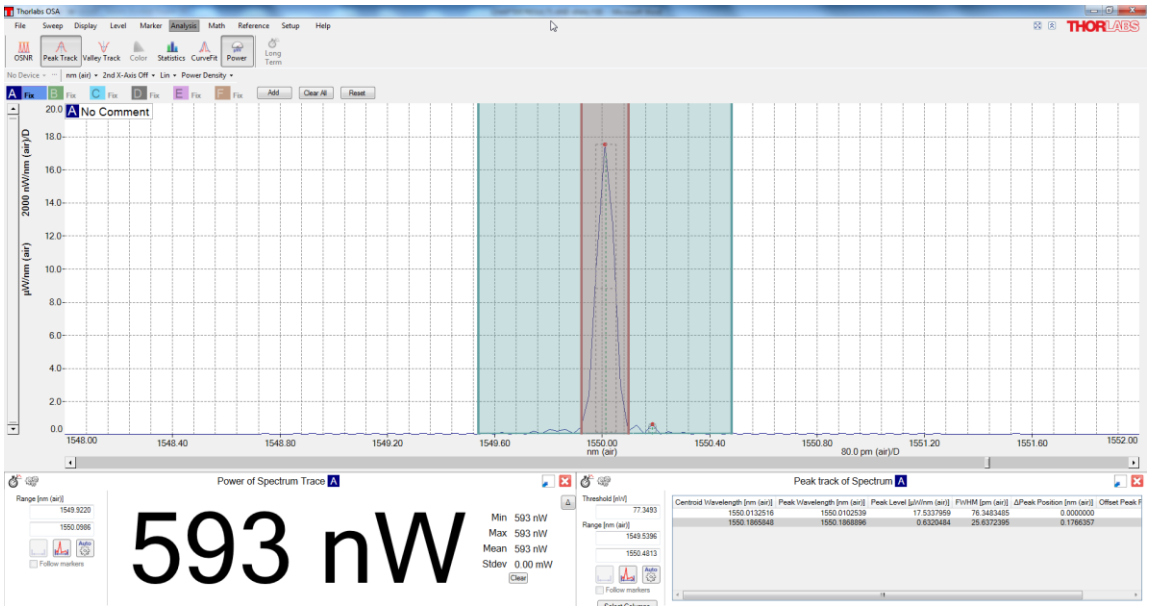

Fig. 7.3: Display of the cone sensor spectrum after the embedding of the FBG with OSA software. Analysis displayed under the graph and in a breakout window.

The results of the first two trials of the DC magnetic field measurements with the second cone-shaped sensor are presented in Fig. 7.4. They are also shown in Tables 7.1 and 7.2, including the magnetic field reading from the magnetometer and output power acquired by OSA. The sensor was placed in the air gap of a laboratory electromagnet, a Gauss meter with a Hall probe was placed tangent to the middle of the sensor to monitor the intensity of the magnetic field. By sweeping the magnetic field, spectra of returned signals from the FBG at various values of H were recorded with the OSA. An FBG with an overall length L = 3cm, linewidth (FWHM) = 0.066nm, and unchirped Bragg wavelength λ_B = 1550 nm was used to fabricate the FOCS.

Magnetic Field (Gauss)	Total Power [nW]	Magnetic Field (KA/m)	Normalized power Trial 1
27	902	2.148591732	1
537	982	42.73310222	1.088691796
1143	1058	90.95704998	1.172949002
1682	1070	133.8493071	1.186252772
2230	1090	177.4577615	1.208425721
2784	1099	221.5436808	1.218403548

Table 7.1: Values of magnetic field and total power for trial 1 DC testing.

Magnetic Field (Gauss)	Total Power (nW)	Magnetic Field (KA/m)	Normalized Power Trial 2
1.1	816	0.087535219	1
300	879	23.87324146	1.077205882
500	917	39.78873577	1.12377451
1000	982	79.57747155	1.203431373
1500	992	119.3662073	1.215686275
2000	998	159.1549431	1.223039216

Table 7.2: Values of magnetic field and total power for trial 2 DC testing.

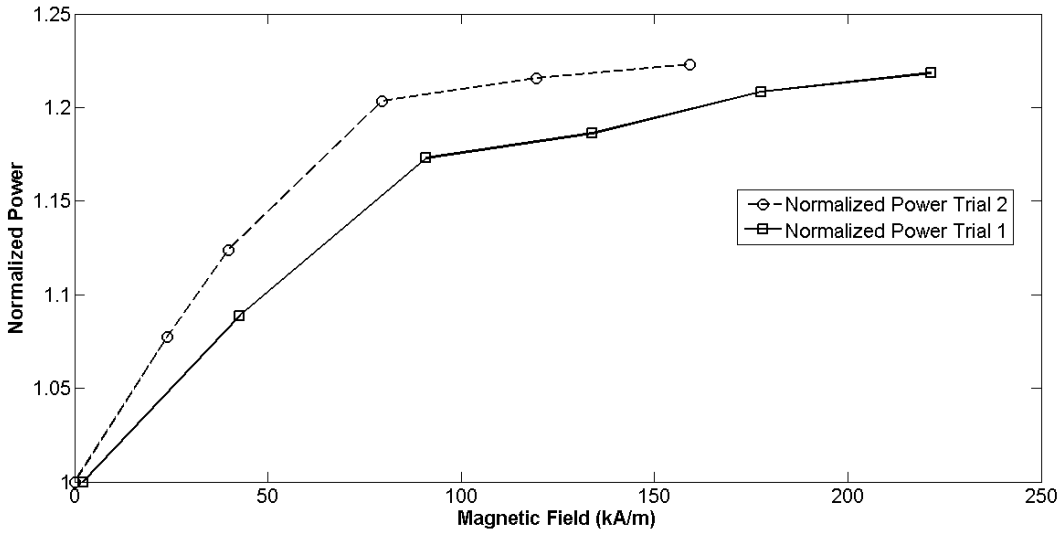

Fig. 7.4: The measured output power for two DC testing trials at magnetic field levels for the second cone sensor.

As seen in Fig. 7.4, sensor sn335611 trial (1) and trial (2) behaves as we would expect. Above a certain field level, the output power gradually increases with increasing field until the sensor reaches the saturation level. It can be seen also that only several data points were collected during the first two trials where we sweep the magnetic field in an increment of 500G. In Fig. 7.4,

the normalized power at each field value was obtained by dividing the power with the power at zero magnetic field. The initial two trials have been conducted to demonstrate that the transfer characteristics of FOCS have similar trend as those from the modeling and the theory. Several trials have been conducted later with more data points; we incremented the magnetic field in steps of 50G and recorded the corresponding total power. Fig. 7.5 shows the experimental response of the second cone-shaped FOCS. As *H* increases, the peak wavelength of the FBG will shift (Fig. 7.6) and the bandwidth of the reflected optical signal increases as shown in Fig.7.7. The raise in bandwidth translates into an increase in return power from the FBG. As a result, the chirped FOCS will respond to a wide range of *H* as shown in Fig. 7.5.

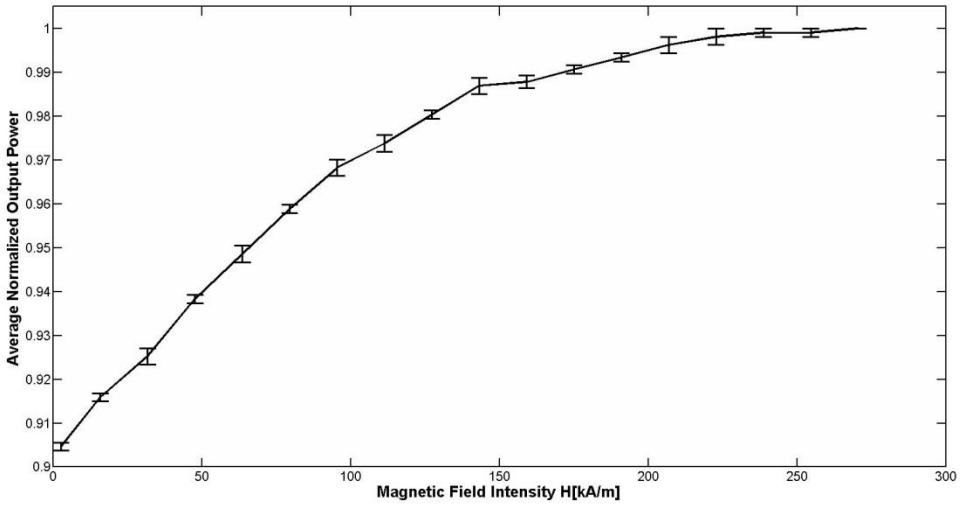

Fig. 7.5: Experimental response of the second cone-shaped FOCS.

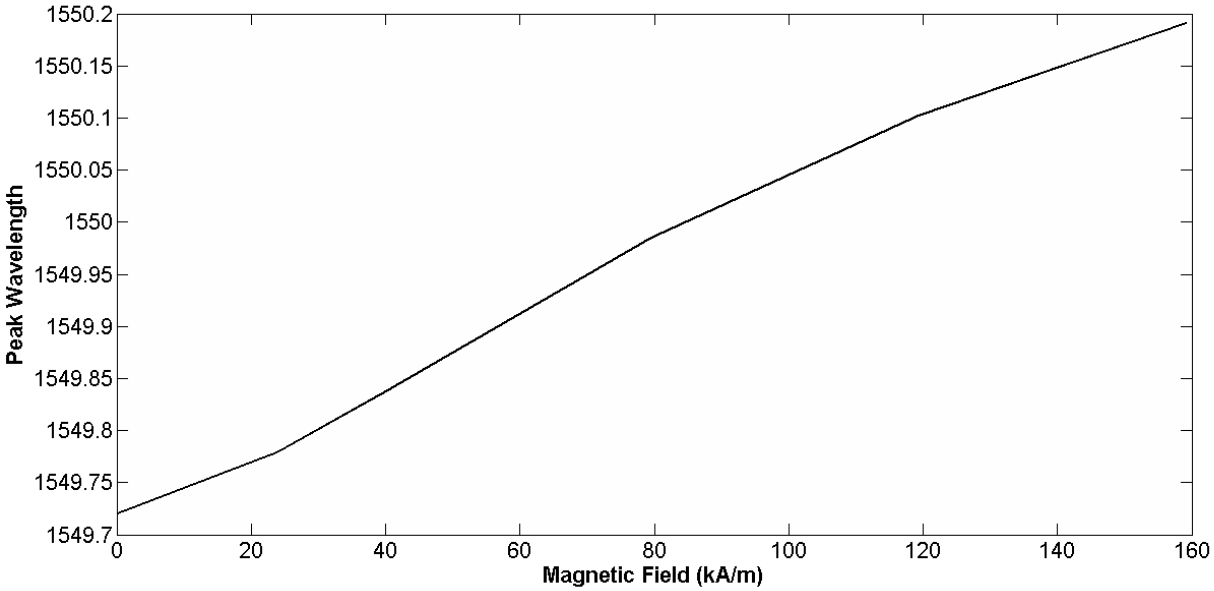

Fig. 7.6: Peak wavelength versus magnetic field.

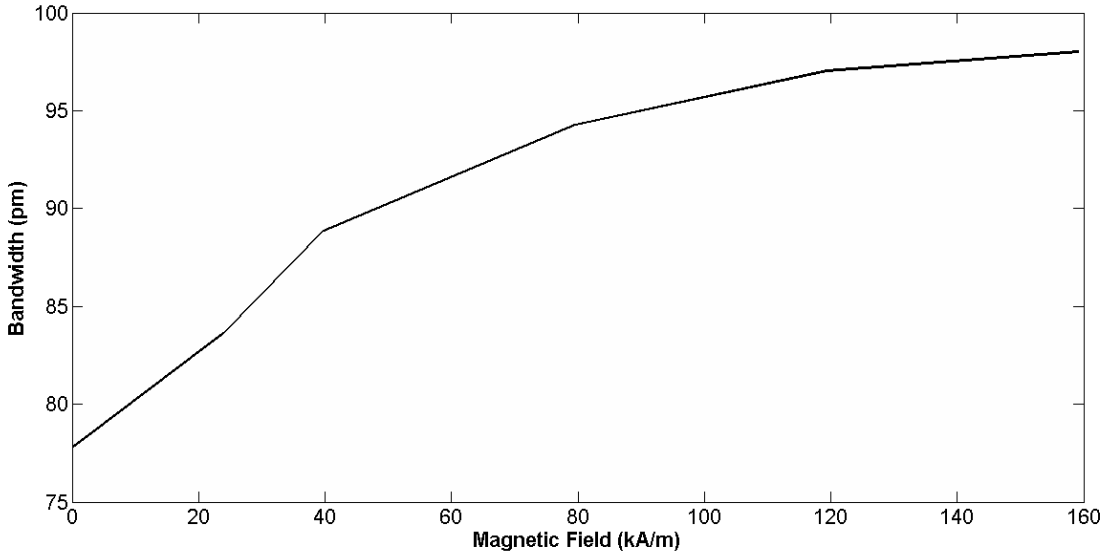

Fig. 7.7: FWHM linewidth versus magnetic field.

Fig. 7.8 below shows the reflection spetcra at various magnetic fields levels for the seond sensor. Another trial for the DC testing has been done by increasing the magnetic field to a certain vlaue and then decreasing the magnetic field while the total power monitored throughout the whole process. As *H* decreases the bandwidth of the reflected optical signal decreases, leading to the similar trend in the returned total power (see Fig. 7.9). The experiment has been conducted also with reversing the direction of the magnetic field to ensure that we have the same behavior. It can be seen form the output characteristics of this FOCS that the output power increases almost linearly over the range from 0 to 150 kA/m. The general response of the FOCS from the experiments agrees with the FBG strain models that were presented in Chapter 2.

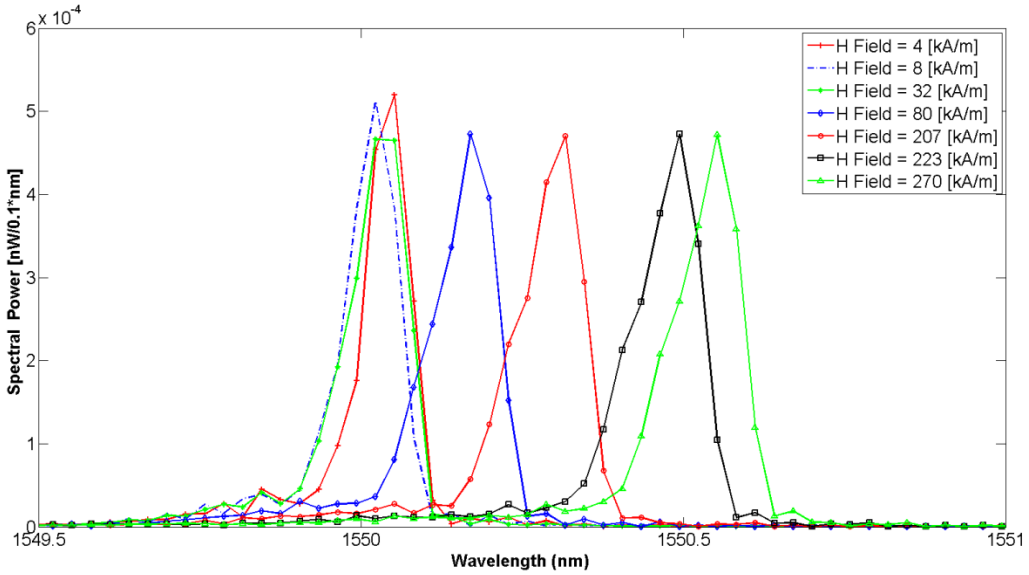

Fig.7.8: Reflection spectra at various field values for the second cone-shaped sensor.

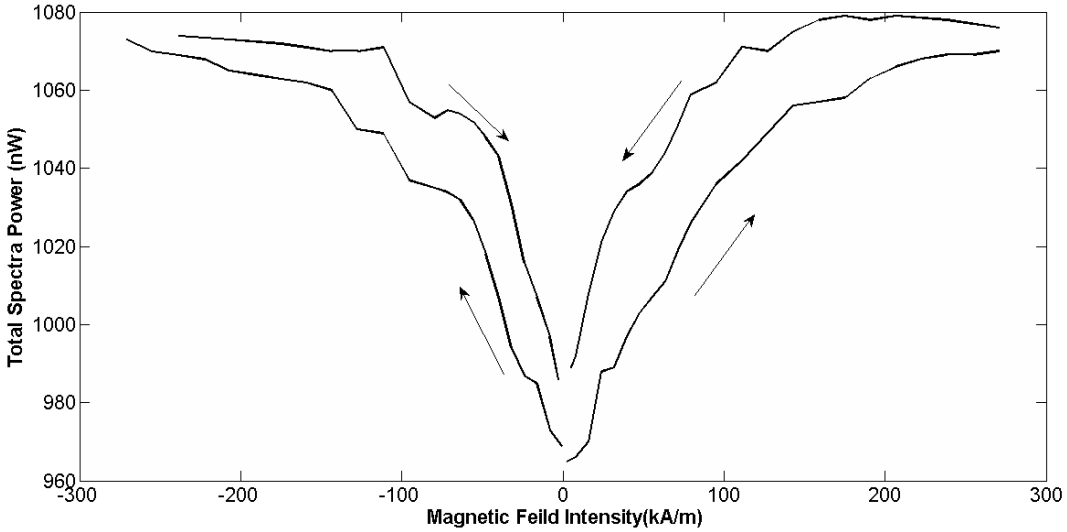

Fig. 7.9: Response of the FOCS with both increasing and decreasing the magnetic field.

7.2 AC MAGNETIC FIELD EXPERIMENTAL RESULTS

Since the intended application of the FOCS is monitoring the power lines against faults, its AC performance is of utmost importance. Several sets of AC experiments have been performed in the laboratory. An electromagnet driven by a sinusoidal signal source made up with a function generator connected to a power amplifier was used. The output voltage from the photodiode circuit was recorded by the oscilloscope in the first channel, and the output from the magnetometer was measured by the second channel. In addition, the output from the function generator was used as an external trigger to the oscilloscope. We used load resistance R_L of various values (4.75kΩ, 32kΩ, and 52kΩ) to obtain the output voltage from the photodiode circuit. It was difficult to generate adequate magnetic field for sinusoidal wave with 60 Hz owing to the impedance of the electromagnet. In the first AC experiment, a sinusoidal waveform with 2Vp-p amplitude and 3Hz frequency was outputted from the function generator that was connected to the power amplifier with a starting gain of 60. Then we stepped up the gain by an increment of 5 and recorded the output voltage of the photodiode on the oscilloscope. The load resistance of the photodiode in the

first trial was 4.75kΩ. In the second trial of the AC experiment, we used an input signal from the function generator with an input voltage of 3Vp-p and frequency of 2Hz. Now, the starting gain of the power amplifier for a clean display of the photodiode circuit voltage on the oscilloscope was 35. The load resistance of the photodiode is still fixed at 4.67KΩ. To increase the response from the FOCS, we increased the load resistance to 36KΩ, the input voltage has amplitude of 3V and a 2Hz frequency. The output voltage from the photodiode has increased slightly. However, in all those trials we were not able to read the amplitude of the AC magnetic field using the magnetometer. After reading the data sheet for the magnetometer, we found that the minimum frequency of 10 Hz was required for reliable the magnetometer reading. Since setting signal frequency at 10 Hz reduced the photodiode circuit to too low a voltage, we tried 6 Hz instead. The magnetometer was able to measure the peak value of the AC magnetic field with an input sinusoidal wave with a peak value of 2 volts and a 6 Hz frequency. Figs. 7.10 to 7.14 below show some samples of the oscilloscope data for the output voltage from the sensor with the input voltage of 2 Vp-p at a frequency of 6Hz from the function generator under different power amplifier gains to increase the magnetic field magnitude. To further boost the photodiode circuit voltage, we used R_L =52kΩ.

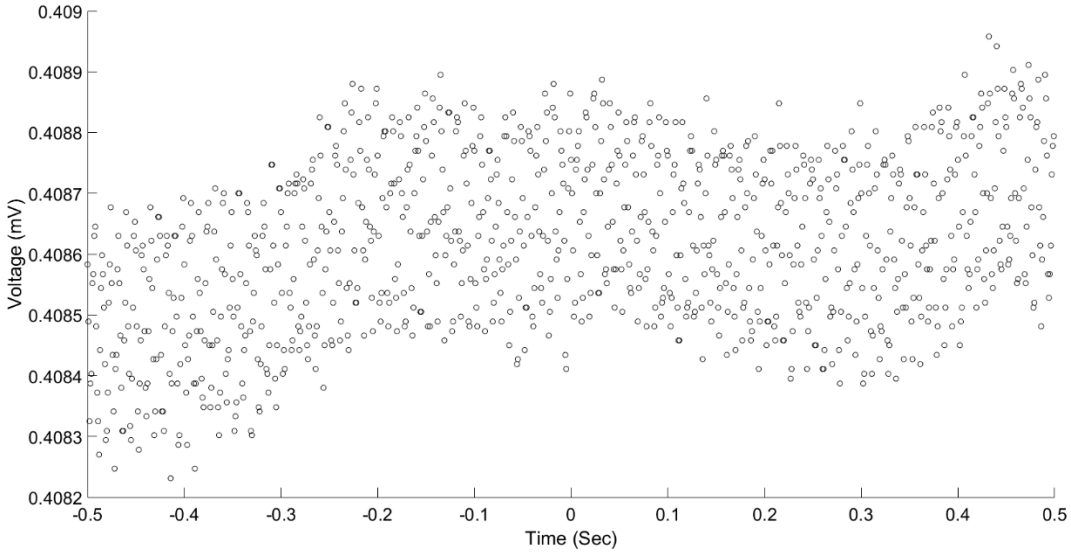

Fig. 7.10: AC experiment data collected by an oscilloscope for the output voltage from the sensor with output optical power 8.531μW, R_L =52kΩ, H = 0.

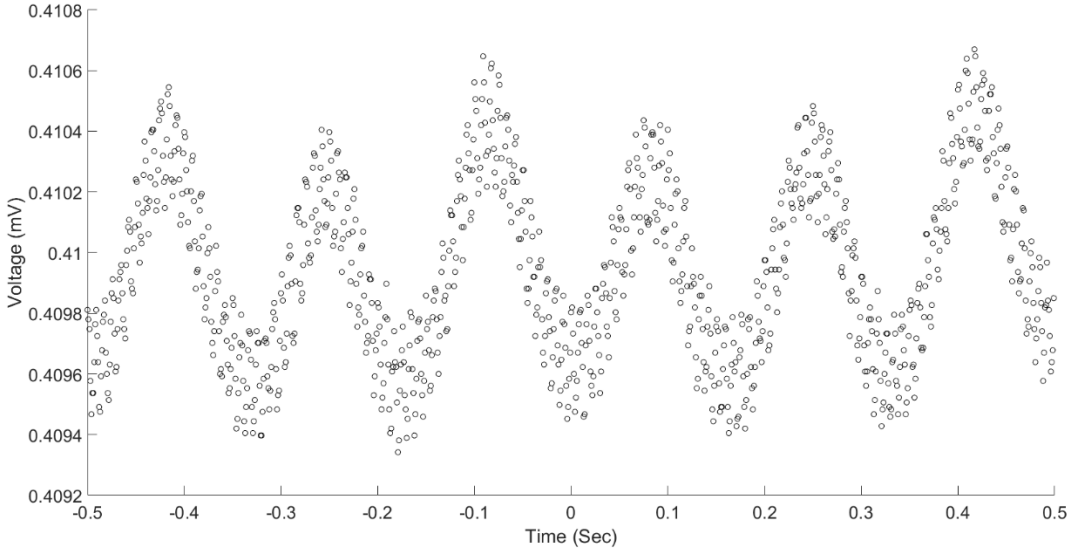

Fig. 7.11: AC experiment data collected by an oscilloscope for the output voltage from the sensor with output optical power at 9.643μW, R_L =52kΩ, under AC H field at 3Hz.

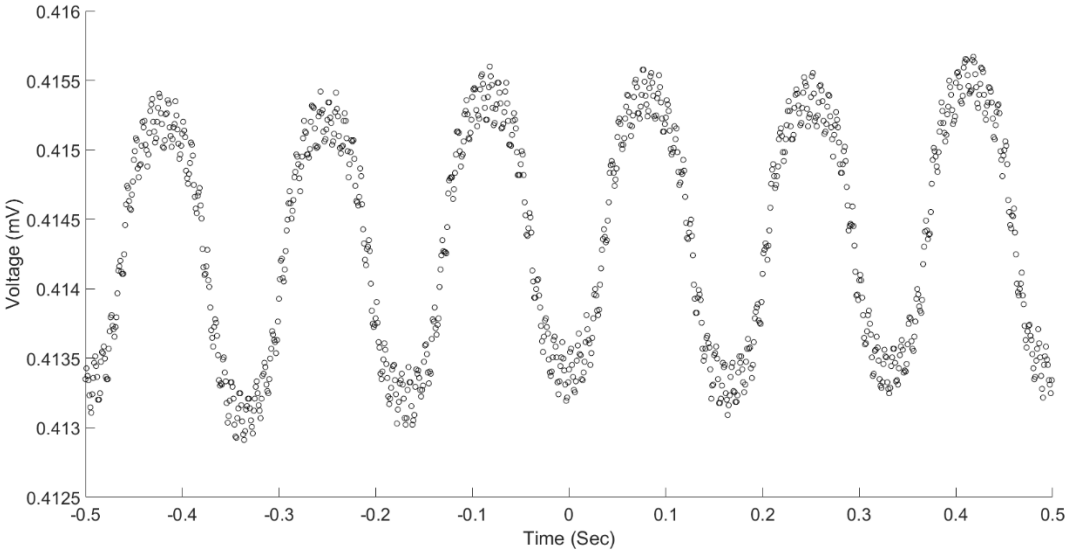

Fig. 7.12: AC experiment data collected by an oscilloscope for the output voltage from the sensor with output optical power at 12.388μW, R_L =52kΩ, under AC H field at 3Hz.

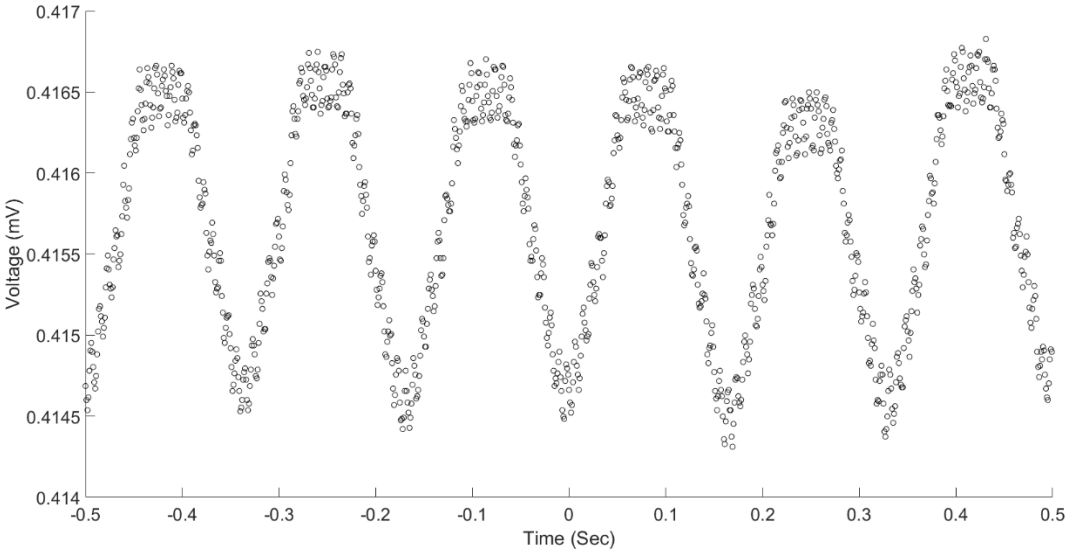

Fig. 7.13: AC experiment data collected by an oscilloscope for the output voltage from the sensor with output optical power at 13.812μW, R_L =52kΩ, under AC H field at 3Hz.

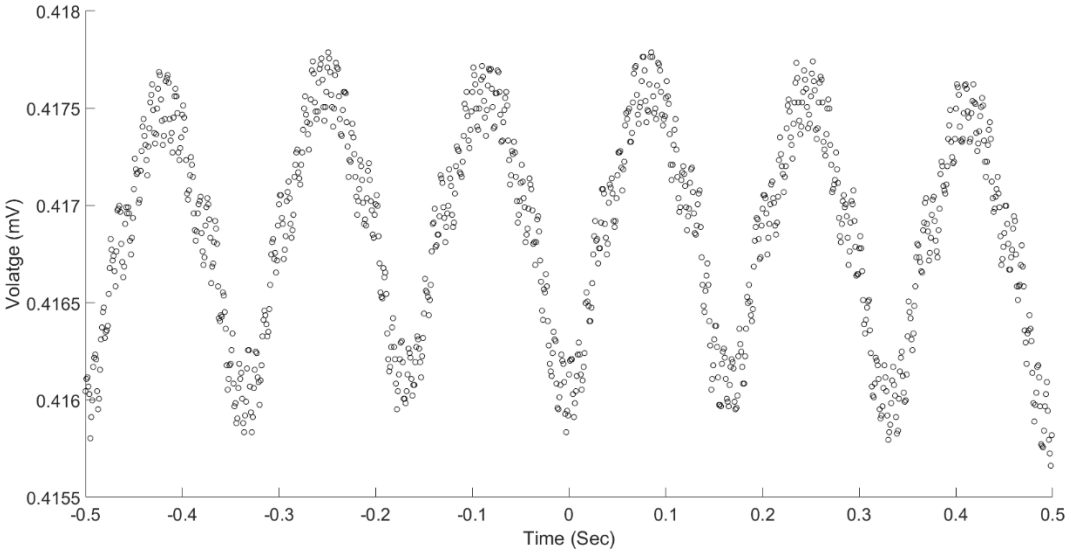

Fig. 7.14: AC experiment data collected by an oscilloscope for the output voltage from the sensor with output optical power at 16.405μW, R_L =52kΩ, under AC H field at 3Hz.

We kept increasing the gain of the power amplifier until we obtain the maximum possible output when the gain was 50. Some results of measured values for this experiment are shown in Table 7.3, including the magnetic field reading from the magnetometer, output voltages obtained from the oscilloscope trace data. The output power as a function of the peak amplitude of the AC magnetic field is shown in Fig. 7.15. The increase in the AC magnetic field translates into an increase in return power from the FBG. Data from both DC and AC magnetic field experiments exhibited almost linear response to magnetic field with slight fluctuations in output power.

H (G)	H(kA/m)	Gain of Power Amplifier	Output Voltage (mV peak)
0.000	0	10	0.6
164.4	13.082	45	0.7
193.5	15.398	50	0.75
219.1	17.435	55	0.8
243.8	19.401	60	1
273.2	21.741	65	1.3
299	23.794	70	1.4
306	24.351	75	1.5

Table7.3: Values of peak magnetic field, and voltage measured in the AC lab experiment.

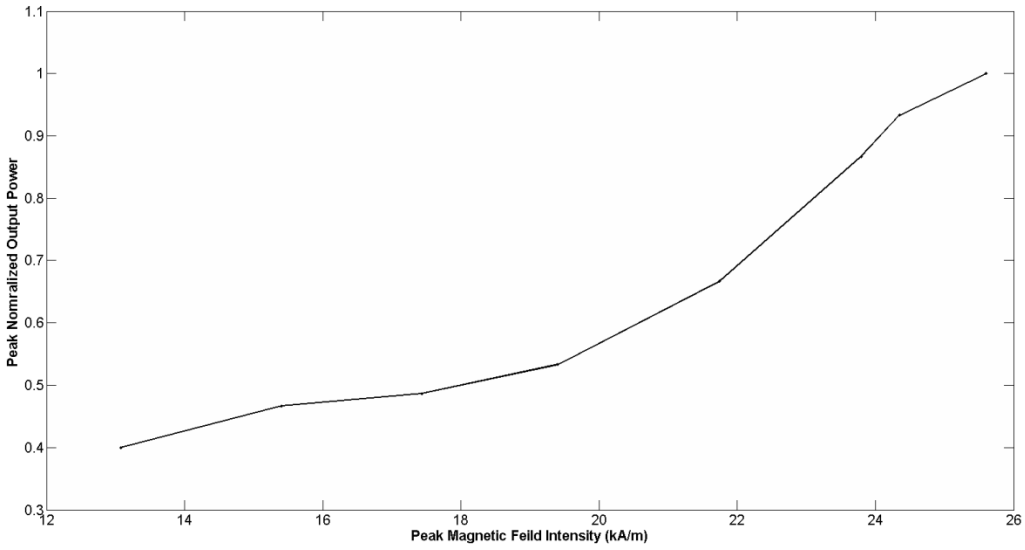

Fig. 7.15: Output of FOCS versus AC magnetic field intensity.

7.3 THERMAL TESTING RESULTS

Temperature variation effect on the response of the cone-shaped sensor has been investigated. Both DAC temperature sensor and the RTD thermometer have been used to measure the temperature inside the thermal chamber that has been described in chapter six. Table 7.4 below shows some temperature measurements that have been performed with both sensors. The two sensors placed very close to each other inside the thermal chamber in order to get consistent temperature measurements. Fig. 7.16 shows the real time graph and table of temperature readings for the thermal chamber generated by the SE-376 software for the RTD thermometer. In the first trials of thermal testing, we acquired the spectrum three to five minutes after increasing the temperature inside the thermal chamber. The results of those trials are shown in Fig. 7.17 below. Trials 1, 2, and 3 ran from 23ºC– 50ºC. In the figure, beyond 43ºC the sensor output power starts to increase in an exponential fashion as the temperature is rising. This is an indication that the chamber has not reached the thermal equilibrium. For this reason, the thermal testing has been repeated again with waiting half an hour after each temperature set point to ensure that the chamber has reached thermal equilibrium before collecting FOCS data. The new results of thermal testing are shown in Fig. 7.18. It can be seen now that the output response of the current sensor is almost independent of the temperature effect and the output became steadier since it depends on the linewidth of the reflected spectrum. In fact, the peak wavelength of the FOCS tracks the steady increases in temperature as shown in Fig. 7.19. However, we could not increase the temperature inside the thermal chamber beyond 39ºC since the heat elements have insufficient power to reach higher temperatures within half an hour. With the limited thermal data, we can observe the potential effect on restricting the FOCS resolution owing to the low sensitivity of the FOCS.

DAC Temperature Sensor in Celsius	RTD Thermometer in Celsius
25.057	25.3
27.12	27.3
29.104	29.3
31.11	31.34
33.11	33.34
35.126	35.31
37.197	37.34
39.26	39.46
41.179	41.4
43.19	43.12
45.029	45.26

Table 7.4: Comparison of temperature measurements with DAC and RTD sensors.

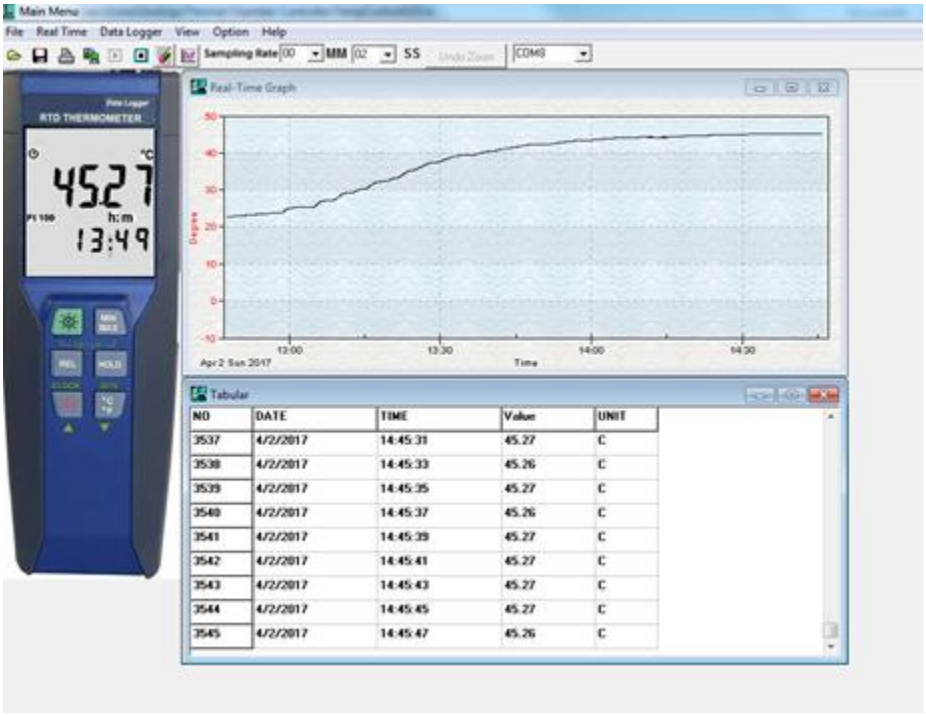

Fig 7.16: Real time graph and table showing the temperature measurement with the SE-376 software.

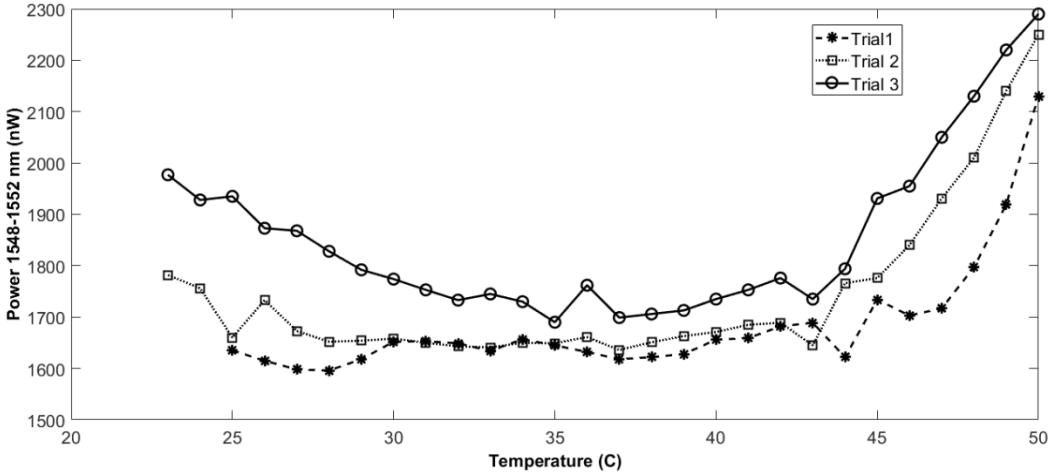

Fig. 7.17: Output of FOCS versus. Temperature when data were taken every three to five minutes.

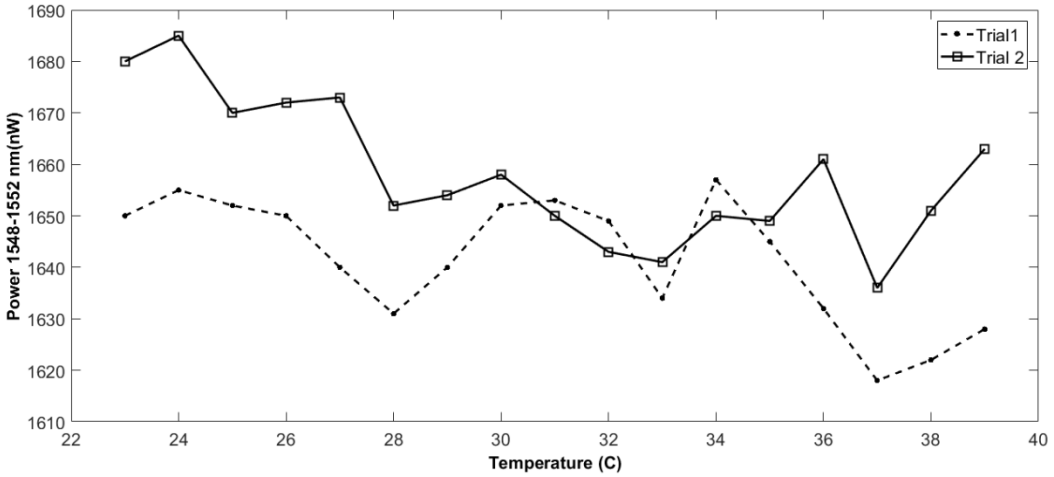

Fig. 7.18: Output of FOCS versus temperature when data were taken every thirty minutes.

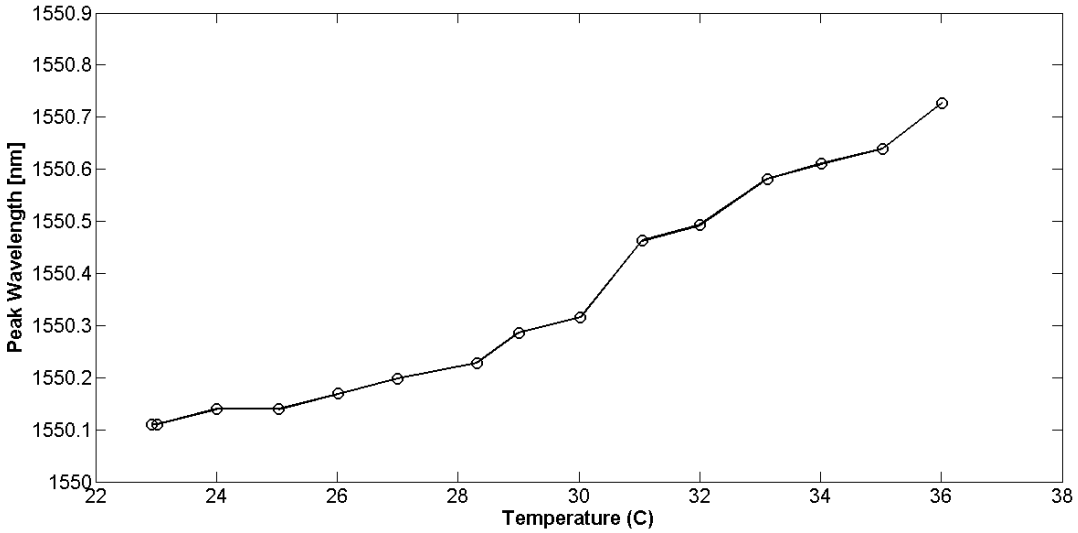

Fig. 7.19: Peak wavelength of FOCS versus temperature.

8. CONCLUSIONS AND FUTURE WORK

8.1 CONCLUSIONS

This thesis presented modeling and experimental verification of several prototypes of the chirped FOCS. The main intended application for the prototyped FOCS is the detection of faults in electrical power distribution systems. This FOCS has several advantages over traditional fault detection schemes involving current transformers, including, compact design, high bandwidth, and immunity to electromagnetic interference, among others. Additionally, it is more cost effective than other types of OCS typically used, requiring only a simple power measurement to detect current levels.

After a quick review of the conventional current sensors and optical current sensor technology, modeling methods and considerations were presented. This began with a basic review of FBG theory, and then different modeling methods for obtaining the theoretical reflection spectra were presented. In addition, the effects of temperature and strain on the output characteristics of the FBG were reviewed. With the FBG theory, we were able to simulate the spectral response of the sensor which consists of the FBG embedded in composite blocks with different volume fractions of T-D particles.

It was imperative to examine the material behavior models of T-D in order to understand the experimental results and to optimize the transducer performance. Several models have been used to explain the magnetostriction in T-D. Some are based on purely physical principles while others model the magnetostriction with the phenomenological approach. Generally, the analysis considers only single crystal.

Accurate modeling of magnetostrictive materials requires coupling of electrical, mechanical, and magnetic domains. For this purpose, several models were implemented by

combining finite element solutions of mechanical and magnetic boundary value problems with COMSOL Multiphysics software package. These models describe the magnetomechanical behavior of T-D composite when applying magnetic field. There are limitations or uncertainty of numerical simulations since the material parameters for composites are unknown and assumed their magnitude being similar to those of T-D.

Experimental components were described. In addition, the experimental setups for both DC and AC magnetic field measurements, sensor output spectrum, temperature, and total output power were explained.

Several FOCS prototypes and configurations have been developed. Sensor fabrication methods are presented in details, particularly focusing on the shape of the T-D composites since sensor behavior is very sensitive to variability in these factors. The prototyped sensors use T-D composites as a transducer. T-D composite reduces the eddy current loss and improves the fracture toughness in comparison to monolithic T-D. The magnetostrictive composite was fabricated by integrating magnetostrictive powders embedded in a nonmetallic binder (epoxy). Owing to the importance of having zero initial strain on the FBG, we developed a two-step method to achieve this goal. First, the composite was prototyped then the FBG was embedded inside.

We then presented the experimental results obtained for several prototypes of the FOCS. Both DC and AC magnetic field results included both the output power as a function of incident field and a sample of the spectra at various field values Although an OSA or wavelength meter is used to characterize FOCS, it is not required for practical applications. We have demonstrated that a photodiode circuit is sufficient to capture the waveform of AC currents. According to the data, the prototyped sensors exhibited behavior almost similar to that predicted by the model but with very lower sensitive. Sensor in both DC and AC responses of FOCSs exhibited linear increase

proportional to the increment in the magnetic field with slight fluctuations of output power, even for low fields. The results of the different DC and AC trials demonstrate repeatability. In addition, thermal testing has confirmed that the output characteristics of the sensor are almost independent of temperature increase but with random fluctuations. Unfortunately, such random fluctuations can hinder the FOCS in resolving the actual current level owing to the low output from the FOCS in comparison to these fluctuations.

In summary, we have successfully design chirped FOCSs, their prototypes were fabricated by embedding an FBG in T-D composite and demonstrate their capability in current sensing. These sensor prototypes were characterized with both direct and alternating magnetic field measurements. We observed that the repeatability in responses and FOCS prototypes had responses in trend similar to simulations. However, FOCS prototypes output within a narrow power range such that thermal variations can prevent them from providing definitive current level. Such low sensitivity can be attributed to the low magnetostriction of the T-D composite. At current stage, our results have shown consistency among different trials and support the operation of FOCS as a current sensing device that is useful for fault detection and location. Further development will be required for chirped FOCS to function as a current measuring device.

8.2 FUTTURE RESEACH DIRECTIONS

Several modifications have already been implemented to sensor prototyping process and experimental procedures during the thesis research, such as replacing the WLM with the OSA for spectral data collection, switching to the electromagnet driven by a power amplifier as the magnetic field source and developing new techniques for sensor construction. However, several areas are identified that will enhance results for both DC and AC testing. Additionally, more

research and testing are needed to determine the effect of temperature on the output spectrum of the current sensor.

In order for DC and AC experimental data to be more accurate, we should wait longer at each field/current level before recording the spectrum to allow the thermal chamber to reach the equilibrium at each level. Since the whole testing procedure will last for a long time, enhanced automation program should be developed with more flexibility in controlling the DC and the AC testing processes.

The limitation in performing AC magnetic field measurements at high field levels and frequency around 60 Hz can be alleviated if additional power amplifier can be used to drive the electromagnet at high current.

Regarding the T-D transducer prototyping, several modifications can be done to improve the response of the FOCS such as using the heat in the curing process to ensure that the T-D composite fully cure before embedding the FBG inside. Another improvement can be performed to reduce thermal variations is to investigate the use of other epoxies that has higher thermal conductivity or low thermal expansion coefficient. Similarly, we can ensure temperature spreading evenly on the sensor and eliminate any thermal gradient that might affect the sensor characteristics by the enclosing the FOCS with a heat conductive layer or film.

Since the operating principle of the sensor relies on the magnetostrictive properties of T-D, another important future enhancement to the transducer fabrication involves using high magnetic field intensity during the fabrication of the transducer. This will align the magnetic domains in T-D in a certain direction in order to optimize the sensor performance.

Although the simulation models that we used to investigate the T-D behavior with varying magnetic field are useful, many improvements can be added to the present models. The models built in COMSOL need a long time to converge. In future models, we will investigate techniques that accelerate the simulation process, such as experimenting with other meshing options to reduce the computation time. We should also research on the appropriate model parameters for modeling composites and finally reach our goal of constructing an equivalent model that can provide sufficient accuracy within a short execution time.

9. REFERENCES

[1] Horowitz, Stanley H., et al. *Power System Relaying*. 4th ed., Hoboken, Wiley, 2013.

[2] C. T. Law, K. Bhattarai, and D. C. Yu, "Fiber-Optics-Based Fault Detection in Power Systems," *IEEE Trans. on Power Delivery*, vol. 23, no. 3, pp. 1271-1279, July 2008.

[3] Ziegler, S., et al. "Current Sensing Techniques: A Review." *Sensors Journal, IEEE*, vol. 9, no. 4, 2009, pp. 354–376.

[4] Silva, Ricardo M., et al. "Optical Current Sensors for High Power Systems: A Review." *Applied Sciences-Basel*, vol. 2, no. 3, 2012, pp. 602–628.

[5] Plavsic, Aleksandar. *Experimentations and Prototyping on Fiber Bragg Gratings-Based Magnetostrictive Current Sensor / by Aleksandar Plavsic.* 2008.

[6] Mueller, Aaron. *Modeling and Experimental Verification of a Fiber Bragg Grating-Based Magnetostrictive Current Sensor / by Aaron Mueller.* 2012.

[7] Y. N. Ning, Z. P. Wang, A. W. Palmer, T. V. Grattan, and D. A. Jackson, "Recent progress in optical current sensing techniques," *Rev. Sci. Instrum*., vol. 66, pp. 3097–3111, 1995.

[8] "Proposal for detection of magnetic fields through magnetostrictive perturbation of optical fibers," *Opt. Lett*., vol. 5, pp. 87–89, Mar. 1980.

[9] J. Mora, A. Díez, J. L. Cruz, and M. V. Andres, "A Magnetostrictive Sensor Interrogated by Fiber Gratings for DC-Current and Temperature Measurement," *IEEE Photon. Technol. Lett.*, vol. 12, no. 12, pp. 1680-1682, December 2000.

[10] Yi B, Chu BCB, Chiang KS. Temperature compensation for a fiber-Bragg-grating-based magnetostrictive sensor. Microw Opt Technol Lett 2003; 3: 211–213.

[11] K. S. Chiang, et al.,"Temperature-compensated fiber-Bragg-grating-based magnetostrictive current sensor for dc and ac currents," Opt. Eng. **42**, 1906—1909 (2003).

[12] Satpathi, D., et al. "Design of a Terfenol-D Based Fiber-Optic Current Transducer." *Sensors Journal, IEEE*, vol. 5, no. 5, 2005, pp. 1057–1065.

[13] Minghong Yang, et al. "Optical Fiber Magnetic Field Sensors with TbDyFe Magnetostrictive Thin Films as Sensing Materials." *Optics Express*, vol. 17, no. 23, 2009, pp. 20777–20782.

[14] Quintero, Sully M. M., et al. "A Magnetostrictive Composite-Fiber Bragg Grating Sensor." *Sensors (Basel, Switzerland)*, vol. 10, no. 9, 2010, pp. 8119–8128.

[15] McKnight, Geoffrey, and Carman, Greg P. "[112] Oriented Terfenol-D Composites." *[112] Oriented Terfenol-D Composites*, 2002, pp. ProQuest Dissertations and Theses.

[16] Chakrabarti, Suryarghya, and Dapino, Marcelo. “Modeling of Three-Dimensional Magnetostrictive Systems with Application to Galfenol and Terfenol-D Transducers.” *Modeling of Three-Dimensional Magnetostrictive Systems with Application to Galfenol and Terfenol-D Transducers*, 2011, pp. ProQuest Dissertations and Theses.

[17] Pei, Yongmao, et al. “A Multi-Field Domain Rotation Model for Giant Magnetostrictive Materials.” *Acta Mechanica*, vol. 224, no. 6, 2013, pp. 1323–1328.

[18] Sandlund, L, et al. “Magnetostriction, Elastic Moduli, and Coupling Factors of Composite Terfenol-D.” *Journal of Applied Physics*, vol. 75, no. 10, 1994, pp. 5656–5658.

[19] T. Erdogan, "Fiber Grating Spectra," *J. Lightw. Technol.*, vol. 15, no. 8, pp. 1277-1294, August 1997.

[20] Othonos, Andreas. “Fiber Bragg Gratings.” *Review of Scientific Instruments*, vol. 68, no. 12, 1997, pp. 4309–4341.

[21] Mohanraj Prabhugoud, and Kara Peters. “Modified Transfer Matrix Formulation for Bragg Grating Strain Sensors.” *Journal of Lightwave Technology*, vol. 22, no. 10, 2004, pp. 2302–2309.

[22] Zhang, C, et al. “Domain Rotation Simulation of Anisotropic Magnetostrictions in Giant Magnetostrictive Materials.” *Journal of Applied Physics*, vol. 110, no. 6, 2011, pp. Journal of Applied Physics, 15 September 2011, Vol.110(6).

[23] Zhang, C, et al. “Induced Additional Anisotropy Influences on Magnetostriction of Giant Magnetostrictive Materials.” *Journal of Applied Physics*, vol. 112, no. 10, 2012, pp. Journal of Applied Physics, 15 November 2012, Vol.112(10).

[24] Clark, A., et al. “Effect of Stress on the Magnetostriction and Magnetization of Single Crystal Tb.27Dy.73Fe2.” *Magnetics, IEEE Transactions On*, vol. 20, no. 5, 1984, pp. 1443–1445.

[25] Kleinke, D, and Uras. “Modeling of Magnetostrictive Sensors.” *Review of Scientific Instruments*, vol. 67, no. 1, 1996, pp. 294–301.

[26] Armstrong, W.D. “Burst Magnetostriction in Tb{Sub 0.3}Dy{Sub 0.7}Fe{Sub 1.9}.” *Journal of Applied Physics*, vol. 81, no. 8, 1997, pp. 3548–3554.

[27] Zhang, Chang-Sheng, et al. “Domain Rotation Simulation of the Magnetostriction Jump Effect of (110) Oriented TbDyFe Crystals.” *Chinese Physics Letters*, vol. 29, no. 2, 2012, p. 4.

[28] C Tannous. “The Stoner-Wohlfarth Model of Ferromagnetism.” *European Journal of Physics*, vol. 30, no. 1, 2009, p. 227.

[29] Jiles, D.C.; Thoelke, J. B., "Modelling of the combined effects of stress and anisotropy on the magnetostriction of $Tb_{0.3}Dy_{0.7}Fe_2$," *Magnetics, IEEE Transactions on* , vol.27, no.6, pp.5352,5354, Nov 1991.

[30] Armstrong, William D. “Nonlinear Behavior of Magnetostrictive Particle Actuated Composite Materials.” *Journal of Applied Physics*, vol. 87, no. 6, 2000, pp. 3027–3031.

[31] Armstrong, W.D. “Magnetization and Magnetostriction Processes in Tb{Sub (0.27-0.30)}Dy{Sub (0.73-0.70)}Fe{Sub (1.9-2.0)}.” *Journal of Applied Physics*, vol. 81, no. 5, 1997, pp. 2321–2326.

[32] Yang, Y, et al. “Effects of Magnetocrystalline Anisotropy Constant K 2 on Magnetization and Magnetostriction of Terfenol-D.” *Applied Physics Letters*, vol. 98, no. 1, 2011, pp. Applied Physics Letters, 03 January 2011, Vol.98(1).

[33] Smith, R, et al. “Free Energy Model for Hysteresis in Magnetostrictive Transducers.” *Journal of Applied Physics*, vol. 93, no. 1, 2003, pp. 458–466.

[34] C de la Fuente. “Magnetocrystalline Anisotropy in a (110) (Tb 0.27 Dy 0.73)Fe 2 Thin-Film.” *Journal of Physics: Condensed Matter*, vol. 16, no. 17, 2004, pp. 2959–2966.

[35] Liu, X, and Xj Zheng. “A Nonlinear Constitutive Model for Magnetostrictive Materials.” *Acta Mechanica Sinica*, vol. 21, no. 3, 2005, pp. 278–285.

[36] Zheng, X, and Liu. “A Nonlinear Constitutive Model for Terfenol-D Rods.” *Journal of Applied Physics*, vol. 97, no. 5, 2005, pp. Journal of Applied Physics, 01 March 2005, Vol.97(5).

[37] Tschopp, M A, et al. “Multi-Scale Characterization of Orthotropic Microstructures.” *Modelling and Simulation in Materials Science and Engineering*, vol. 16, no. 6, 2008, p. 14.

[38] http://www.comsol.com/model/nonlinear-magnetostrictive-transducer-6063.

[39] Wysin GM (2012) Demagnetization fields.
https:// www.phys.ksu.edu/personal/wysin/notes/demag.pdf.

APPENDIX A: LIST OF MATERIALS

CURRENT SOURCES AND POWER SUPPLIES

- DC Regulated Power Supply – Mf: BK PRECISION; Model: 1665
- AC Adapter 5V 3A – Mf: D-Link; Model: JTA0302C
- DC power supply – Mf: BK Precision; Model: 1790; Output current = 0-20 A; Output voltage = 0-32 V
- DC power supply – Mf: Mastech; Model: HY5020E; Output current = 0-20 A; Output voltage = 0-50 V
- Variable Autotransformer – Mf: The Superior Electric Co. Model: Powerstat 3PN116C; Ratings: 120 V in, 0-140 V out, 10 A, 1.4 kVA

OPTICAL LINK AND MEASUREMENT EQUIPMENT

- Optical isolator – Mf: Newport; Model: ISC-1550; Operating wavelength = 1550nm; Insertion Loss = 0.35dB
- Optical isolator (substituted circulator for dual stage isolator) – Mf: JDS Uniphase; Model: CR5500P-3P-CV5A; S/N: HD122865
- 3-port Optical Circulator – Mf: New Focus, Inc; Model: 0803; Operating wavelength = 1550nm; Insertion loss (port 1 to port 2) = 0.62dB, Insertion loss (port 2 to port 3) = 0.58dB
- 3-port Optical Circulator – Mf: New Focus, Inc; Model: CIR10BN32N-01; S/N: 001 803722
- Fiber splice (x3) – Mf: Siemon; Model: ULTRAsplice; Average insertion loss < 0.2dB [2]

- Fiber FC-FC ceramic mating sleeve – Mf: FIS, Inc; Model: F18520; Typical insertion loss = 1dB
- Superluminescent Light Emitting Diode (SLED) with driver board – Manufacturer (Mf): Exalos; SLED Model: EXS1520-2xxx; Max. optical output power = 16mW; Typical peak wavelength = 1550nm; Bandwidth = 60 nm; Driver Board Model: EBD2000-0000
- Multi-Wavelength Meter; Mf: Hewlett Packard/Agilent; Model: 86120C
- Magnetometer – Mf: Alpha Lab, Inc/USA; Model: DC Magnetometer (Gauss); With transverse probe –DC/AC adjustable range; Website: www.trifield.com; S/N: 2450
- GPIB-USB cable
- Desktop computer
- Fiber Optic Power Meter – Mf: Photodyne Products 3M; Model: 17*TF; S/N: 21311
- Digital Phosphor Oscilloscope – Mf: Tektronix; Model: 2024B
- InGaAs PIN photodiode – Mf: NEC; Model: NR7800; Responsivity $\mathcal{R}$ = 0.94 A/W @ λ = 1550 nm.
- Load resistor – 4.75kΩ, 36 kΩ, and 50 kΩ nominal
- Battery – 9V
- Photodiode circuit board and fixture
- Digital Multimeter – Mf: TENNA TM; Model: True RMS Multimeter 72-4020

SENSOR MATERIALS – INCLUDES TRANSDUCER/FIBER PARTS

- Terfenol-D Powder –250-300μm Particle size.

- Monel-400 rod (x2) – Cylindrical shape; Length = ? Diameter = 0.25 in.
- Fiber Bragg gratings (x10) – Mf: O/E Land, Inc.; sn: 2393-1-x, 2459-x (x=1-5); Grating length = 30 mm; Initial center wavelength ≅ 1550nm; FWHM = 0.1 nm; Peak reflectivity ≅ 97%

AUXILIARY FIBER MATERIALS AND EQUIPMENT

- Fiber type: SMF-28, single-mode fiber with 900μm or 250μm jacket
- Fiber optic stripper – Mf: Clauss; Model: NO-NIK
- Optical fiber cleaver – Mf: Fitel; Model: S323
- Fusion splicer – Mf: Ericsson; Model: FSU975
- Methanol
- Kim Wipes
- Fiber FC-FC ceramic mating sleeve (x2) – Mf: FIS, Inc; Model: F18520; Typical insertion loss = 1dB

APPENDIX B: SCHEMATIC DRWAING OF THE CONE SENSOR

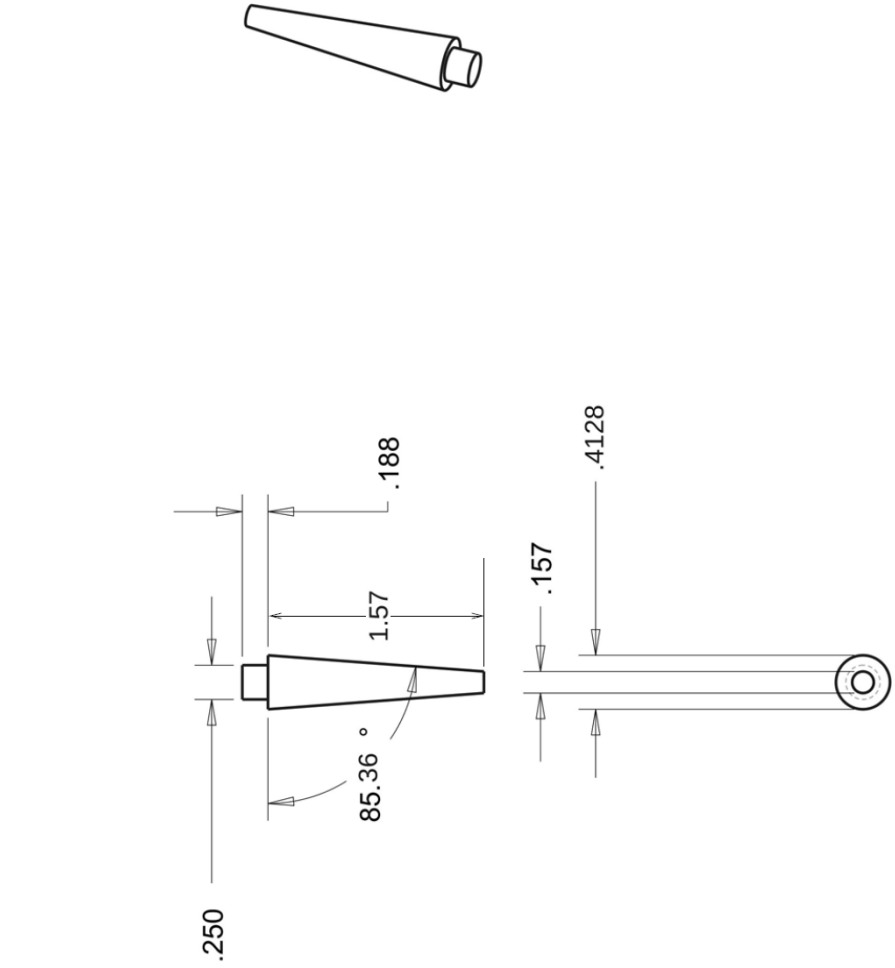

THIS IS HOW THE PARTS ARE
INTENDED TO BE ASSEMBLED

PART: POST
•PRESS INTO BASE

PART: BASE
Ø1.25
Ø1.00
.10
Ø.25
THRU
.20

CURRICULUM VITA

Suha Lasassmeh

EDUCATION:

Ph.D., Electrical Engineering, University of Wisconsin Milwaukee, Milwaukee, WI, 2011-August 2017.

Master of Science, Electrical & Computer Engineering, University of North Carolina, Charlotte, NC, 2011.

Master of Science, Electrical Engineering, Mut'ah University, Karak, Jordan 2007.

Bachelor of Science, Electrical Engineering, Mu'tah University, Karak, Jordan, 2004.

PROFESSIONAL EXPERINCE:

- **Teaching Assistant, University of Wisconsin, Milwaukee,** August 2011 – August 2017.
  Taught the following courses as a lecturer:
  - Electronic Technology in the World around us, Fall 2015, Spring 2016.
  - Electronics II, Summer 2015
  - Electrical Circuit II, Summer 2014
  - Electronic I, Summer 2012

  Taught the following discussion and laboratory sections:
  - Digital Logic, Spring 2017.
  - Electronics I Lab, Fall 2011, Spring 2012, Fall 2012, Spring 2013, Fall 2013, Spring 2014.
  - Capstone Design Project, Fall 2013, Spring 2015, Spring 2017.
  - Electrical Circuit II Lab, Spring 2014.
  - Electrical Circuit I, Fall 2014.

- Teaching Assistance, Department of Electrical & Computer Engineering, University of North Carolina, charlotte, August 2007 – May 2010.
  Taught following engineering classes:

  - Basic Electrical Engineering, Spring 2010
  - Solid State Microelectronics I, Spring 2009
  - Digital Signal Processing, Spring 2009
  - Signals and Systems, Fall 2008
  - Electrical Engineering Design I, Fall 2008
  - Professional Practice, Spring 2008 and Fall 2007

- Teaching Assistance, Department of Electrical Engineering, Mu'tah University, Karak, Jordan, August 2005 – May 2006.
  Taught following engineering classes:

  - Electrical Circuit I, Spring 2006
  - Control Systems, Fall 2005
  - Digital & Analog Communication, Spring 2005

- Research Assistance, Department of Electrical & Computer Engineering, University of North Carolina, Charlotte, August 2008 – May 2009.

- Networks Engineer**,** Jordanian Telecommunications Company, Jordan, Jun. 2004-Jun.2005.

COMPUTER PROFICIENCIES:

System Programming: DSP programming using MathCAD**,** Digital Image programming using C++, Control systems designs using MATLAB.
Platforms: Worked on Linix and Windows XP.
Languages: C, C++, and FORTRAN 90
Scripting Languages: HTML
Packages/Tools: COMSOL, MATLAB, MathCAD, 3D Game Studio, LabVIEW, StressCheck, ModelSim SE, IPerf, and Microsoft Office.

Schematic Capture and PCB layout Software: LTspice/SwitcherCAD III, CircuitMaker, Altium Designer, ExpressPCB**,** ExpressSCH.

PUPLICATIONS:

1. **S. Lasassmeh**, E. Lynch, C. T. Law, and R. El-Hajjar, "Chirped Fiber Optical Current Sensor Based on Graded Terfenol-D Composite," in *Frontiers in Optics 2015*, OSA Technical Digest (online) (Optical Society of America, 2015), paper FTh3E.3.

2. Sweeney, B., **Lasassmeh, S**., Elhajjar, R., and Law, C., "Chirped Fiber Optical Current Sensor using Magnetostrictive Composites," 2015 ASME Power and Energy Conference, June 28 – July 2, San Diego, CA, USA.

3. A. D. Mueller, C. T. Law, and **S. M. Lasassmeh**, "Novel Chirped Fiber Optic Current Sensor," in *Frontiers in Optics 2012/Laser Science XXVIII*, OSA Technical Digest (online) (Optical Society of America, 2012), paper FM3H.4.

PROFESSINAL SERIVCES AND ACTIVITES:

- President of Optical Society of America – University of Wisconsin Student Chapter.
- Poster presentation at Johnson Control International Tech Challenge, May 2017.
- Conducted workshop on MATALB programing for undergraduate students, University of Wisconsin, Milwaukee, February 2013.
- Conducted workshop on Spice for graduate teaching Assistants, University of Wisconsin, Milwaukee, August 2014.
- Served as judge in UWM Undergraduate Research Symposium, 2014.
- Served as judge in UWM Undergraduate Research Symposium, 2015.
- Represented Optical Society of America at Student Leadership Conference in San Jose, California, October, 2015.
- Poster presentation at College of Engineering & Applied Science Poster Competition, 2015.
- Poster presentation at Microscopy & Optical Coherence Tomography Poster Session, San Jose, California, 2015.
- Poster presentation at College of Engineering & Applied Science Poster Competition, 2016.

HONORS AND AWARDS:

- Second place – graduate level Larry Hause Poster Competition of the IEEE Milwaukee Section, May 2015.
- Chancellor's Graduate Student Award, University of Wisconsin, Milwaukee, 2011-2012.
- Graduate Assistant Support Plan (GASP), University of North Carolina, Charlotte, 2008-2010.

MEMBERSHIP IN PROFESSINAL SOCITES:

- Optical Society of America (OSA).
- Institute of Electrical and Electronics Engineers (IEEE).
- Society of Women Engineers (SWE).